Molecular Pharmacology Fast Forward. Published on October 5, 2015 as DOI: 10.1124/mol.115.100917
This article has not been copyedited and formatted. The final version may differ from this version.

Long-range inhibitor-induced conformational regulation of human IRE1α endoribonuclease activity

Nestor O. Concha, Angela Smallwood, William Bonnette, Rachel Totoritis, Guofeng Zhang, Kelly Federowicz, Jingsong Yang, Hongwei Qi, Stephanie Chen, Nino Campobasso, Anthony E. Choudhry, Leanna E. Shuster, Karen A. Evans, Jeff Ralph, Sharon Sweitzer, Dirk A. Heerding, Carolyn A. Buser, Dai-Shi Su, & M. Phillip DeYoung

Oncology R&D (K.F., J.Y., L.E.S., K.A.E., J.R., D.A.H., C.A.B., D.S.S, M.P.D.), Biological Sciences (R.T., G.Z., H.Q., S.C., A.E.C., S.S.), and Chemical Sciences (N.O.C., A.S., W.B., N.C.), GlaxoSmithKline Research and Development, Collegeville, PA

Molecular Pharmacology Fast Forward. Published on October 5, 2015 as DOI: 10.1124/mol.115.100917
This article has not been copyedited and formatted. The final version may differ from this version.

Running Title: Structure of human phosphorylated (active) IRE1α dimer

Corresponding author:

M. Phillip DeYoung (maurice.p.deyoung@gsk.com) or Nestor O. Concha

(Nestor.O.Concha@gsk.com)

GlaxoSmithKline, Oncology R&D

1250 S. Collegeville Road, UP1450

Collegeville, PA 19426, USA

Phone : 610-917-5025

Pages: 40

Tables: 1

Figures: 5

References: 46

Words in abstract: 244

Words in Introduction (including references and PDB IDs): 794

Words in Discussion (including references and PDB IDs): 1649

Non-standard abbreviations:

APY29: 2-N-(3H-benzimidazol-5-yl)-4-N-(5-cyclopropyl-1H-pyrazol-3-yl)pyrimidine-2,4-diamine, ATF6: activating transcription factor 6, BIIC: baculovirus-infected insect cells, ER: endoplasmic reticulum, ERAD: ER-associated protein degradation, FP: fluorescence polarization, GSK2850163: (R)-2-(3,4-dichlorobenzyl)-N-(4-methylbenzyl)-2,7-diazaspiro[4.5]decane-7-carboxamide, HDX: hydrogen-deuterium exchange, IRE1α: inositol-requiring enzyme-1 alpha, KIRA6: 1-(4-(8-Amino-3-tert-butylimidazo[1,5-a]pyrazin-1-yl)naphthalen-1-yl)-3-(3-(trifluoromethyl)phenyl)urea, PERK: PKR-like ER kinase, RIDD:

Molecular Pharmacology Fast Forward. Published on October 5, 2015 as DOI: 10.1124/mol.115.100917
This article has not been copyedited and formatted. The final version may differ from this version.

regulated IRE1α dependent degradation, RNase: endoribonuclease, SAR: structure activity relationship, STS: staurosporine, TEV: tobacco etch virus, UPR: unfolded protein response, UPRE: unfolded protein response element

Molecular Pharmacology Fast Forward. Published on October 5, 2015 as DOI: 10.1124/mol.115.100917
This article has not been copyedited and formatted. The final version may differ from this version.

ABSTRACT

Activation of the inositol-requiring enzyme-1 alpha (IRE1α) protein caused by endoplasmic reticulum (ER) stress results in the homodimerization of the N-terminal ER luminal domains, autophosphorylation of the cytoplasmic kinase domains, and conformational changes to the cytoplasmic endoribonuclease (RNase) domains which render them functional and can lead to the splicing of XBP1 mRNA. Herein we report the first crystal structures of the cytoplasmic portion of a human phosphorylated IRE1α dimer in complex with GSK2850163, a novel, IRE1α-selective kinase inhibitor, and with staurosporine (STS), a broad spectrum kinase inhibitor. GSK2850163 inhibits both the kinase and RNase activities of IRE1α. The inhibitor interacts with the catalytic residues Lys599 and Glu612 and displaces the kinase activation loop to the DFG-out conformation. Inactivation of IRE1α RNase activity appears to be caused by a conformational change whereby the αC helix is displaced resulting in the rearrangement of the kinase domain-dimer interface and a rotation of the RNase domains away from each other. In contrast, STS binds at the ATP-binding site of IRE1α resulting in a dimer consistent with RNase active yeast Ire1 dimers. Activation of IRE1α RNase activity appears to be promoted by a network of hydrogen bond interactions between highly conserved residues across the RNase dimer interface that place key catalytic residues poised for reaction. These data implicate that the intermolecular interactions between conserved residues in the RNase domain are required for activity, and that the disruption of these interactions can be achieved pharmacologically by small molecule kinase domain inhibitors.

Molecular Pharmacology Fast Forward. Published on October 5, 2015 as DOI: 10.1124/mol.115.100917
This article has not been copyedited and formatted. The final version may differ from this version.

INTRODUCTION

Cellular stresses such as accumulation of unfolded proteins, hypoxia, glucose deprivation, depletion of ER calcium levels, and changes in ER redox status activate the unfolded protein response (UPR), an intracellular signal transduction network involved in restoring protein homeostasis (reviewed in Walter and Ron, 2011). To alleviate these types of stress responses, the UPR responds by halting protein translation, activating transcription of UPR-associated target genes, and degrading misfolded proteins (Ron, 2002; Harding, et al, 2002; Feldman et al., 2005). UPR signaling also regulates cell survival by modulating apoptosis and autophagy and can induce cell death under prolonged ER stress if the misfolded protein burden is too high (Woehlbier and Hetz, 2011; Ma and Hendershot, 2004; Rouschop et al., 2010).

Three key ER membrane proteins have been identified as primary effectors of the UPR: PKR-like ER kinase (PERK), inositol-requiring enzyme 1 α/β (IRE1), and activating transcription factor 6 (ATF6) (Schroder and Kaufman, 2005). IRE1α is a transmembrane protein that functions both as an ER stress sensing receptor via its N-terminal ER luminal domain and as a signal transducer via its cytoplasmic C-terminal kinase and RNase domains (Tirasophon et al., 1998). Upon sensing ER stress, the extracellular portion of the IRE1α protein will homodimerize, allowing for trans autophosphorylation, which, in turn, induces a conformational change resulting in activation of the RNase domains (Ali et al., 2011). Phosphorylation within the kinase activation loop is an essential step for RNase activation (Prischi et al., 2014). Mammalian IRE1α excises a 26-bp intron from the mRNA of XBP1 that causes a translational frame shift downstream of the splice site to produce XBP1s, the active form of the transcription factor (Yoshida et al., 2001; Calfon et al., 2002; Lee et al., 2002). XBP1 is responsible for the

Molecular Pharmacology Fast Forward. Published on October 5, 2015 as DOI: 10.1124/mol.115.100917
This article has not been copyedited and formatted. The final version may differ from this version.

activation of key UPR target genes, including molecular chaperones and components of the ER-associated protein degradation (ERAD) machinery (Lee at al., 2003). Activation of IRE1α is also reported to result in the induction of regulated IRE1α dependent degradation (RIDD) of a subset of mRNAs encoding secretory proteins or the induction of apoptosis via IRE1α signaling through its kinase domain and downstream effectors ASK1, JNK1, and Caspase-12 (Hollien and Weissman, 2006; Urano et al., 2000).

Loss of ER homeostasis (i.e., loss or hyperactivation of UPR signaling) has been attributed to a number of diseases, including cancer, diabetes, cardiovascular diseases, liver diseases, and neurodegenerative disorders, and the UPR is increasingly becoming an attractive pathway in drug discovery (Hetz et al., 2013; Maly and Papa, 2014). To this end, an increasing body of work has been performed to identify potent and selective molecules of IRE1α and to better understand how these molecules bind and affect IRE1α activation mechanisms. Crystal structures of the C-terminal region of phosphorylated (active) yeast Ire1 were the first to be characterized and revealed that Ire1 forms dimers arranged in a “back-to-back” configuration with the kinase active sites facing outward (PDB ID 2RIO; Lee at al., 2008; PDB ID 3FBV; Korennykh et al., 2009; PDB ID 3LJ0; Wiseman et al., 2010). This dimer arrangement also formed the basis of a rod-shaped helical structure representing a high-order oligomeric Ire1 structure in complex with the kinase inhibitor APY29 (3FBV; Korennykh et al., 2009). These yeast “back-to-back” structures contrast with the first reported human IRE1α dimer: a dephosphorylated C-terminal IRE1α- Mg^{2+}-ADP complex possibly representing an early state prior to phosphoryl-transfer (PDB ID 3P23; Ali et al., 2011). In this structure, the kinase active sites are facing each other and are in a suitable orientation and proximity for trans autophosphorylation, but the RNase domains are far from each other and inactive. A similar

Molecular Pharmacology Fast Forward. Published on October 5, 2015 as DOI: 10.1124/mol.115.100917
This article has not been copyedited and formatted. The final version may differ from this version.

"face-to-face" structure was recently reported for mouse IRE1α, but this structure was phosphorylated (PDB ID 4PL3; Sanches et al., 2014). More recently, a few other dephosphorylated human crystal structures were reported. One is of a co-crystal structure containing a kinase domain inhibitor bound to an IRE1α monomer (PDB ID 4U6R; Harrington et al., 2014). Here, no dimers were found with the inhibitor-bound structure suggesting that the compound may either prevent dimerization or stabilize a monomeric IRE1α. The second report presented two "back-to-back" dimers of IRE1α, one in apo form and one in an inhibitor-bound form (PDB IDs 4Z7G and 4Z7H; Joshi et al., 2015). These structures are consistent with yeast Ire1 dimers but are distinct in that the apo structure contains a twisted interface between the dimers across the RNase domains which may represent an additional intermediate of IRE1α prior to full activation. The culmination of all these structures may depict the IRE1 protein at various levels of activation and suggest that this process is conserved evolutionarily. Here we present a proposed structure of the final state of a human phosphorylated (active) IRE1α dimer co-crystallized with two kinase inhibitors that have opposing effects to the RNase activity of the protein.

Molecular Pharmacology Fast Forward. Published on October 5, 2015 as DOI: 10.1124/mol.115.100917
This article has not been copyedited and formatted. The final version may differ from this version.

MATERIALS AND METHODS

IRE1α protein expression and purification

The cytosolic domain of human IRE1α (NM_001433) encompassing amino acids 547-977 was cloned into pENTR/TEV/D-TOPO (Life Technologies, Carlsbad, CA) and subsequently transferred to a pDest8 (Life Technologies) vector backbone containing N-terminal Flag epitope tag followed by 6xHis tag and tobacco etch virus (TEV) cleavage site (ENLYFQG/S). Baculovirus generation was accomplished using the Bac-to-Bac® baculovirus generation system (Life Technologies). Flag-His_6-TEV-IRE1α (547-977) protein expression in baculovirus-infected insect cells (BIIC) was accomplished following established procedures (Wasilko and Lee, 2006). Briefly, a proprietary Sf9 insect cell line was grown to early log phase, infected with $1x10^7$ BIIC/10 L culture and incubated at 27°C. Cell paste was harvested at 66-72 h post infection. Human phosphorylated or dephosphorylated IRE1α protein containing N-terminal Flag-His_6 tags and a TEV protease cleavage site between the tags and IRE1α protein was purified from ~150 g of cells from a 10L culture (lysed in 1.5 L lysis buffer (50 mM Hepes, pH 7.5, 10% glycerol, 300 mM NaCl) by EmulsiFlex-C50 homogenizer (Avestin, Ottowa, ON). The protein in the clear supernatant from centrifugation at 30,000g for 30 min at 4°C was first captured in 20 ml NiNTA-SF beads (Qiagen, Venlo, Netherlands) in batch mode for 4 h at 4°C. The beads were poured into a column, washed with 20 mM imidazole in lysis buffer, and the IRE1α protein was eluted from the column by 300 mM imidazole in 50 mM Hepes, pH 7.5, 150 mM NaCl buffer. The Ni elution pool was concentrated using a 10 kDa MW cutoff filter concentrator to about 25 ml to which 3 mg of Tev protease was added to remove the His_6 tag. This mixture was then transferred into dialysis tubing (8 kDa MW cutoff) and dialyzed overnight against 3L MonoQ buffer A (50 mM Hepes, pH 7.5, 50 mM NaCl, 5 mM DTT, 1 mM EDTA),

Molecular Pharmacology Fast Forward. Published on October 5, 2015 as DOI: 10.1124/mol.115.100917
This article has not been copyedited and formatted. The final version may differ from this version.

passed through a second 20 ml Mono Q column (GE Healthcare, Piscataway, NJ), and eluted with a 50-500 mM NaCl gradient over 10 column volumes. The eluted samples were analyzed by LC-MS, and the major peak with a mass consistent with the expected molecular weight for the protein plus three phosphates (80 mass units per phosphate) was purified in a Hiload Superdex 200 sizing column (GE Healthcare) with a buffer of 50 mM Hepes, pH 7.5, 200 mM NaCl, 5 mM DTT, 1 mM EDTA. The eluted protein (2-3 mg protein in 1 ml aliquots) was stored at -80°C and later used in assays and crystallography. The remaining fractions from the Mono Q column were pooled and treated with λ-phosphatase to produce the fully dephosphorylated enzyme before it was further purified and stored in the same way as the triply phosphorylated protein.

pIRE1α RNase activity assay

The nuclease enzymatic activity of phosphorylated IRE1α (pIRE1α) was measured using a dual labeled 36-mer RNA substrate that contained the IRE1α recognition sequence with a 6-carboxyfluorescein fluorescent reporter (6-FAM) at the 3' end, and the Black Hole quencher -1 (BHQ-1) at the 5' end (5'/6-FAM/rCrArG rUrCrC rGrCrA rGrCrA rCrUrG/BHQ-1/3'; Integrated DNA Technologies, Coralville, IA). Upon cleavage, the release of FAM results in an increase in fluorescent signal measured at $\lambda_{ex}/\lambda_{em}$ = 485/535nm. A typical enzymatic reaction was carried out with 10 nM pIRE1α and 500 nM substrate in a buffer containing 20 mM HEPES, pH 7.5, 5 mM $MgCl_2$, 10 mM NaCl, 1 mM DTT, 0.05% Tween-20 and 0.02% heat-treated casein (heated for 20 min at 60^{o}C prior to use each time), and the fluorescence change was followed using an Envision plate reader (PerkinElmer, Waltham, MA).

Molecular Pharmacology Fast Forward. Published on October 5, 2015 as DOI: 10.1124/mol.115.100917
This article has not been copyedited and formatted. The final version may differ from this version.

To identify inhibitors of IRE1α nuclease activity, pIRE1α was screened against the GSK compound collection. The RNA oligomer substrate was added to the assay plates containing 10 μM compound. The reaction was initiated immediately by the addition of enzyme and the plates centrifuged for 1 minute at 500 rpm. The final reaction mixture contained 10 nM pIRE1α, 25 nM RNA oligomer, 20 mM HEPES pH 7.5, 5 mM $MgCl_2$, 1 mM DTT, 0.05% Tween-20, 10 mM NaCl, and 0.02% casein. The reaction plates were incubated at room temperature for 90 minutes before the reaction was terminated with 0.015% SDS in 20 mM HEPES, pH 7.5. The plates were centrifuged for 3 min at 1000 rpm prior to measuring product formation using the Viewlux imager (PerkinElmer).

pIRE1α kinase assays

In the ADP-Glo™ assay, a compound's potency towards pIRE1α kinase activity was measured as its inhibition of an intrinsic, slow ATP hydrolysis activity. 100 nL DMSO solution of GSK2850163, at various concentrations, was added into a white Greiner low volume 384 well plate. The reaction was carried out with 5 nM pIRE1α and 60 μM ATP in 10 μL 50 mM HEPES buffer, pH 7.5, containing 30 mM NaCl, 10 mM $MgCl_2$, 1 mM DTT, 0.02% Chaps and 0.01 mg/mL BSA. The reaction was stopped after 2 h by adding 5 μL ADP-Glo™ reagent I, which also depletes the remaining ATP. Following a 1 h incubation, 5 μL ADP-Glo™ reagent II was added into the reaction, which converts the ADP product into ATP to serve as substrate for the coupled luciferin/luciferase reaction. After 30 min, the plate was read on a Wallac ViewLux microplate imager.

In the fluorescence polarization (FP) assay, a compound's affinity was measured by its ability to compete with a fluorescent labeled ATP site ligand for binding to the kinase domain.

Molecular Pharmacology Fast Forward. Published on October 5, 2015 as DOI: 10.1124/mol.115.100917
This article has not been copyedited and formatted. The final version may differ from this version.

The FP assay was carried out in the same reaction buffer described above. A 10 μL reaction contained 5 nM IRE1, 5 nM fluorescent ligand (GSK369716A), and GSK2851063 at various concentrations. After the addition of reagents, the plate was incubated at room temperature for 15 min and then read on an Analyst GT multimode reader (Molecular Devices, Sunnyvale CA) at excitation/emission of 485nm/530nm with a dichroic of 505 nm. IC_{50} values were calculated using the data fitting software GraFit (Erithacus Software).

PERK kinase assay

Recombinant PERK protein (Life Technologies) was purchased for use in a selectivity assay to test pIRE1α inhibitors. Solution of PERK (0.40 nM) in assay buffer containing 10 mM HEPES, pH 7.5, 2 mM CHAPS, 5 mM $MgCl_2$, and 1 mM DTT was pre-incubated with compound for 30 min at room temperature. The reaction was initiated by the addition of substrate mix which contained 0.040 μM biotinylated eIF2α (eukaryotic translation initiation factor 2α) peptide and 5 μM ATP. The reaction plates were incubated at room temperature for 60 min, followed by termination with a detection/quench mixture. The detection/quench mixture contained 15 mM EDTA, 4 nM eIF2α phospho antibody (Millipore, Billerica, MA), 4 nM europium-labeled anti-rabbit antibody (PerkinElmer) and 40 nM streptavidin APC (PerkinElmer). The plates were incubated for 10 min at room temperature prior to measuring HTRF signal (excitation at 610-640nm, emission at 660nm) using the Viewlux imager.

RNase L activity assay

A solution of 0.1 nM RNase L, 1 μM ATP, and 8 nM 2-5A (2′,5′-linked oligoadenylate, $p_{1–3}(A2'p5'A)_{n\geq2}$) in assay buffer containing 20 mM HEPES, pH 7.5, 10 mM $MgCl_2$, 1 mM TCEP, 0.5 mM CHAPS, 100 mM NaCl, and 0.02% casein was incubated at room temperature

Molecular Pharmacology Fast Forward. Published on October 5, 2015 as DOI: 10.1124/mol.115.100917
This article has not been copyedited and formatted. The final version may differ from this version.

for 30 minutes. A 0.2 μM solution of a 36-mer RNA substrate (5'/6-FAM rUrUrA rUrCrA rArArU rUrCrU rUrArU rUrUrG rCrCrC rCrArU rUrUrU rUrUrU rGrGrU rUrUrA BHQ-1/3'; Integrated DNA Technologies) was prepared in assay buffer and added to reaction plates containing compounds. The reaction was initiated with the addition of RNase L-ATP-2-5A mixture and the plates incubated at room temperature for 90 min. Following the incubation, the reaction was terminated with 0.02% SDS solution in nuclease free water. The plates were centrifuged for 3 min at 1000 rpm prior to measuring product formation using the Viewlux imager.

Competitive inhibition studies

In single compound inhibition studies, the concentrations of the substrate or non-cleavable substrate (analog in which the ribose linked to the guanine at the cleavage site was replaced by deoxyribose), and GSK2850163 were varied and the enzyme concentration was fixed at 10 nM. The modes of inhibition and the inhibition constants were determined by fitting the initial velocities to different models (competitive, uncompetitive and noncompetitive) using Grafit software. In a double inhibition experiment, the concentration of the first inhibitor was varied at several different concentrations of the second inhibitor, and the concentrations of the enzyme and substrate were kept constant at 10 nM and 100 nM, respectively. The reactions were monitored kinetically and the initial reaction velocities were analyzed using the Yonetani-Theorell equation.

Protein crystallization and structure determination

Crystals of pIRE1α (547-977) with GSK2850163 (PDB: 4YZ9) were prepared by mixing pIRE1α with 0.5 mM GSK2850163 and incubating overnight on ice. The crystals were grown at

Molecular Pharmacology Fast Forward. Published on October 5, 2015 as DOI: 10.1124/mol.115.100917
This article has not been copyedited and formatted. The final version may differ from this version.

20°C by vapor diffusion in sitting drops containing 2 µl of protein (13 mg/ml in 50 mM Hepes, pH 7.5, 200 mM NaCl, 5 mM DTT, 1 mM EDTA , 0.5 mM GSK2850163, 0.25% DMSO) and 2 µl reservoir solution containing PEG 3350 (16%-22%), 100 mM Hepes pH 7.0, 200 mM Ca^{2+} acetate. The crystals were thick rods that appeared over 2-5 days and reached full size (0.05 X 0.025 X 0.3 mm) in 2 weeks. Seeding was used to improve crystal quality. The pIRE1α + GSK2850163 crystals were frozen in a solution of 20% ethylene glycol, 22% PEG 3350, 0.2 M calcium acetate added in a stepwise manner to the protein drop before mounting the crystal on the loop.

The crystals of pIRE1α with Mg^{2+}-ADP (PDB: 4YZD) were grown by mixing 2 µl protein solution (10 mg/ml pIRE1α (547-977) in 50 mM Hepes, pH 7.5, 200 mM NaCl, 5 mM DTT, 1 mM EDTA, 1 mM ADP (100 mM ADP stock was ~ pH 7.0), 1 mM $MgCl_2$) with 2 µl reservoir solution (16 % PEG 3350, 200 mM Na^+ Malonate pH 6.0) in sitting drops at room temperature. Seeding was used to initiate crystal growth. Crystals appeared the next day and grew to full size in 3 weeks. For data collection, the crystals were frozen in a solution of 20% ethylene glycol, 22% PEG 3350, 200 mM Na^+ Malonate pH 6.0 and added to the protein drop before mounting the crystals on the loop.

The complex of pIRE1α (547-977) with staurosporine (PDB: 4YZC) was prepared by mixing the protein with 0.5 mM staurosporine and incubated overnight on ice. The crystals were grown at 20°C by vapor diffusion in sitting drop containing 2 µl of protein (13 mg/ml in 50 mM Hepes, pH 7.5, 200 mM NaCl, 5 mM DTT, 1 mM EDTA) and 2µl reservoir solution containing PEG 300 (30%-40%), 100 mM Hepes pH 7.5, 200 mM KCl. Small hexagonal plates appeared over 5-10 days and reached full size (0.05 X 0.75 X 0.15 mm) in ~20 days. The crystals were

Molecular Pharmacology Fast Forward. Published on October 5, 2015 as DOI: 10.1124/mol.115.100917
This article has not been copyedited and formatted. The final version may differ from this version.

flash-frozen in liquid N_2 directly from the crystallization drop. All diffraction data was collected at the Advanced Photon Source, Argonne National Laboratories, Life Sciences CAT, Sector 21.

All structures were determined by molecular replacement with Phaser (Afonine et al., 2010) as implemented in CCP4 (Winn et al., 2011) using the human dephosphorylated IRE1α-Mg^{2+}-ADP complex (3P23; Ali et al., 2011) as a model. Refinement was performed by a combination of Refmac5 (Murshudov et al., 1997) and Phenix (Afonine et al., 2010) with manual adjustments to the model in COOT (Emsley and Cowtan, 2004). The quality of the model was monitored using Molprobity (Chen et al., 2010). Figures were made with PYMOL (Schrödinger, LLC, New York, NY).

Detection of XBP1 splicing by RT-PCR

Multiple myeloma cancer cell lines were obtained from ATCC (Manassas, VA) or DSMZ (Braunschweig, Germany). Cells were cultured in the appropriate culture medium supplemented with 10% FBS (Sigma-Aldrich, St. Louis, MO) at 37°C in humidified incubators under 5% CO_2. Cells were seeded into 6-well plates at a density of $1.5x10^6$ cells/well in the appropriate media containing 1% FBS media and were treated with 5 μg/mL tunicamycin (MP Biomedicals, Newport Beach, CA) for 1 h before the addition of GSK2850163 for 3 h (four hours total). For studies involving staurosporine (Sigma-Aldrich) treatment, cells were treated with staurosporine for 30 min followed by 5 μg/mL tunicamycin for 1 h. RNA was collected using the Qiagen RNEasy Mini Kit. RNA was quanitated using a NanoDrop (Thermo Scientific, Philadelphia, PA) and stored at -80°C. To generate cDNA, the High-Capacity cDNA Reverse Transcription Kit (Life Technologies) was used. For PCR, a 25 μL reaction included 12.5 μL of Master Mix (Promega Go-Taq 2X Master Mix), 1 μL each of forward and reverse primers (100 ng/μL), 9.5

Molecular Pharmacology Fast Forward. Published on October 5, 2015 as DOI: 10.1124/mol.115.100917
This article has not been copyedited and formatted. The final version may differ from this version.

μL of water, and 1 μL of cDNA template. Primers for human XBP1 were: Forward: 5'-CCTGGTTGCTGAAGAGGAGG-3' and Reverse: 5'-CCATGGGGAGATGTTCTGGG-3'. RT-PCR conditions were: 95°C for 5 min; 95°C for 30 sec; 58°C for 30 sec; 72°C for 30 sec; 72°C for 5 min with 35 cycles of amplification. After RT-PCR, reactions were run on a 3% agarose gel and visualized using SYBR® Safe DNA gel stain (Life Technologies) and a BioRad Imager (Hercules, CA).

Western blot analysis

RPMI 8226 cells were seeded into 6-well plates at a density of $2.0x10^6$ cells/well in RPMI 1640 media containing 1% FBS. Cells were treated with the same conditions as described above for XBP1 splicing detection by RT-PCR. To harvest protein lysates, cells were lysed with 60 μL of 1X cell lysis buffer (Cell Signaling Technologies, Danvers, MA) containing protease and phosphatase inhibitors. Cell lysates were quantified using the Pierce BCA Protein Assay Kit (Thermo Scientific) and samples were read on a SPECTRAmax 190 instrument. Following quantitation, 40 μg of protein was run on 4-12% Bis-Tris gels (LifeTechnologies), and protein was transferred onto 0.45 μM nitrocellulose membranes (LifeTechnologies) using the BioRad semi-dry transfer blotting apparatus. Membranes were blocked for one hour using Li-Cor Odyssey Blocking Buffer then probed with the following antibodies overnight: pIRE1α S724 (Abcam, #ab48187; 1:1000), total IRE1α (Abcam, #ab37073; 1:1000), and GAPDH (Bethyl Laboratories, #A300-639A; 1:2000). After washing, blots were incubated with donkey anti-rabbit IRDye-800CW secondary antibody (Li-Cor), and proteins were visualized using the Odyssey Imaging System.

Molecular Pharmacology Fast Forward. Published on October 5, 2015 as DOI: 10.1124/mol.115.100917
This article has not been copyedited and formatted. The final version may differ from this version.

XBP1 transcriptional activity assay

PANC-1 cells were seeded into 6-well plates at a density of $5.0x10^3$ cells/well in RPMI 1640 media containing 10% FBS. Cells were co-transfected with a pGL3-5xUPRE-luciferase reporter containing five repetitions of the XBP-1 DNA binding site (a kind gift from R. Prywes, Columbia University) and pRL-SV40 (Promega, Madison, WI) using FuGENE6 transfection reagent (Roche, Indianapolis, IN). Forty eight hours later, cells were treated with 2.5 µg/mL tunicamycin for 1 hour followed by GSK2850163 treatment for 16 hours. Luciferase expression was measured using Dual-Glo Luciferase Assay kit (Promega) and normalized to renilla expression levels.

Hydrogen-Deuterium Exchange

pIRE1α (547-977, 78 µM) was incubated with 250 µM GSK2850163 or 1 mM staurosporine for at least 18 hours. 2 µl of protein-inhibitor mixture was mixed with 18 µl D_2O at room temperature for 1 minute, after which 20 µl of 4M guanidinium chloride in 1M glycine buffer, pH 2.5 and 120 µl formic acid were added and immediately transferred to an ice cold bath. All subsequent treatment and analysis was done at 2-4˚C. 50 µl of this solution was injected into a Waters Enzymate BEH pepsin 2.1 x 30 mm column for digestion, then to a C18 column and into a LTQ XL Orbitrap mass spectrometer. The z/m values were calculated with XCalibur and compared with sequences in the MASCOT database. The analysis of the H/D exchange was done with HDExaminer. Tryptic digestion of all the samples gave a sequence coverage of at least 98% of the amino acid sequence.

Preparation and characterization of compounds 1-24

Molecular Pharmacology Fast Forward. Published on October 5, 2015 as DOI: 10.1124/mol.115.100917
This article has not been copyedited and formatted. The final version may differ from this version.

Details provided in supplementary methods.

RESULTS

Crystallization of the novel inhibitor GSK2850163 bound to pIRE1α

Because of the relevance of the IRE1α/XBP1 pathway in human disease, we sought to identify small molecules that would inhibit IRE1α RNase activity. GSK2850163 was discovered as a result of a high-throughput screening campaign to identify IRE1α-selective inhibitors of XBP1 splicing. It is a highly selective inhibitor with dual activity: it inhibits IRE1α kinase activity (IC_{50} = 20 nM) and RNase activity (IC_{50} = 200 nM) (Fig. 1A, Supplementary Table 1). In competition kinetic studies, GSK2850163 and a noncleavable RNA substrate demonstrated mutually exclusive binding to activated IRE1α (K_i = 200 ± 20 nM) (Supplementary Fig. 1). We hypothesized that this was due to bound GSK2850163 altering the preferred enzyme structure for RNA substrate binding (and vice versa) and not due to a physical overlapping of binding sites.

To investigate the mode of binding and to enable structure-guided optimization of GSK2850163, we determined the co-crystal structure of GSK2850163 with the C-terminal portion of the phosphorylated human IRE1α protein (pIRE1α, residues 547-977, PDB ID: 4YZ9) (Fig. 1B, Supplementary Fig. 2, Table 1). The structure of pIRE1α-GSK2850163 is of a "back-to-back" dimer with one inhibitor molecule bound to the kinase domain of each protomer in a pocket next to the kinase αC helix, approximately 12 Å from hinge region (Fig. 1C). GSK2850163 adopts a "U" shaped conformation with the tolyl and dichlorophenyl groups facing the inside of the protein and the spirodecane core partially solvent exposed with the piperidine ring (A-ring) in a chair conformation. Two key interactions with conserved kinase catalytic residues, Glu612 and Lys599, are observed. The urea nitrogen and the pyrrolidine nitrogen of

Molecular Pharmacology Fast Forward. Published on October 5, 2015 as DOI: 10.1124/mol.115.100917
This article has not been copyedited and formatted. The final version may differ from this version.

GSK2850163 form a hydrogen bond interaction with the side chain of Glu612, and the carbonyl oxygen of the urea of GSK2850163 interacts through a hydrogen bond with the side chain of Lys599.

GSK2850163 displaces the kinase activation loop of pIRE1α such that the DFG motif is in the "out" conformation and is flipped by nearly 180° occupying the ATP binding site (Fig. 1C). This clearly contrasts with our resolved structure of pIRE1α-ADP-Mg^{2+} (PDB ID: 4YZD) where the DFG motif is found in the "in" conformation and Phe712 occupies the same pocket where the GSK2850163 binds in the pIRE1α-GSK2850163 structure (Fig. 1D and Table 1). Phe712 makes a π interaction with Tyr628 in a pocket lined by Val613, Leu616, Vals625, and Leu679. Superposition of the ADP-Mg^{2+} and GSK2850163-bound pIRE1α complexes shows that GSK2850163 does not overlap with the ATP-binding site (data not shown). The structure of pIRE1α in complex with Mg^{2+}-ADP forms a "face-to-face" dimer across the symmetry planes with neighboring molecules (Supplementary Fig.3). Consistent with previously published structures, the kinase active sites are facing each other and are in an orientation and proximity favorable for trans autophosphorylation (3P23; Ali et al., 2011; 4PL3; Sanches et al., 2014). The present structure may possibly represent an early post-phosphoryl-transfer dimer, while the "face-to-face" structure of dephosphorylated human IRE1α may represent a state just prior to phosphoryl-transfer.

Structure activity relationship of GSK2850163

To provide supportive evidence for the binding mode of GSK2850163 observed in the crystal structure, we performed structure activity relationship (SAR) studies whereby we systematically modified the structure of the ligand and followed the effect by measuring pIRE1α

Molecular Pharmacology Fast Forward. Published on October 5, 2015 as DOI: 10.1124/mol.115.100917
This article has not been copyedited and formatted. The final version may differ from this version.

RNase inhibition. First, we observed that while the *S*-enantiomer is inactive and its conformation does not fit in the electron density map, the *R*-enantiomer inhibited the RNase activity *in vitro* with an IC_{50} = 0.2 μM (Fig. 2A). The *R*-enantiomer is refined in the structure of the complex. Since the activity of the *R*-enantiomer is equally potent to the racemic compound and *S*-enantiomer is not active, the initial SAR study was performed with the racemic analogs.

Secondly, the NH of urea nitrogen and the pyrrolidine nitrogen are required to make a H-bond with Glu612 (2.98Å), and any changes in the GSK2850163 (compound **1**) molecule disrupting these specific H-bond interactions resulted in loss of activity. For example, replacement of the urea nitrogen (compound **2**) or capping the NH with a methyl group (compound **3**) caused a loss of potency (Fig. 2A). Similarly, conversion of a basic amine in pyrrolidine ring to a non basic amide yielded an inactive analog (compound **4**, Fig. 2A).

Thirdly, in the binding mode of GSK2850163 in complex with pIRE1α described here, the lipophilic groups at both ends of molecule (the tolyl and dichlorophenyl groups) are accommodated within the lipophilic pockets observed in the core crystal structure (Supplementary Fig. 2B) and are critical for the inhibitor's activity. All analogs with polar functionality, such as pyridines, were not active (compounds **5-6,** Fig. 2B) or much less active (compounds **15-19,** Fig. 2C). On the other hand, the lipophilic groups were well tolerated (compounds **8-14, 20-24**) in the hydrophobic pocket. Deletion of one of the chlorines to form 3- or 4-mono chloro analogs (**7** and **8**, respectively) revealed that the 4-chloro substitution was more tolerated than 3-position in term of potency (Fig. 2B). Replacement of 3-chloro with other groups, such as fluoro (**11**), methyl (**12**), or methoxy (**13**), provided equally potent analogs, but the trifluoromethyl group (**14**) caused a significant loss of potency. The tolyl group at the A-ring urea preferred lipophilic substitutions, and polar functionalities (*e.g.* pyridines (**15**-**17**) and

Molecular Pharmacology Fast Forward. Published on October 5, 2015 as DOI: 10.1124/mol.115.100917
This article has not been copyedited and formatted. The final version may differ from this version.

substituted pyridines (**18**-**19**)) were not tolerated. Deletion of the methyl group gave the simple phenyl analog **20** that maintained RNase activity (IC_{50} = 0.40 μM) (Fig. 2B). Replacement of the methyl group at the 4-position with other lipophilic groups, such as, chlorine (**21**), methoxy (**22**), fluorine (**23**) was well tolerated. The benzodioxole analog **24** exhibited an IC_{50} value of 100 nM. These SAR study results are consistent with the binding mode of GSK2850163 to pIRE1α observed in the crystal structure, and indicate that GSK2850163 functions as a kinase and RNase inhibitor of pIRE1α.

Cellular activity of GSK2850163

We utilized a panel of eight multiple myeloma cell lines to test the effects of GSK2850163 on IRE1α RNase activity. Increased IRE1α activity has been observed in primary multiple myeloma specimens, and clinical studies have associated high levels of spliced XBP1 mRNA with poor patient survival (Reimold et al., 2001; Nakamura et al., 2006; Bagratuni, et al., 2010). To recapitulate an ER stress-induced environment in cell culture, tunicamycin, an inhibitor of N-linked glycosylation, was used (Yoshida et al., 2001). XBP1 mRNA is found primarily in the unspliced form under basal conditions. Upon ER stress stimulation, all cells induced varying degrees of XBP1 splicing that could be reversed following treatment with GSK2850163 (Fig. 3A). ER stress also induced increased autophosphorylation of IRE1α, which could be reduced in a dose-dependent manner by GSK2850163 (Fig. 3B). To determine if GSK2850163 could affect the transcriptional function of XBP1, cells expressing a reporter plasmid under the control of five tandem repeats of the Unfolded Protein Response Element (UPRE) motif were treated with tunicamycin followed by increasing doses of GSK2850163 (Wang et al., 2000). The UPRE sequence contains the binding site found at the promoter of

Molecular Pharmacology Fast Forward. Published on October 5, 2015 as DOI: 10.1124/mol.115.100917
This article has not been copyedited and formatted. The final version may differ from this version.

XBP1 target genes. Induction of ER stress by tunicamycin significantly increases XBP1 transcriptional activity in these cells, yet increasing concentrations of GSK2850163 are capable of reducing this activity (Fig. 3C). These data support our biochemical and structural evidence that GSK2850163 is an inhibitor of IRE1α, capable of inhibiting both kinase and RNase activities of IRE1α.

Crystallization of staurosporine bound to pIRE1α

To further understand the mechanism by which the RNase activity of IRE1α could be modulated pharmacologically with kinase inhibitors, we sought to investigate the effect of the broad-spectrum kinase inhibitor staurosporine (STS) on IRE1α. It has been previously shown that STS inhibits IRE1α kinase activity (Ali et al., 2011) and is likely to bind to the ATP-binding site of IRE1α since it competed with the irreversible IRE1α inhibitor, 4μ8C, preventing the formation of a Schiff base with the kinase active site residue Lys599 (Cross et al., 2012). We found that STS inhibited pIRE1α kinase enzymatic activity (IC_{50}= 3 nM) but had no effect on pIRE1a RNase activity *in vitro* (Fig. 4A). STS exhibited similar binding affinity towards phosphorylated IRE1α (IC_{50}= 30 nM) and dephosphorylated IRE1α (IC_{50}= 50 nM) in a competitive binding assay (data not shown). Interestingly, incubation of STS with dephosphorylated (inactive) IRE1α was capable of activating IRE1α RNase activity (Fig. 4B). To test the effects of STS on IRE1α RNase activity in a cellular context, RPMI 8226 multiple myeloma cells were treated with STS followed by tunicamycin to measure XBP1 splicing. STS treatment alone was sufficient to induce XBP1 splicing, similar to levels achieved with tunicamycin (Fig. 4C). Despite inducing XBP1 splicing, STS did not increase IRE1α autophosphorylation. Instead, STS inhibited tunicamycin-induced autophosphorylation (Fig.

Molecular Pharmacology Fast Forward. Published on October 5, 2015 as DOI: 10.1124/mol.115.100917
This article has not been copyedited and formatted. The final version may differ from this version.

4D). STS treatment may also inhibit IRE1α autophosphorylation below basal levels, but it was difficult to measure this convincingly by Western blot analysis. These observations, both biochemical and in cells, suggest that the effects of STS on IRE1α phosphorylation and XBP1 splicing could be due to direct binding of STS to IRE1α and not just due to general stress that could occur due to the broad-spectrum nature of the compound.

To understand the structural basis of the activation of the RNase activity of IRE1α by staurosporine, we determined the crystal structure of the human pIRE1α-STS complex (PDB ID: 4YZC, Table 1). The pIRE1α-STS complex forms a back-to-back dimer with one STS molecule bound per protomer (Fig. 4E, Supplementary Fig. 4A). STS binds in the ATP-binding site of the kinase domain and interacts with hinge residues Glu643, Cys645, and His692 (Supplementary Fig. 4B). The activation loop containing phosphorylated Ser residues (pSer724, pSer726, and pSer729) that was previously disordered in both the pIRE1α-GSK2850163 and the pIRE1α-ADP complexes is well defined in the pIRE1α-STS complex (Supplementary Fig. 4C). pSer724 interacts with Asn750 via two H-bonds, pSer726 is involved in a H-bond interaction with Arg722 (3.1Å) and Arg728 (3.3 Å), and pS729 is interacting through a H-bond with Lys716 (2.7 Å) and Arg687 (2.5 Å). A network of H-bonds extends from the serines in the activation loop to the αC helix and into the active site DFG motif. Binding of STS to pIRE1α locks the kinase domain in a conformation in which the (*i*) activation loop is in the DFG (711-713)-in conformation; (*ii*) the DFG-aspartate interacts with His689 in the HRD motif in the catalytic loop; (*iii*) the conserved Leu616 in the αC helix interacts with the DFG-phenylalanine in the regulatory spine of the kinase; and (*iv*) Arg687 of the HRD motif interacts with pSer729 (Supplementary Fig. 4C). These are the signatures of a kinase in the active conformation

Molecular Pharmacology Fast Forward. Published on October 5, 2015 as DOI: 10.1124/mol.115.100917
This article has not been copyedited and formatted. The final version may differ from this version.

(Kornev and Taylor, 2010). Attempts to crystallize dephosphorylated IRE1α with STS were not successful.

Comparison of pIRE1α dimer interactions and protein dynamics

To test the pIRE1α dimer interactions observed in the structures, we determined the hydrogen-deuterium exchange of pIRE1α in the presence or absence of either GSK2850163 or STS in solution (Supplementary Fig. 5). Changes in the labeling pattern can be related to changes in protein structure or dynamics resulting from a ligand binding event (Percy et al., 2012; Englander et al., 2003). By mapping the observed labeling onto the two co-crystal structures, we observed three areas where most of the structural changes occurred. The first region is in the vicinity of the ligand binding site (Supplementary Fig. 6A). Increased solvent exposure of the activation loop and the disruption of the conserved salt bridge Arg627 - Asp620 by GSK2850163 are both consistent with the displacement of the activation loop to the DFG-out conformation, and the changes in the αC helix to the inactive conformation (Supplementary Fig. 6B). Secondly, in the presence of STS the residues at the kinase-RNase intramolecular domain interface show increased solvent exposure (Supplementary Fig. 6C). The loosening of the intramolecular interactions is consistent with the reorientation of the pIRE1α dimer that leads to the dimerization of the RNase domains. Simultaneously, the decrease in overall labeling of the RNase domains occurs in concert with the conditions under which RNase domains dimerize (Fig. 5A and 5D). Third, in the presence of bound STS there is an increase in solvent exposure of the residues 900-916 (Supplementary Fig. 6D). These residues form a helix-loop element that interact directly with the RNA substrate and include the catalytically essential His910 (Korennykh et al., 2009; Dong et al., 2001). This apparent increased dynamic state of the helix-

Molecular Pharmacology Fast Forward. Published on October 5, 2015 as DOI: 10.1124/mol.115.100917
This article has not been copyedited and formatted. The final version may differ from this version.

loop catalytic element may be related to the catalytic readiness favored by STS but opposed by GSK2850163.

Comparison of pIRE1α co-crystal structures

A comparison between the pIRE1α-GSK2850163 and pIRE1α-STS complexes shows that both structures are back-to-back dimers (Fig. 5A). Binding of GSK2850163 causes the kinase αC helix (residues 610-619) to move to the inactive conformation by an average 4.4Å ±1.0Å (range of 3.03Å to 6.40Å on superposition of the αC helix carbon atoms) as compared with the position observed in the STS complex (Fig 5B). While the centers of mass of the kinase N-domains (21.5Å to 21.9Å) and C-domains (43.1Å to 43.6Å) remain constant, a nearly 20˚ rotation of the domains relative to one another is observed in the two structures. A differential gap of nearly 4Å between the RNase domains in the structures of pIRE1α-GSK2850163 (29.7Å) and pIRE1α-STS (26.1Å) is reflected in a different set of interactions across the RNase dimer interfaces. Hence, the RNase dimer interface in the pIRE1α-GSK2850163 complex is reduced by 58% (269 $Å^2$) compared to the pIRE1α-STS complex (642$Å^2$) (Fig. 5E). In pIRE1α-GSK2850163, the RNase domains are noticeably separated such that the network of interactions across the dimer is no longer possible. The interactions between the protomers of the pIRE1α-GSK2850163 dimer occur mostly between the kinase domains (1,734 $Å^2$), with less contact occurring between the RNase domains (269$Å^2$). This separation of RNase domains is consistent with the biochemical and cellular data showing that GSK2850163 is a potent inhibitor of pIRE1α RNase activity.

In the pIRE1α-STS complex, the RNase domains form a dimer with two sets of interdigitating H-bond interactions between His909, Asp847 and Arg905 (3.2-3.5Å), and

Molecular Pharmacology Fast Forward. Published on October 5, 2015 as DOI: 10.1124/mol.115.100917
This article has not been copyedited and formatted. The final version may differ from this version.

between Arg955, Glu836, and Asp927 (3.1-3.5Å) that allow the key nuclease catalytic residues Tyr892, Arg905, Asn906, and His910 to be poised for action (Fig. 5D). Asp847, His909, Arg905 are highly conserved residues across multiple species (Dong et al., 2001). These interactions across the RNase dimer interface are also analogous to those observed previously for the activation of yeast Ire1 RNase activity by quercetin (3LJ0; Wiseman et al., 2010). In the structure of pIRE1α-GSK2850163, the RNase domains are separated; thus, the network of H-bonds between the RNase domains observed in the active pIRE1α+STS dimer does not exist (Fig. 5C). Hence, the data from the co-crystal structures presented here suggest that the formation of interdigitating H-bonds and the stabilization of the RNase dimer are critical for the active RNase conformation and its enzymatic activity.

Molecular Pharmacology Fast Forward. Published on October 5, 2015 as DOI: 10.1124/mol.115.100917
This article has not been copyedited and formatted. The final version may differ from this version.

DISCUSSION

Recent work has implicated the UPR in a number of diseases, most notably in cancer where UPR activation has been shown to function as a survival mechanism in cancer promoting tumor growth, regulating angiogenesis, and facilitating adaptation to hypoxia (Ma and Hendershot, 2004; Feldman et al., 2005; Chen et al., 2014). Specifically, the IRE1α/XBP1 pathway has shown to be overexpressed in a variety of human cancers, and activation of the pathway has been shown to be essential for the survival of highly secretory multiple myeloma cells where the protein load is high (Koong et al., 2006; Feldman et al., 2005; Carrasco et al., 2007). These key findings, coupled with the possibility to modulate IRE1α activity via targeting two potentially druggable domains, has made IRE1α a very attractive target in drug discovery (Hetz et al., 2013; Maly and Papa, 2014; Harrington et al., 2014; Sanches et al., 2014; Joshi et al., 2015).

An increasing body of evidence indicates that IRE1α inhibitors bound to the kinase domain invariably inhibit its ATPase activity, yet some kinase inhibitors inhibit the RNase activity while others activate its RNase activity. GSK2850163 was discovered in an attempt to identify IRE1α-selective inhibitors of XBP1 splicing that could regulate multiple myeloma cancer cells. It is a highly selective kinase inhibitor; a panel of 284 kinases was assayed to determine the specificity of GSK2850163, and only two additional kinases were weakly inhibited by GSK2850163: Ron (IC50 = 4.4 μM), and FGFR1 V561M (IC50 = 17 μM) (Supplementary Table 1). GSK2850163 inhibits IRE1α RNase activity due to the unique way the molecule binds in the kinase domain active site. GSK2850163 binds deep in a pocket next to the kinase αC helix, approximately 12 Å from the hinge region which is clearly distinct from the

Molecular Pharmacology Fast Forward. Published on October 5, 2015 as DOI: 10.1124/mol.115.100917
This article has not been copyedited and formatted. The final version may differ from this version.

ADP binding site. The molecule adopts a U-shape conformation when bound to pIRE1α that could only be achieved with the *R*-stereoisomer (Supplementary Fig. 2A). Modeling of the *S*-stereoisomer places the di-fluoro benzene outside the electron density and clashes with the protein. Similarly, flipping the U-shaped molecule to the reverse orientation places the spirodecane within the electron density, but the 4-bond length between the spirodecane and the tolyl group leads to a clash with Leu616 and the 2-bond length is too short and causes a clash between the di-fluoro benzene and Lys599 instead of the H-bond when in the modeled orientation. Based on this and the SAR studies performed, it is clear that only the *R*-stereoisomer in the modeled conformation and orientation is capable of fitting the electron density, avoiding clashes, and engaging with Glu612 and Lys599.

The GSK2850163 mode of binding differs from classic ATP-competitive inhibitors (reviewed in Dar and Shokat, 2011). Inhibitors exemplified by APY29 (DFG-in and the αC helix in the active conformation), activate IRE1α RNase activity (Korennykh et al., 2009; Wang et al., 2012). In contrast, inhibitors like KIRA6 and several close analogs inhibit IRE1α kinase and RNase activities and possibly prevent dimer association (Wang et al., 2012; Ghosh et al., 2014). While co-crystal structures for KIRA6 are not available, a close analog was recently co-crystallized with the c-Src kinase domain demonstrating a shift in the αC-helix 'out' to the inactive conformation (PDB ID 3QLF). Thus, it is possible that KIRA6 invokes a similar conformational change when bound to IRE1α. Similarly, another inhibitor recently described by Amgen potently inhibited IRE1α kinase and RNase activity and was co-crystallized with a dephosphorylated IREα monomer (Harrington et al., 2014). The lack of IRE1α dimer structure here could be due to the compound either preventing dimerization or stabilizing a monomeric form of IRE1α. While previously it was suggested that dimerization/oligomerization occurs after

Molecular Pharmacology Fast Forward. Published on October 5, 2015 as DOI: 10.1124/mol.115.100917
This article has not been copyedited and formatted. The final version may differ from this version.

autophosphorylation, recent crystal structures of dephosphorylated human IRE1α dimers demonstrate that dimerization can precede phosphorylation in both "face-to-face" and "back-to-back" configurations (Ali et al., 2011; Joshi et al., 2015). It should also be noted that this molecule shifted the αC-helix 'out.' Hence, one commonality between this molecule, GSK2850163, and the KIRA6 analogs, is that all these inhibitors shift the αC-helix to an inactive conformation which may likely be a requirement for IRE1α RNase inactivation.

Aside from kinase domain inhibitors, two other classes of IRE1α inhibitors have been characterized that target other potential drug pockets in the IRE1α protein: quercetin and salicylaldehyde-based inhibitors. Quercetin binds uniquely to yeast Ire1 in a pocket at the enzyme-dimer interface termed the Q-site, thereby stabilizing Ire1 in an active conformation that augments RNase activity (Wiseman et al., 2010). While quercetin has been shown to be a broad spectrum kinase inhibitor and may potentially target the nucleotide binding site of Ire1, it did not inhibit Ire1 autophosphorylation. Independently, a considerable amount of work has been conducted to target IRE1α RNase activity directly (Maly and Papa, 2014; Sanches et al., 2014). These salicylaldehyde-based inhibitors contain a reactive electrophile that most likely covalently modifies Lys907 at the IRE1α RNase active site. It is believed that these inhibitors should not affect IRE1α autophosphorylation or dimerization. GSK2850163 is the first molecule that inhibits both kinase and RNase activity by binding to phosphorylated IRE1α and inducing a unique long-range conformation change which alters the preferred enzyme structure for RNA substrate binding.

The wealth of data on the dimeric/oligomeric state of IRE1as a function of phosphorylation and the effects of various classes of kinase inhibitors does not fully explain the

Molecular Pharmacology Fast Forward. Published on October 5, 2015 as DOI: 10.1124/mol.115.100917
This article has not been copyedited and formatted. The final version may differ from this version.

details of the conformational changes required to cause modulation of IRE1α RNase activity. The hydrogen-deuterium exchange (HDX) rate, which is dependent on both structural and conformational changes, is very well suited to reveal these details and has the resolution necessary to pinpoint the required conformational changes in solution state. Our HDX data is consistent with the model of RNase inhibition suggested by the pIRE1α-GSK2850163 co-crystal structure. The differences observed in labeling overlap with the changes observed in the crystal state. The critical observation of the conserved salt bridge between Arg627 and Asp620 in the kinase domain being disrupted by GSK2850163 is highly consistent with the changes in the αC helix to the 'out' (inactive) conformation and the reorientation of the pIRE1α dimer to the inactive form. By the same analysis, the reverse is true in the activation of the RNase.

A comparison of the yeast Ire1 "back to back" dimers with the human pIRE1α-STS dimer demonstrates that the kinase domain DFG-loop is in the "in" conformation, the αC helix is in the active conformation, and the RNase domains are engaged through a network of H-bond interactions in these structures that coincide with conditions of RNase activation. Minor differences are observed between the pIRE1α+STS dimer and the three yeast Ire1 structures (PDB IDs 2RIO; 3FBV; 3LJ0) (r.m.s. on Cα = 1.9-2.1Å); however, differences are even greater when comparisons are made with the pIRE1α-GSK2850163 dimer (r.m.s. on Cα = 3.3-3.4Å). GSK2850163 binding results in shifting the structure of the kinase domain to the DFG-out, αC helix inactive conformation, and the RNase domains of the dimer are rotated away from each other. This indicates that the RNase active forms of yeast and human IRE1 are markedly different from the RNase inactive pIRE1α-GSK2850163 dimer. While the key interactions in the RNase domains are not mediated by identical residues across species, they are essential.

Molecular Pharmacology Fast Forward. Published on October 5, 2015 as DOI: 10.1124/mol.115.100917
This article has not been copyedited and formatted. The final version may differ from this version.

Mutagenesis studies have shown that these interfacial residues are critical for maintaining RNase activity (Lee et al., 2008).

Structural similarities are also observed between the human phosphorylated (4YZD) and dephosphorylated (3P23) IRE1α-ADP-Mg^{2+} structures (r.m.s. on Cα = 0.5Å). In both cases, the dimers are "face-to-face" with the RNase domains separated in an inactive conformation. Likewise, pIRE1α-ADP-Mg^{2+} and mouse IRE1 complexed with the RNase domain inhibitor, MKC9989, (4PL3) are similar in dimeric structure (r.m.s on Cα = 0.8Å). The largest differences are located in a loop formed by residues 654-659 in the kinase domain. This stretch of amino acids is engaged in intermolecular contacts within the neighboring molecule of the asymmetric unit in the ADP complex. It is worth noting that previous *in vitro* studies have shown that ADP bound to IRE1α can affect dimerization and/or reduce RNase activity of both mouse and human IRE1α (Prischi et al., 2014; Sanches et al., 2014).

The pIRE1α-GSK2850163 and pIRE1α-STS co-crystal structures were also compared to two recently reported human "back-to-back" dimers of IRE1α: one in apo form (4Z7G) and one in an inhibitor-bound form (4Z7H). In these two structures, the RNase domains are not engaging with each other across the dimer interface and more closely resemble the pIRE1α+GSK2850163 dimer (overall dimer r.m.s. on Cα = 1.6Å) than the pIRE1α+STS dimer (overall dimer r.m.s. on Cα = 2.7Å). Despite this, the imidazopyridine molecule, compound 3, interacts with the hinge and the activation loop (DFG-in) in a similar fashion as staurosporine (r.m.s. on Cα = 0.9Å) and behaves as a type I kinase inhibitor (Joshi et al., 2015). GSK2850163 and compound 3 do not occupy overlapping pockets. This structural observation is at odds with other type I inhibitor bound IRE1 structures. A comparison of the IRE1α apo and IRE1α-imidazopyridine complex

Molecular Pharmacology Fast Forward. Published on October 5, 2015 as DOI: 10.1124/mol.115.100917
This article has not been copyedited and formatted. The final version may differ from this version.

indicates that they are nearly identical (r.m.s. on Ca = 0.6A). This discrepancy may be due to the way the experiments were performed, namely that the inhibitor-bound form was resolved by soaking into the pre-formed apo crystals as opposed to performing co-crystallization.

The characterization of the first co-crystal structure of human phosphorylated IRE1α and its complex with a new class of kinase inhibitor has revealed a novel mode of action for the inhibition of pIRE1α kinase and RNase activity. The comparisons made between known structures across various species and with inhibitors that have differential effects on IRE1α RNase activity should provide insights into the molecular mechanisms responsible for activation and inhibition of IRE1α RNase activity. These new data should also provide a feasible path to enable the design and use of pharmacological agents that differentially affect IRE1α/XBP1 signaling.

Coordinates for the pIRE1α+GSK2350163, pIRE1α+ADP, and pIRE1α+STS co-crystal structures have been deposited to the Protein Data Bank with the respective accession codes: PDB ID 4YZ9, 4YZD, and 4YZC.

Molecular Pharmacology Fast Forward. Published on October 5, 2015 as DOI: 10.1124/mol.115.100917
This article has not been copyedited and formatted. The final version may differ from this version.

ACKNOWLEDGEMENTS

We would like to thank the members of the IRE1α drug discovery program and the Computational and Structural Chemistry Department for fruitful discussions and insightful comments on the manuscript.

AUTHOR CONTRIBUTIONS

Participated in research design: Evans, Heerding, Buser, Su, DeYoung

Conducted experiments: Concha, Smallwood, Bonnette, Totoritis, Federowicz, Campobasso, Choudhry, Shuster, Evans, Su, DeYoung

Contributed new reagents or analytic tools: Qi, Chen, Sweitzer, Shuster, Evans, Ralph

Performed data analysis: Concha, Smallwood , Totoritis, Zhang, Yang, Choudhry, Heerding, Su, DeYoung

Wrote or contributed to the writing of the manuscript: Concha, Buser, Su, DeYoung

Molecular Pharmacology Fast Forward. Published on October 5, 2015 as DOI: 10.1124/mol.115.100917
This article has not been copyedited and formatted. The final version may differ from this version.

REFERENCES

Ali MM, Bagratuni T, Davenport EL, Nowak PR, Silva-Santisteban MC, Hardcastle A, McAndrews C, Rowlands MG, Morgan GJ, and Aherne W et al. (2011) Structure of the Ire1 autophosphorylation complex and implications for the unfolded protein response. *EMBO J* **30**:894-905.

Afonine PV, Mustyakimov M, Grosse-Kunstleve RW, Moriarty NW, Langan P, and Adams PD (2010) Joint X-ray and neutron refinement with phenix.refine. *Acta Cryst D Biol Crystallogr* **66:**1153-1163.

Bagratuni T, Wu P, Gonzalez de Castro D, Davenport EL, Dickens NJ, Walker BA, Boyd K, Johnson DC, Gregory W, and Morgan GJ et al. (2010) XBP1s levels are implicated in the biology and outcome of myeloma mediating different clinical outcomes to thalidomide-based treatments. *Blood* **116**:250-253.

Calfon M, Zeng H, Urano F, Till JH, Hubbard SR, Harding HP, Clark SG, and Ron D (2002) IRE1 couples endoplasmic reticulum load to secretory capacity by processing the XBP-1 mRNA. *Nature* **415**:92-96.

Carrasco DR, Sukhdeo K, Protopopova M, Sinha R, Enos M, Carrasco DE, Zheng M, Mani M, Henderson J, and Pinkus GS et al. (2007) The differentiation and stress response factor XBP-1 drives multiple myeloma pathogenesis. *Cancer Cell* **11**:349-360.

Chen VB, Arendall WB 3rd, Headd JJ, Keedy DA, Immormino RM, Kapral GJ, Murray LW, Richardson JS, and Richardson DC (2010) MolProbity: all-atom structure validation for macromolecular crystallography. *Acta Cryst D Biol Crystallogr* **66**:12-21.

Chen X, Iliopoulos D, Zhang Q, Tang Q, Greenblatt MB, Hatziapostolou M, Lim E, Tam WL, Ni M, and Chen Y et al. (2014) XBP1 promotes triple-negative breast cancer by controlling the HIF1α pathway. *Nature* **508**:103-107.

Cross BC, Bond PJ, Sadowski PG, Jha BK, Zak J, Goodman JM, Silverman RH, Neubert TA, Baxendale IR, and Ron D et al. (2012) The molecular basis for selective inhibition of unconventional mRNA splicing by an IRE1-binding small molecule. *Proc Natl Acad Sci USA* **109**:E869-E878.

Dar AC and Shokat KM (2011) The evolution of protein kinase inhibitors from antagonists to agonists of cellular signaling. *Annu Rev Biochem* **80**:769-795.

Dong B, Niwa M, Walter P, and Silverman RH (2001) Basis for regulated RNA cleavage by functional analysis of RNase L and Ire1p. *RNA* **7**:361-373.

Emsley PP and Cowtan K (2004) Features and development of Coot. *Acta Cryst D Biol Crystallogr* **66**:486-501.

Molecular Pharmacology Fast Forward. Published on October 5, 2015 as DOI: 10.1124/mol.115.100917
This article has not been copyedited and formatted. The final version may differ from this version.

Englander JJ, Del Mar C, Li W, Englander SW, Kim JS, Stranz DD, Hamuro Y, and Woods VL Jr. (2003) Protein structure change studied by hydrogen-deuterium exchange, functional labeling, and mass spectrometry. *Proc Natl Acad Sci USA* **100**:7057-7062.

Feldman DE, Chauhan V, and Koong AC (2005) The unfolded protein response: a novel component of the hypoxic stress response in tumors. *Mol Cancer Res* **3**:597-605.

Ghosh R, Wang L, Wang ES, Perera BG, Igbaria A, Morita S, Prado K, Thamsen M, Caswell D, and Macias H et al. (2014) Allosteric inhibition of the IRE1α RNase preserves cell viability and function during endoplasmic reticulum stress. *Cell* **158**:534-548.

Harding HP, Calfon M, Urano F, Novoa I, and Ron D (2002) Transcriptional and translational control in the mammalian unfolded protein response. *Annu Rev Cell Dev Biol* **18**:575-599.

Harrington PE, Biswas K, Malwitz D, Tasker AS, Mohr C, Andrews KL, Dellamaggiore K, Kendall R, Beckmann H, and Jaeckel P et al. (2014) Unfolded Protein Response in Cancer: IRE1α Inhibition by Selective Kinase Ligands Does Not Impair Tumor Cell Viability. *ACS Med Chem Lett* **6**:68-72.

Hetz C, Chevet E, and Harding HP (2013) Targeting the unfolded protein response in disease. N*at Rev Drug Discov* **12**:703-719.

Hollien J and Weissman JS (2006) Decay of endoplasmic reticulum-localized mRNAs during the unfolded protein response. *Science* **313**:104-107.

Joshi A, Newbatt Y, McAndrew PC, Stubbs M, Burke R, Richards MW, Bhatia C, Caldwell JJ, McHardy T, and Collins I et al. (2015) Molecular mechanisms of human IRE1 activation through dimerization and ligand binding. *Oncotarget* Apr 18. [Epub ahead of print].

Koong AC, Chauhan V, and Romero-Ramirez L (2006) Targeting XBP-1 as a novel anti-cancer strategy. *Cancer Biol Ther* **5**:756-759.

Korennykh AV, Egea PF, Korostelev AA, Finer-Moore J, Zhang C, Shokat KM, Stroud RM, and Walter P (2009) The unfolded protein response signals through highorder assembly of Ire1. *Nature* **457**:687-693.

Kornev AP and Taylor SS (2010) Defining the conserved internal architecture of a protein kinase. *Biochim Biophys Acta* **1804**:440-444.

Lee AH, Iwakoshi NN, and Glimcher LH (2003) XBP-1 regulates a subset of endoplasmic reticulum resident chaperone genes in the unfolded protein response. *Mol Cell Biol* **23**:7448-7459.

Lee K, Tirasophon W, Shen X, Michalak M, Prywes R, Okada T, Yoshida H, Mori K, and Kaufman RJ (2002) IRE1-mediated unconventional mRNA splicing and S2P-mediated ATF6 cleavage merge to regulate XBP1 in signaling the unfolded protein response. *Genes Dev* **16**:452-466.

Lee KP, Dey M, Neculai D, Cao C, Dever TE, and Sicheri F (2008) Structure of the dual enzyme Ire1 reveals the basis for catalysis and regulation in nonconventional RNA splicing. *Cell* **132**:89-100.

Ma Y and Hendershot LM (2004) The role of the unfolded protein response in tumor development: friend or foe?. *Nat Rev Cancer* 4:966-977.

Maly DJ and Papa FR (2104) Druggable sensors of the unfolded protein response. *Nat Chem Biol* **10**:892-901.

Murshudov GNG, Vagin AA, and Dodson EJ (1997) Refinement of macromolecular structures by the maximum-likelihood method. *Acta Cryst D Biol Crystallogr* **53**:240-255.

Nakamura M, Gotoh T, Okuno Y, Tatetsu H, Sonoki T, Uneda S, Mori M, Mitsuya H, and Hata H (2006) Activation of the endoplasmic reticulum stress pathway is associated with survival of myeloma cells. *Leuk Lymphoma* **47**:531-539.

Percy AJ, Rey M, Burns KM, and Shriemer DC (2012) Probing protein interactions with hydrogen/deuterium exchange and mass spectrometry-a review. *Anal Chim Acta* **721**:7-21.

Prischi F, Nowak PR, Carrara M, and Ali MM (2014) Phosphoregulation of Ire1 RNase splicing activity. *Nat Commun* **5**:doi: 10.1038/ncomms4554.

Reimold AM, Iwakoshi NN, Manis J, Vallabhajosyula P, Szomolanyi-Tsuda E, Gravallese EM, Friend D, Grusby MJ, Alt F, and Glimcher LH (2001) Plasma cell differentiation requires the transcription factor XBP-1. *Nature* **412**:300-307.

Ron D (2002) Translational control in the endoplasmic reticulum stress response. *J Clin Invest* **110**:1383-1388.

Rouschop KM, van den Beuken T, Dubois L, Niessen H, Bussink J, Savelkouls K, Keulers T, Mujcic H, Landuyt W, and Voncken JW, et al. (2010) The unfolded protein response protects human tumor cells during hypoxia through regulation of the autophagy genes MAP1LC3B and ATG5. *J Clin Invest* **120**:127-141.

Sanches M, Duffy NM, Talukdar M, Thevakumaran N, Chiovitti D, Canny MD, Lee K, Kurinov I, Uehling D, and Al-awar R et al. (2014) Structure and mechanism of action of the hydroxy–aryl–aldehyde class of IRE1 endoribonuclease inhibitors. *Nat Commun* **5:**doi: 10.1038/ncomms5202.

Schroder M and Kaufman RJ (2005) The mammalian unfolded protein response, *Annu Rev Biochem* **74**:739-789.

Tirasophon W, Welihinda AA, and Kaufman RJ (1998) A stress response pathway from the endoplasmic reticulum to the nucleus requires a novel bifunctional protein kinase/endoribonuclease (Ire1p) in mammalian cells. *Genes Dev* **12**:1812-1824.

Urano F, Wang X, Bertolotti A, Zhang Y, Chung P, Harding HP, and Ron D (2000) Coupling of stress in the ER to activation of JNK protein kinases by transmembrane protein kinase IRE1. *Science* **287**:664-666.

Walter P and Ron D (2011) The unfolded protein response: from stress pathway to homeostatic regulation. *Science* **334**:1081-1086.

Wang L, Perera BG, Hari SB, Bhhatarai B, Backes BJ, Seeliger MA, Schürer SC, Oakes SA, Papa FR, and Maly DJ (2012) Divergent allosteric control of the IRE1alpha endoribonuclease using kinase inhibitors. *Nat Chem Biol* **8**:982-989.

Wang Y, Shen J, Arenzana N, Tirasophon W, Kaufman RJ, and Prywes R (2000) Activation of ATF6 and an ATF6 DNA binding site by the endoplasmic reticulum stress response. *J Biol Chem* **275**:27013-27020.

Wasilko DJ and Lee SE (2006) TIPS: Titerless Infected-Cells Preservation and Scale-Up. *BioProc J* **5**:29-32.

Winn MD, Ballard CC, Cowtan KD, Dodson EJ, Emsley P, Evans PR, Keegan RM, Krissinel EB, Leslie AG, and McCoy A (2011) Overview of the CCP4 suite and current developments. *Acta Cryst D Biol Crystallogr* **67**:235-242.

Wiseman RL, Zhang Y, Lee KP, Harding HP, Haynes CM, Price J, Sicheri F, and Ron D (2010) Flavonol activation defines an unanticipated ligand-binding site in the kinase-RNase domain of IRE1. *Mol Cell* **38**:291-304.

Woehlbier U and Hetz C (2011) Modulating stress responses by the UPRosome: A matter of life and death. *Trends Biochem Sci* **36**:329-337.

Yoshida H, Matsui T, Yamamoto A, Okada T, and Mori K (2001) XBP1 mRNA is induced by ATF6 and spliced by IRE1 in response to ER stress to produce a highly active transcription factor. *Cell* **107**:881-891.

Molecular Pharmacology Fast Forward. Published on October 5, 2015 as DOI: 10.1124/mol.115.100917
This article has not been copyedited and formatted. The final version may differ from this version.

FOOTNOTES

All authors are past or present employees of GlaxoSmithKline. No potential conflicts of interest were disclosed by the authors.

Molecular Pharmacology Fast Forward. Published on October 5, 2015 as DOI: 10.1124/mol.115.100917
This article has not been copyedited and formatted. The final version may differ from this version.

FIGURE LEGENDS

Fig. 1. GSK2850163 binds to human pIRE1α and inhibits XBP1 splicing. (A) GSK2850163 is a selective inhibitor of pIRE1α kinase activity and RNase activity. It exhibits no or weak inhibition towards a wide range of the other kinases (shown here is the UPR kinase, PERK) and nucleases (shown here is RNase L, its closest homolog). Refer to *Materials and Methods* for assay details. (B) Overall structure of the pIRE1α-GSK2850163 (PDB ID: 4YZ9) back-to-back dimer. Inset: chemical structure of GSK2850163 ((R)-2-(3,4-dichlorobenzyl)-N-(4-methylbenzyl)-2,7-diazaspiro[4.5]decane-7-carboxamide). (C) GSK2850163 (yellow) binds next to the αC helix and displaces the activation loop (DFG-out) such that it is occupying the ATP-binding site represented by its surface. GSK2850163 makes H-bond interactions with key kinase catalytic residues Lys599 (K599) and Glu612 (E612). (D) For comparison, the DFG loop is in the "in" conformation in the structure of pIRE1α-Mg^{2+}-ADP (PDB ID: 4YZD), and Phe712 (F712) occupies the same pocket where the GSK2850163 would bind. For both (C) and (D), the asterix (*) indicates the C-terminal end of the visible portion of the activation loop.

Fig. 2. Selected SAR results of compound **1** (GSK2850163). (A). Replacement of the urea nitrogen with a carbon atom (compound **2**) or capping the NH with a methyl group (compound **3**) caused a loss of potency. Conversion of basic amine in pyrrolidine ring to a non basic amide yielded an inactive analog (compound **4**). (B and C). The lipophilic groups at the tolyl and dichlorophenyl groups were critical for the compound's activity. On the other hand, the polar functionalities, such as pyridines, were not tolerated.

Fig. 3. Inhibition of IRE1α kinase and RNase activity in cells treated with GSK2850163. (A) Multiple myeloma cell lines were left untreated or treated with tunicamycin for 1 hour.

Molecular Pharmacology Fast Forward. Published on October 5, 2015 as DOI: 10.1124/mol.115.100917
This article has not been copyedited and formatted. The final version may differ from this version.

GSK2850163 **(**GSK163) was then added for 3 hours at the indicated doses. Total RNA was harvested and RT-PCR was performed using human-specific XBP1 primers flanking the splice site that distinguish between unspliced ($XBP1_u$) and spliced ($XBP1_s$) XBP1 mRNA. (B) RPMI 8226 cells were left untreated or treated with tunicamycin and/or GSK2850163 as described in (A). Changes in IRE1α phosphorylation were detected by western blot using a phospho-specific antibody raised against Ser 724 in the kinase activation loop. (C) XBP1s transcriptional activity is reduced in cells treated with GSK2850163**.** PANC-1 cells were transfected with a 5X UPRE luciferase reporter and pRL-SV40 renilla constructs. 48 hours later, cells were left untreated or treated with tunicamycin for 1 hour, followed by GSK2850163 treatment for 16 hours. UPRE luciferase expression was measured and normalized to renilla expression levels.

Fig, 4. Structure and activity of the human pIRE1α-STS (STS) complex. (A) STS inhibits pIRE1α kinase activity but not RNase activity. (B) Titration curve showing that the nuclease activity of dephosphorylated IRE1α (IRE1α (-P)) is stimulated by STS in the RNase assay. (C) STS induces XBP1 splicing in RPMI 8826 cells. Cells were treated with STS for 30 minutes, followed by tunicamycin (tuni, 5ug/mL) treatment in half of the cells for 1 hour. Total RNA was harvested and RT-PCR was performed using human-specific XBP1 primers flanking the splice site that distinguish between unspliced ($XBP1_u$) and spliced ($XBP1_s$) XBP1 mRNA. (D) STS inhibits tunicamycin-induced IRE1α phosphorylation. RPMI 8226 cells were treated as described in (c). Changes in IRE1α phosphorylation were detected by western blot using a phospho-specific antibody raised against Ser 724 in the kinase activation loop. (E) pIRE1α-STS dimer (PDB ID: 4YZC) in the back-to-back configuration with STS bound in the ATP-binding site.

Molecular Pharmacology Fast Forward. Published on October 5, 2015 as DOI: 10.1124/mol.115.100917
This article has not been copyedited and formatted. The final version may differ from this version.

Fig. 5. Conformational changes to pIRE1α upon ligand binding. (A) Left panel, increased interactions along the kinase dimer interface and decreased surface area contact of the RNase domains in pIRE1α + GSK2850163; Right panel, pIRE1α–STS structure where the interactions are tighter between the RNase domains. A carton model depicts a rocking motion between inactive (left) and active (right) pIRE1α dimers. (B) Residues 610-619 that make up the αC helix move 4.4 Å ± 1.0 between pIRE1α-STS (green) and pIRE1α-GSK2850163 (salmon). The structures of the kinase domains were superimposed using Cα atoms of the residues forming the hinge region. (C) Bottom-up view of the pIRE1α-GSK2850163 RNase domains. There is one pair of residues interacting across the RNase dimer interface which covers a contact area of 269Å^2. Glu913 on chain A (green) and Arg905 on chain B (cyan) form a salt bridge, but the equivalent interaction (i.e., Glu913 of chain B and Arg905 of chain A) is not possible because the side chain of Glu913 in chain B is disordered. (D) Bottom-up view of the pIRE1α-STS RNase domains. There are two sets of interdigitating H-bond interactions, the first set involves His909, Asp847 and Arg905 (3.2-3.5Å), and the second is between Arg955, Glu836, and Asp927 (3.1-3.5Å). (E) Calculated buried surface area of contact for the two pIRE1α dimers and the individual domains.

(Data Supplement 1) Crystal Structure of human phosphorylated IRE1alpha in complex with a type III kinase inhibitor (GSK2850163A) (PDB ID: 4YZ9).

(Data Supplement 2) Crystal Structure of human phosphorylated IRE1alpha in complex with ADP- Mg^{2+} (PDB ID: 4YZD).

(Data Supplement 3) Crystal structure of pIRE1alpha in complex with staurosporine (PDB ID: 4YZC).

Molecular Pharmacology Fast Forward. Published on October 5, 2015 as DOI: 10.1124/mol.115.100917
This article has not been copyedited and formatted. The final version may differ from this version.

TABLES

Table 1. Data collection and refinement statistics (molecular replacement)

	pIRE1α+GSK2850163	pIRE1α + ADP	pIRE1α + STS
Data collection			
Space group	*$P2_12_12$*	*C2*	*$P2_12_12_1$*
Cell dimensions			
a, *b*, *c* (Å)	244.0, 77.8, 88.3	191.8, 122.5, 77.9	49.3, 155.3, 155.6
α, β, γ (°)	90, 90, 90	90.0, 107.1, 90.0	90, 90, 90
Molecules/a.u.	3	3	2
Resolution (Å)	2.45 (2.54 – 2.45)	3.14 (3.25 – 3.10)	2.62 (2.71 – 2.62)
R_{sym} or R_{merge}	0.073 (0.592)	0.087 (0.569)	0.118 (0.565)
$I / \sigma I$	22.9 (3.1)	15.2 (2.4)	22.7 (5.6)
Completeness (%)	96.7 (89.7)	100.0 (100.0)	100.0 (100.0)
Redundancy	6.3 (6.3)	3.8 (3.8)	11.8 (11.6)
Refinement			
Resolution (Å)	30.0 – 2.45	45.6 – 3.14	40.0 – 2.62
No. reflections	59,654	60,654	41,900
R_{work} / R_{free}	0.24/0.29	0.20/0.25	0.25/0.29
No. atoms			
Protein	17,853	9.822	12,041
Ligand/ion	90	90	70
Water	81	35	62
B-factors			
Protein	57	31	55
Ligand/ion	57	24	23
Water	51	10	48
R.m.s. deviations			
Bond lengths (Å)	0.007	0.008	0.002
Bond angles (°)	0.93	1.09	1.15

Note: Values in parentheses are for highest-resolution shell.

Each dataset was collected from a single crystal

Figure 1.

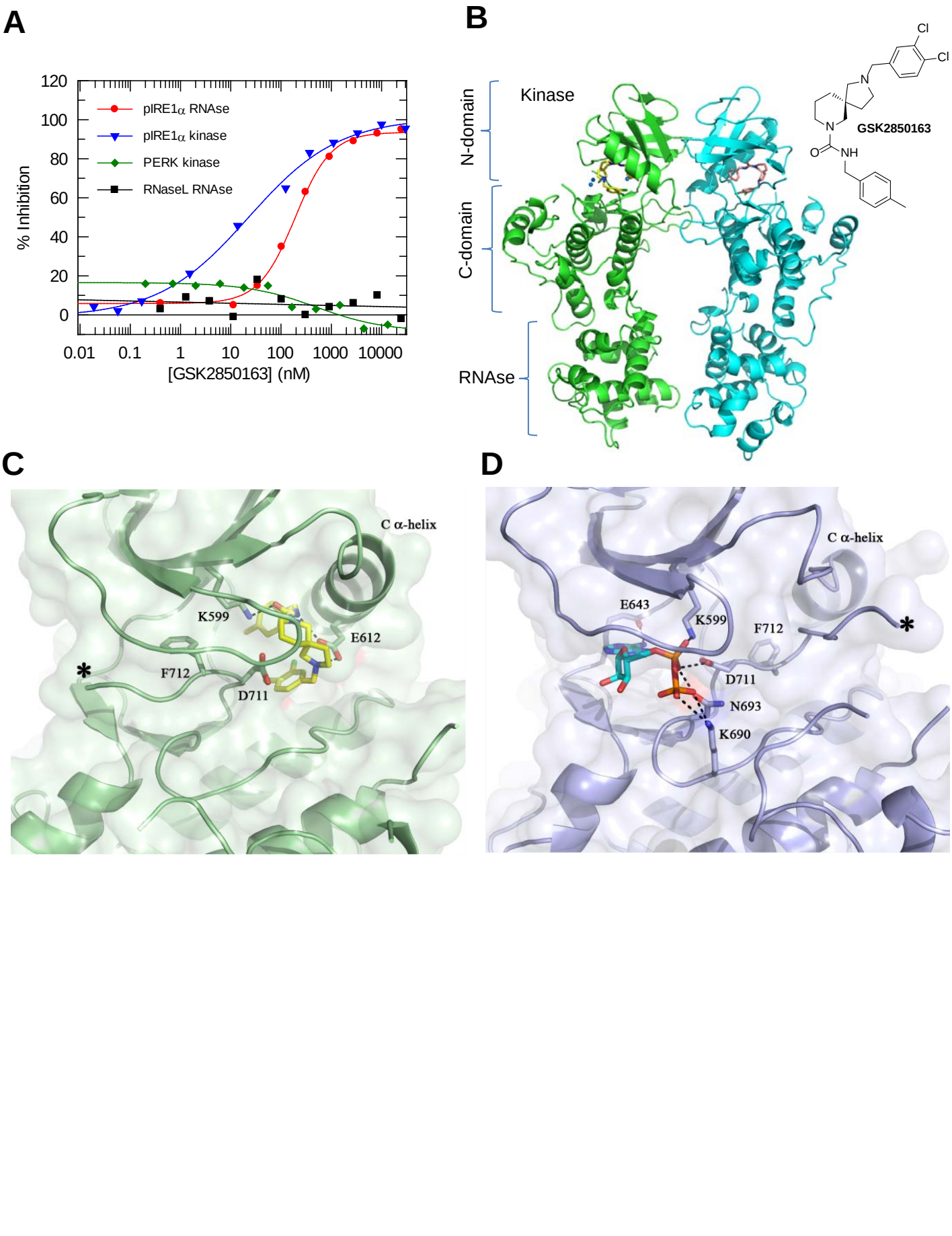
A
120
100
80
60
40
20
0
% Inhibition
pIRE1α RNAse
pIRE1α kinase
PERK kinase
RNaseL RNAse
0.01
0.1
1
10
100
1000
10000
[GSK2850163] (nM)
B
Kinase
N-domain
C-domain
RNAse
Cl
Cl
N
N
O
NH
GSK2850163
C
C α-helix
K599
E612
F712
D711
*
D
C α-helix
E643
K599
F712
D711
N693
K690
*

Figure 2.

A

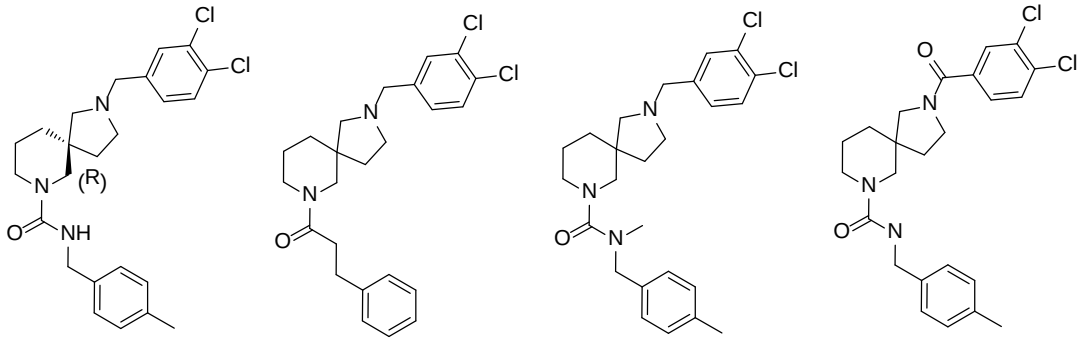

1, GSK2850163
RNase IC50: 0.20 μM

2
RNase IC50: > 50 μM

3
RNase IC50: > 25 μM

4
RNase IC50: > 25 μM

B

SAR Results of B-ring Aryl group

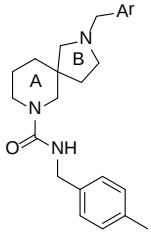

Comp #	Ar	RNase IC_{50} (μM)
1	3,4-diClPh	0.20
5	4-Me-3-pyridyl	>25
6	4-Cl-2-pyridyl	>25
7	3-ClPh	10
8	4-ClPh	0.40
9	4-MePh	1.0
10	4-CF_3Ph	0.32
11	4-Cl, 3-FPh	0.25
12	4-Cl, 3-MePh	0.32
13	4-Cl, 3-OMePh	0.20
14	4-Cl, 3-CF_3Ph	10

C

SAR Results of A-ring Aryl group

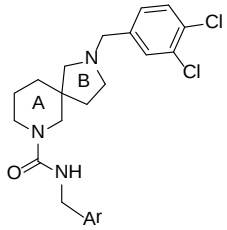

Comp #	Ar	RNase IC_{50} (μM)
1	4-MePh	0.20
15	4-pyridyl	6.3
16	3-pyridyl	7.9
17	2-pyridyl	12.5
18	4-Me-3-pyridyl	12.5
19	4-Me-2-pyridyl	10
20	Ph	0.40
21	4-ClPh	0.50
22	4-OMePh	0.50
23	4-F Ph	0.79
24	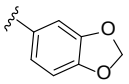	0.1

Figure 3.

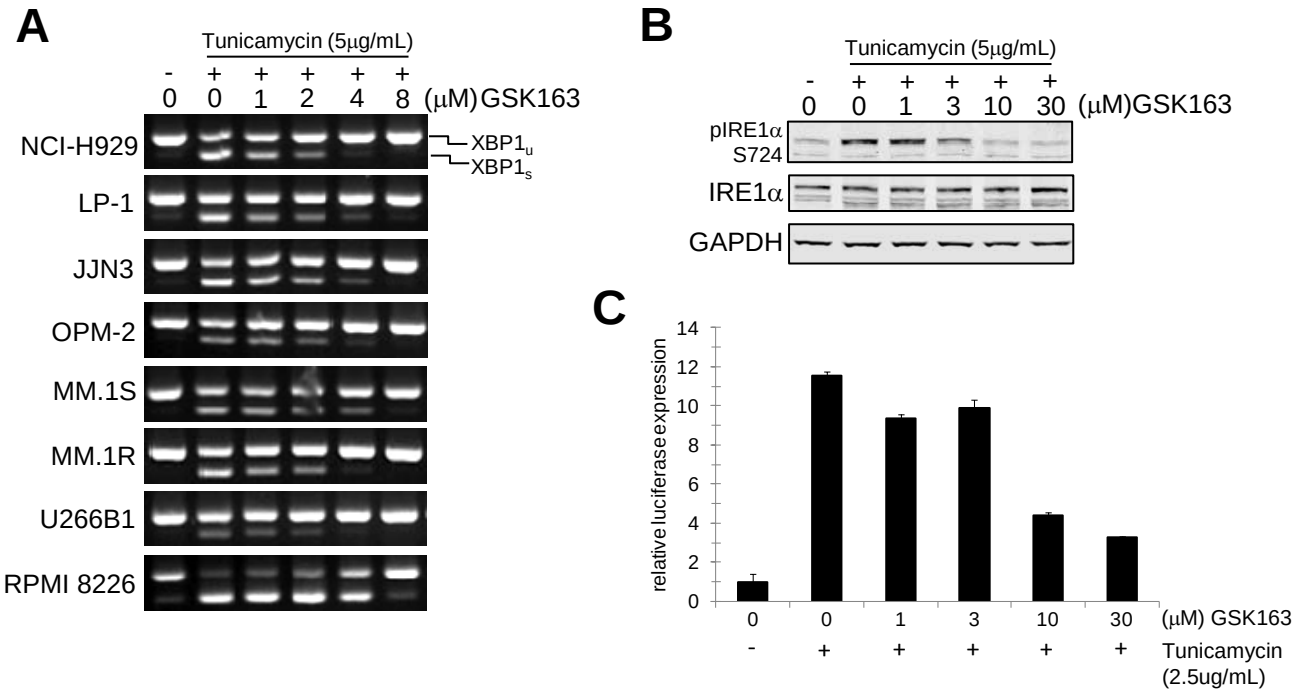
A
Tunicamycin (5μg/mL)
- + + + + +
0 0 1 2 4 8 (μM)GSK163
NCI-H929
LP-1
JJN3
OPM-2
MM.1S
MM.1R
U266B1
RPMI 8226
XBP1u
XBP1s
B
Tunicamycin (5μg/mL)
- + + + + +
0 0 1 3 10 30 (μM)GSK163
pIRE1α S724
IRE1α
GAPDH
C
relative luciferase expression
0 2 4 6 8 10 12 14
0 0 1 3 10 30 (μM) GSK163
- + + + + + Tunicamycin (2.5ug/mL)

Figure 4.

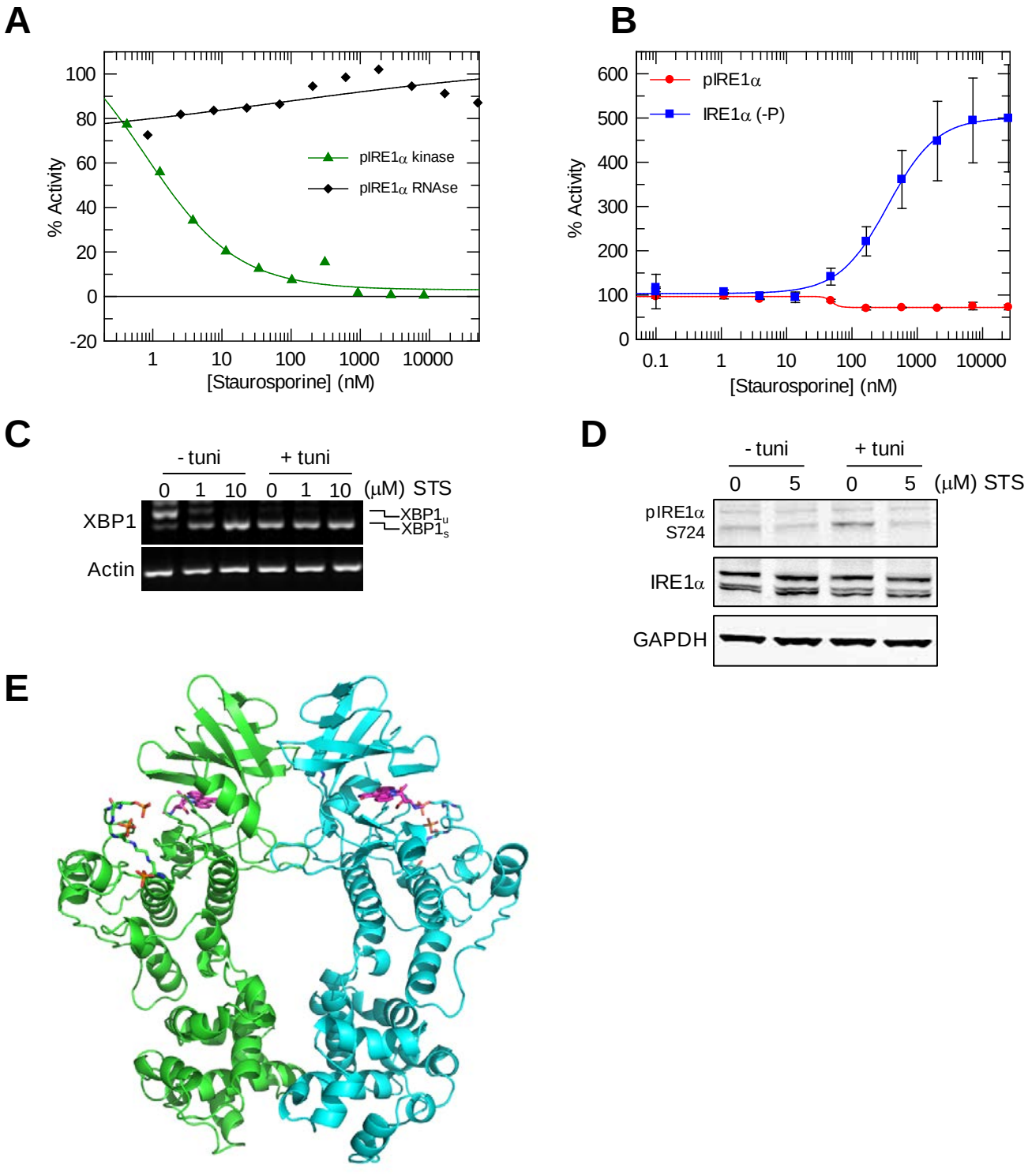
A
100
80
60
40
20
0
-20
% Activity
pIRE1α kinase
pIRE1α RNAse
1
10
100
1000
10000
[Staurosporine] (nM)
B
600
500
400
300
200
100
0
% Activity
pIRE1α
IRE1α (-P)
0.1
1
10
100
1000
10000
[Staurosporine] (nM)
C
- tuni
+ tuni
0 1 10 0 1 10 (μM) STS
XBP1
XBP1u
XBP1s
Actin
D
- tuni
+ tuni
0 5 0 5 (μM) STS
pIRE1α
S724
IRE1α
GAPDH
E

Figure 5.

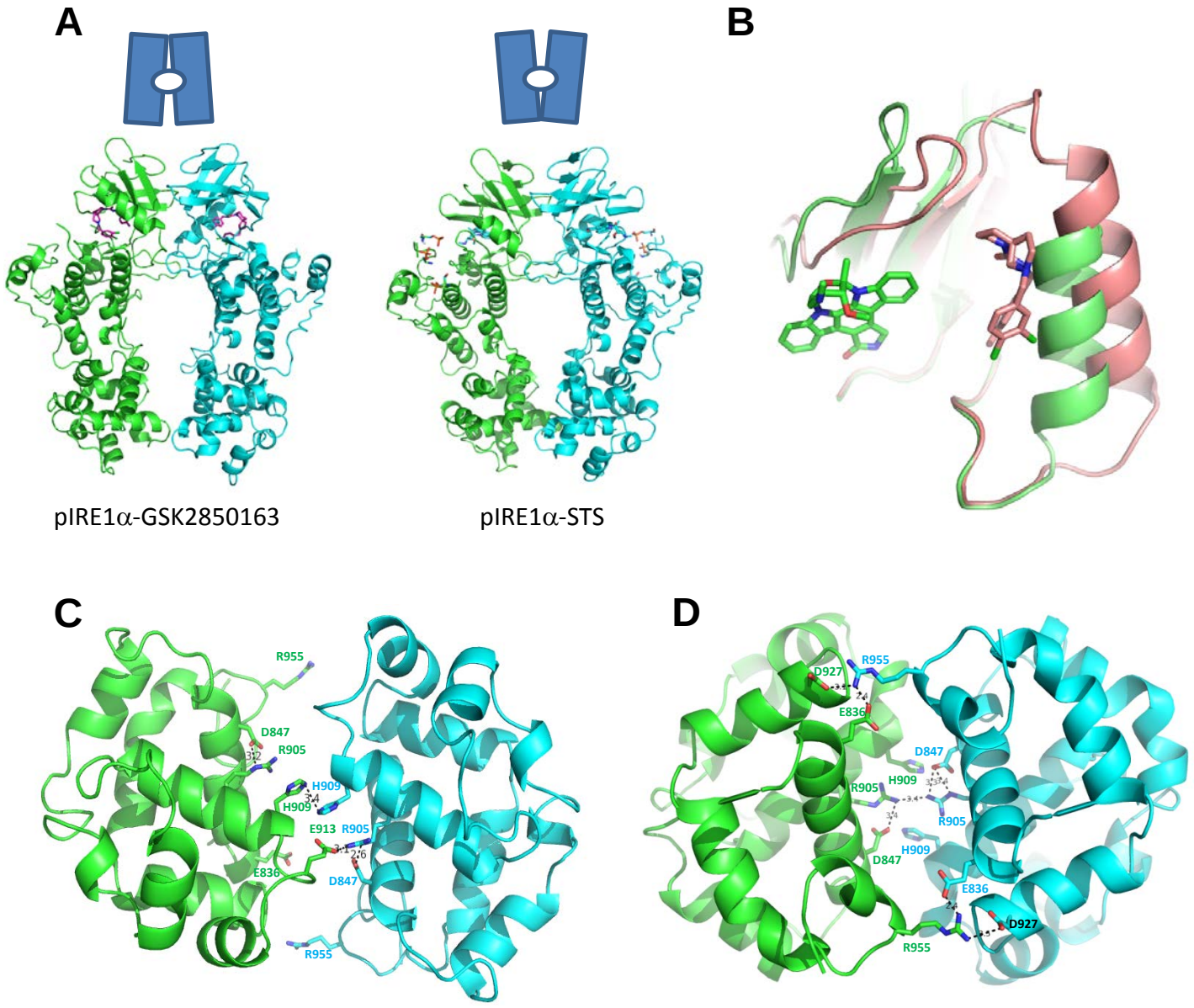

E

	Surface area of contact	
	GSK2850163	STS
Kinase domain	1,734 Å^2	1,461 Å^2
RNase domain	269 Å^2	642 Å^2
Dimer	2,003 Å^2	2,103 Å^2

SUPPLEMENTARY INFORMATION

Long-range inhibitor-induced conformational regulation of human IRE1α endoribonuclease activity

Nestor O. Concha, Angela Smallwood, William Bonnette, Rachel Totoritis, Guofeng Zhang, Kelly Federowicz, Jingsong Yang, Hongwei Qi, Stephanie Chen, Nino Campobasso, Anthony E. Choudhry, Leanna E. Shuster, Karen A. Evans, Jeff Ralph, Sharon Sweitzer, Dirk A. Heerding, Carolyn A. Buser, Dai-Shi Su, & M. Phillip DeYoung

Molecular Pharmacology

SUPPLEMENTARY METHODS

General synthetic experimental procedures

Proton Nuclear Magnetic Resonance (^{1}H NMR) spectra were recorded on a Bruker UltraShield™ 400 spectrometer operating at 400.132 MHz using a 5mm QNP probe unless otherwise specified. The 2D NMR spectra were recorded on a Bruker Avance 600 spectrometer operating at 600.13 MHz using a 5mm TXI cryoprobe. Spectra were taken in the indicated solvent at ambient temperature, and the chemical shifts are reported in parts per million (ppm (δ)) relative to the lock of the solvent used. Resonance patterns are recorded with the following notations: br (broad), s (singlet), d (doublet), t (triplet), q (quartet), and m (multiplet). Second order spectra in which coupling cannot be obtained by inspection are reported as multiplets, with the center of the signal indicated by the δ value given.

Starting reagents were purchased from commercial suppliers and were used without further purification unless otherwise specified. Microwave reactions were performed in a Biotage™ Initiator Sixty reactor using the manufacturer supplied vials and caps. Microwave reaction times are for time held at the specified temperature.

Normal phase column chromatography was carried out in the indicated solvent system (in the percentage of volume) using pre-packed silica gel cartridges (Reveleris®, Analogix® or Isco Redisep Gold) on the Analogix Intelliflash280® , Varian Intelliflash 971-FP, or Combiflash Companion purification systems. Analytical thin layer chromatography (TLC) visualization was performed using 254 nm wavelength ultraviolet light. Preparative HPLC purifications (reversed-phase) were performed using a Gilson 215 Liquid Handler with Trilution software, typically with a SunFire(TM) Prep C18 OBD(TM) 5 μM, 30 mm x 50 mm column. A 7 min gradient followed

by a 3 min 100% organic hold time (47 mL/min, 30% gradient of ACN/H_2O, 0.1%TFA) with UV detection at 254 nm was typically used.

LCMS M+H signals were consistent with expected molecular weight for all reported products. LCMS data were acquired from a Waters Acquity Ultra Performance LC system with UV detector (Waters Acquity PDA) set to 210-350 nm. Samples were injected (0.2 μL) onto a Thermo Hypersil Gold column (C18, 20x2.1 mm, 1.9 u particle diam.) maintained at 55 °C. A linear gradient (1.9 min) from 2% to 95% B (MeCN/H_2O, 0.02% TFA) with a flow rate of 1.6 mL/min was used. The mass spectra (MS) data were acquired in positive ion mode using a Water Acquity SQD (single quadrupole) mass spectrometer with a positive electrospray ionization source.

The compounds in Fig. 2B were prepared straightforwardly according to the route depicted in Scheme 1. Urea formation of the commercially available N2-Boc protected diazospirodecane in the presence of isocyanate followed by acid deprotection afforded the key intermediate. Reductive amination of intermediate with the corresponding aldehyde delivered the desired analogs. Compound 3 and the compounds in Fig. 2C were prepared similarly from the other Boc protected diazaspirodecane starting material with the reverse of steps of urea formation and reductive amination as depicted in Scheme 1. In the case that isocyanate is not commercially available, the urea formation was carried out by the action of triphosgene with the corresponding amines or microwave-assisted phenyl carbamate formation following by the treatment with the corresponding amines.

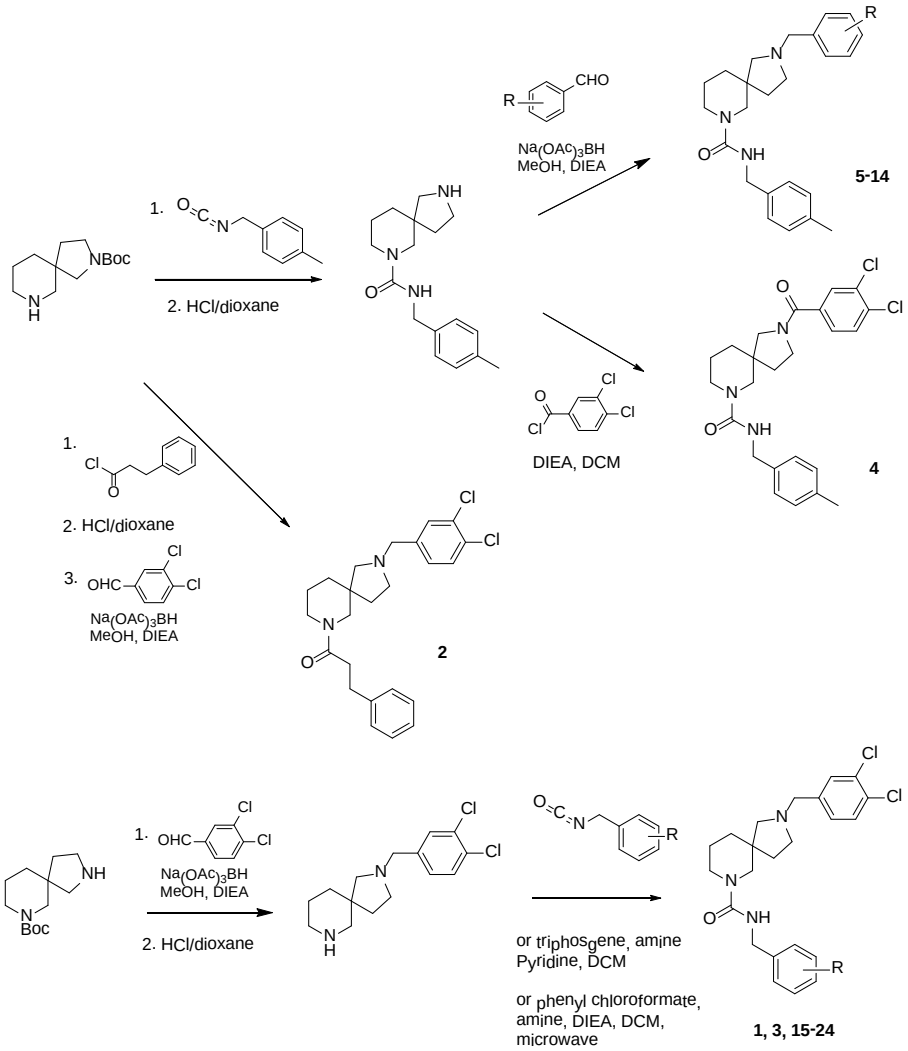

Scheme 1. General Synthetic Route

Preparation and characterization of compounds 1-24

(R)-2-(3,4-dichlorobenzyl)-N-(4-methylbenzyl)-2,7-diazaspiro[4.5]decane-7-carboxamide (1). To a solution of tert-butyl 2,7-diazaspiro[4.5]decane-7-carboxylate (500 mg, 2.080 mmol) and 3,4-dichlorobenzaldehyde (364 mg, 2.080 mmol) in methanol (5 mL) was added sodium triacetoxyborohydride (882 mg, 4.16 mmol). The reaction mixture was stirred at room temperature overnight under N_2. The reaction mixture was concentrated in vacuo. The

residue was taken up in EtOAc (~50 mL) and the resulting solution was washed with 3 x H_2O, sat. $NaHCO_3$, and brine. The organic layer was dried with $MgSO_4$, filtered, and concentrated to give 809 mg of crude material. The residue was subjected to normal phase purification using the ISCO Combiflash. The compound was eluted through a 12 g Analogix silica column, with a 0-40% gradient of EtOAc and hexane. The desired fractions were combined and concentrated to give tert-butyl 2-(3,4-dichlorobenzyl)-2,7-diazaspiro[4.5]decane-7-carboxylate (566.3 mg, 1.418 mmol, 68 % yield) as a colorless oil. LC/MS (ES) m/z = 399 $(M+H)^+$, ^1H NMR (400 MHz, CHLOROFORM-*d*) δ ppm 1.46 (s, 11 H), 1.50 - 1.75 (m, 8 H), 2.08 - 2.61 (m, 2 H), 2.71 (br. s., 1 H), 3.43 (m, *J*=3.0 Hz, 1 H), 3.54 (br. s., 1 H), 7.13 - 7.26 (m, 1 H), 7.39 (d, *J*=8.3 Hz, 1 H), 7.42 - 7.49 (m, 1 H). Tert-butyl 2-(3,4-dichlorobenzyl)-2,7-diazaspiro[4.5]decane-7-carboxylate (500 mg, 1.252 mmol) and HCl, 4M in dioxane (4 mL, 16.00 mmol) were combined and stirred at room temperature. After 1 h, the reaction mixture was concentrated in vacuo. The residue was taken up in tetrahydrofuran (THF) (10 mL). To this solution were added DIEA (0.656 mL, 3.76 mmol) and 1-(isocyanatomethyl)-4-methylbenzene (0.175 mL, 1.252 mmol). The reaction mixture stirred at room temperature under N_2 overnight. After 19 h, the reaction mixture was concentrated by rotary evaporation. The residue was taken up in ~25 mL EtOAc and the resulting solution was washed with H_2O (3x). The combined aqueous layers were extracted with 10 mL EtOAc (2x). The combined organics were dried with $MgSO_4$, filtered, and concentrated to give 607 mg of crude material. The residue was subjected to normal phase purification using the Analogix IntelliFlash 280. The compound was eluted through a 40 g ISCO Redisep Gold silica column, with a 0-40% gradient of 90:9:1 chloroform:MeOH:ammonium hydroxide (aq) and chloroform. The desired fractions were combined and concentrated to give 2-(3,4-dichlorobenzyl)-N-(4-methylbenzyl)-2,7-diazaspiro[4.5]decane-7-carboxamide (496 mg, 1.11

mmol, 89% yield). LC/MS (ES) m/z = 446 $(M+H)^+$. After chiral separation by HPLC, using 10:90 EtOH:Heptane on AD column with 0.1 isopropylamine as basic modifier, the product was obtained (130 mg, 95% ee, 100% by LCMS, second peak). LC/MS (ES) m/z = 446.5 $(M+H)^+$; ^{1}H NMR (400 MHz, DMSO-d_6) δ ppm 1.30 - 1.61 (m, 6 H) 2.06 - 2.12 (m, 1 H) 2.25 (s, 3 H) 2.37 - 2.46 (m, 2 H) 2.62 (td, *J*=8.27, 5.43 Hz, 1 H) 3.11 (d, *J*=12.88 Hz, 1 H) 3.15 - 3.23 (m, 1 H) 3.23 - 3.32 (m, 2 H) 3.49 - 3.58 (m, 2 H) 4.17 (d, *J*=5.81 Hz, 2 H) 6.92 (t, *J*=5.81 Hz, 1 H) 7.03 - 7.13 (m, 4 H) 7.31 (dd, *J*=8.34, 2.02 Hz, 1 H) 7.51 - 7.56 (m, 2 H). LC/MS (ES) m/z = 446.5 $(M+H)^+$ VCD analysis showed that the product was the R enantiomer.

1-(2-(3,4-dichlorobenzyl)-2,7-diazaspiro[4.5]decan-7-yl)-3-phenylpropan-1-one (2). LCMS (ES) m/z 431.4 $(M+H)^+$, ^{1}H NMR (400 MHz, DMSO-d_6) δ ppm 1.20 - 1.34 (m, 1 H) 1.34 - 1.64 (m, 5 H) 1.92 - 2.05 (m, 1 H) 2.23 - 2.48 (m, 2 H) 2.51 - 2.75 (m, 3 H) 2.75 - 2.84 (m, 2 H) 2.92 - 3.06 (m, 1 H) 3.23 - 3.32 (m, 1 H) 3.35 - 3.45 (m, 1 H) 3.45 - 3.60 (m, 2 H) 3.78 (m, *J*=13.20, 4.90, 4.90 Hz, 1 H) 7.12 - 7.25 (m, 5 H) 7.25 - 7.34 (m, 1 H) 7.39 - 7.50 (m, 1 H) 7.50 - 7.60 (m, 1 H).

2-(3,4-dichlorobenzyl)-N-methyl-N-(4-methylbenzyl)-2,7-diazaspiro[4.5]decane-7-carboxamide (3). LC-MS (ES) m/z 460.4 $(M+H)^+$, ^{1}H NMR (400 MHz, DMSO-d_6) δ ppm 1.35 - 1.61 (m, 6 H), 2.05 (d, *J*=9.3 Hz, 1 H), 2.27 (s, 3 H), 2.30 - 2.39 (m, 1 H), 2.58 (s, 3 H), 2.64 (td, *J*=8.7, 4.8 Hz, 1 H), 2.92 (d, *J*=12.4 Hz, 1 H), 2.96 - 3.05 (m, 1 H), 3.11 (m, *J*=12.1 Hz, 2 H), 3.33 (s, 1 H), 3.44 - 3.58 (m, 2 H), 4.15 - 4.27 (m, 2 H), 7.08 - 7.14 (m, 4 H), 7.27 (dd, *J*=8.2, 2.1 Hz, 1 H), 7.51 (d, *J*=2.0 Hz, 1 H), 7.54 (d, *J*=8.3 Hz, 1 H).

2-(3,4-dichlorobenzoyl)-N-(4-methylbenzyl)-2,7-diazaspiro[4.5]decane-7-carboxamide (4). LC-MS (ES) m/z 460.5 $(M+H)^+$, ^{1}H NMR (DMSO-d6, 400MHz): δ (ppm) 7.59-7.79 (m, 2H),

7.42-7.54 (m, 1H), 7.02-7.14 (m, 4H), 6.93-7.00 (m, 1H), 4.04-4.24 (m, 2H), 3.36-3.63 (m, 4H), 3.19-3.31 (m, 2H), 2.92-3.18 (m, 2H), 2.20-2.30 (m, 3H), 1.17-1.83 (m, 6H).

N-(4-methylbenzyl)-2-((6-methylpyridin-3-yl)methyl)-2,7-diazaspiro[4.5]decane-7-carboxamide (5). LC-MS (ES) m/z 393.5 $(M+H)^+$, ^{1}H NMR (400 MHz, DMSO-d_6) δ ppm 1.29 - 1.60 (m, 6 H) 2.08 (d, *J*=8.84 Hz, 1 H) 2.26 (s, 3 H) 2.35 - 2.47 (m, 5 H) 2.56 - 2.65 (m, 1 H) 3.08 - 3.31 (m, 4 H) 3.51 (s, 2 H) 4.16 (d, *J*=5.81 Hz, 2 H) 6.91 (t, *J*=5.81 Hz, 1 H) 7.09 (q, *J*=7.92 Hz, 4 H) 7.17 (d, *J*=8.08 Hz, 1 H) 7.57 (dd, *J*=7.83, 2.02 Hz, 1 H) 8.34 (d, *J*=1.77 Hz, 1 H).

2-((5-chloropyridin-2-yl)methyl)-N-(4-methylbenzyl)-2,7-diazaspiro[4.5]decane-7-carboxamide (6). LC-MS (ES) m/z 413.1 $(M+H)^+$, ^{1}H NMR (400 MHz, DMSO-d_6) δ ppm 1.29 - 1.62 (m, 6 H) 2.12 (d, *J*=9.09 Hz, 1 H) 2.25 (s, 3 H) 2.43 - 2.49 (m, 3 H) 2.64 - 2.75 (m, 1 H) 3.05 - 3.25 (m, 3 H) 3.58 - 3.73 (m, 2 H) 4.17 (d, *J*=5.56 Hz, 2 H) 6.93 (t, *J*=5.56 Hz, 1 H) 7.01 - 7.16 (m, 4 H) 7.48 (d, *J*=8.34 Hz, 1 H) 7.79 (dd, *J*=8.34, 2.53 Hz, 1 H) 8.51 (d, *J*=2.27 Hz, 1 H).

2-(3-chlorobenzyl)-N-(4-methylbenzyl)-2,7-diazaspiro[4.5]decane-7-carboxamide (7). LC-MS (ES) m/z 412.5 $(M+H)^+$, ^{1}H NMR (400 MHz, DMSO-d_6) δ ppm 1.30 - 1.62 (m, 6 H), 2.08 (d, 1 H), 2.25 (s, 3 H), 2.42 (d, *J*=8.8 Hz, 2 H), 2.56 - 2.69 (m, 1 H), 3.10 - 3.30 (m, 4 H), 3.54 (br. s., 2 H), 4.17 (d, *J*=5.8 Hz, 2 H), 6.89 - 6.97 (m, 1 H), 7.04 - 7.09 (m, 2 H), 7.09 - 7.14 (m, 2 H), 7.24 - 7.38 (m, 4 H).

2-(4-chlorobenzyl)-N-(4-methylbenzyl)-2,7-diazaspiro[4.5]decane-7-carboxamide (8). LC/MS (ES) m/z = 412.4 $(M+H)^+$, ^{1}H NMR (400 MHz, DMSO-d_6) δ ppm 1.30 - 1.60 (m, 6 H) 2.06 (d, *J*=9.09 Hz, 1 H) 2.26 (s, 3 H) 2.37 - 2.45 (m, 2 H) 2.61 (td, *J*=8.21, 5.81 Hz, 1 H)

3.08 - 3.15 (m, 1 H) 3.15 - 3.22 (m, 1 H) 3.22 - 3.31 (m, 2 H) 3.47 - 3.57 (m, 2 H) 4.16 (d, *J*=5.56 Hz, 2 H) 6.91 (t, *J*=5.81 Hz, 1 H) 7.04 - 7.14 (m, 4 H) 7.29 - 7.36 (m, 4 H).

N,2-bis[(4-methylphenyl)methyl]-2,7-diazaspiro[4.5]decane-7-carboxamide (9). LC-MS (ES) m/z 392.5 (M+H)+, 1H NMR (400 MHz, DMSO-d_6) δ ppm 1.29 - 1.59 (m, 6 H) 2.06 (d, J=9.09 Hz, 1 H) 2.26 (s, 3 H) 2.27 (s, 3 H) 2.35 - 2.44 (m, 2 H) 2.59 (td, J=8.21, 5.56 Hz, 1 H) 3.10 - 3.16 (m, 1 H) 3.16 - 3.31 (m, 3 H) 3.47 (s, 2 H) 4.16 (d, J=5.81 Hz, 2 H) 6.91 (t, J=5.68 Hz, 1 H) 7.05 - 7.14 (m, 6 H) 7.15 - 7.20 (m, 2 H).

N-[(4-methylphenyl)methyl]-2-{[4-(trifluoromethyl)phenyl]methyl}-2,7-diazaspiro[4.5]decane-7-carboxamide (10). LC-MS (ES) m/z 446.1 (M+H)+, ^{1}H NMR (400 MHz, DMSO-d_6) δ ppm 1.29 - 1.62 (m, 6 H) 2.10 (d, *J*=9.09 Hz, 1 H) 2.25 (s, 3 H) 2.40 - 2.48 (m, 2 H) 2.65 (td, *J*=8.27, 5.43 Hz, 1 H) 3.13 (d, *J*=12.63 Hz, 1 H) 3.15 - 3.23 (m, 1 H) 3.24 - 3.31 (m, 2 H) 3.57 - 3.68 (m, 2 H) 4.16 (d, *J*=5.81 Hz, 2 H) 6.92 (t, *J*=5.81 Hz, 1 H) 7.03 - 7.08 (m, 2 H) 7.08 - 7.14 (m, 2 H) 7.53 (d, *J*=8.08 Hz, 2 H) 7.65 (d, *J*=8.08 Hz, 2 H).

2-[(4-chloro-3-fluorophenyl)methyl]-N-[(4-methylphenyl)methyl]-2,7-diazaspiro[4.5]decane-7-carboxamide (11). LC-MS (ES) m/z 430.4 (M+H)+, 1H NMR (400 MHz, DMSO-d_6) δ ppm 1.29 - 1.60 (m, 6 H) 2.04 - 2.10 (m, 1 H) 2.25 (s, 3 H) 2.37 - 2.47 (m, 2 H) 2.60 - 2.69 (m, 1 H) 3.10 (d, J=12.63 Hz, 1 H) 3.13 - 3.21 (m, 1 H) 3.25 - 3.32 (m, 2 H) 3.48 - 3.60 (m, 2 H) 4.16 (d, J=5.56 Hz, 2 H) 6.92 (t, J=5.81 Hz, 1 H) 7.03 - 7.08 (m, 2 H) 7.08 - 7.13 (m, 2 H) 7.18 (dd, J=8.21, 1.39 Hz, 1 H) 7.33 (dd, J=10.48, 1.89 Hz, 1 H) 7.48 (t, J=7.96 Hz, 1 H).

2-[(4-chloro-3-methylphenyl)methyl]-N-[(4-methylphenyl)methyl]-2,7-diazaspiro[4.5]decane-7-carboxamide (12). LC-MS (ES) m/z 426.5 (M+H)+, 1H NMR (400

MHz, DMSO-d_6) δ ppm 1.29 - 1.60 (m, 6 H) 2.05 (d, J=9.09 Hz, 1 H) 2.25 (s, 3 H) 2.30 (s, 3 H) 2.36 - 2.45 (m, 2 H) 2.61 (td, J=8.21, 5.56 Hz, 1 H) 3.10 (d, J=12.63 Hz, 1 H) 3.14 - 3.23 (m, 1 H) 3.23 - 3.31 (m, 2 H) 3.42 - 3.54 (m, 2 H) 4.16 (d, J=5.56 Hz, 2 H) 6.91 (t, J=5.81 Hz, 1 H) 7.03 - 7.12 (m, 4 H) 7.14 (dd, J=8.08, 1.77 Hz, 1 H) 7.27 (d, J=1.77 Hz, 1 H) 7.31 (d, J=8.08 Hz, 1 H).

2-[(4-chloro-3-methoxyphenyl)methyl]-N-[(4-methylphenyl)methyl]-2,7-diazaspiro[4.5]decane-7-carboxamide (13). LC-MS (ES) m/z 442.5 (M+H)+;^{1}H NMR (400 MHz, DMSO-d_6) δ ppm 1.30 - 1.61 (m, 6 H) 2.06 (d, *J*=9.35 Hz, 1 H) 2.25 (s, 3 H) 2.39 - 2.48 (m, 2 H) 2.61 - 2.70 (m, 1 H) 3.09 (d, *J*=12.63 Hz, 1 H) 3.13 - 3.22 (m, 1 H) 3.28 (s, 2 H) 3.45 - 3.61 (m, 2 H) 3.83 (s, 3 H) 4.16 (d, *J*=5.56 Hz, 2 H) 6.85 - 6.94 (m, 2 H) 7.02 - 7.13 (m, 5 H) 7.31 (d, *J*=7.83 Hz, 1 H).

2-{[4-chloro-3-(trifluoromethyl)phenyl]methyl}-N-[(4-methylphenyl)methyl]-2,7-diazaspiro[4.5]decane-7-carboxamide (14). LC-MS (ES) m/z 480.5 (M+H)+, ^{1}H NMR (400 MHz, DMSO-d_6) δ ppm 1.30 - 1.62 (m, 6 H) 2.11 (d, J=9.09 Hz, 1 H) 2.25 (s, 3 H) 2.38 - 2.49 (m, 2 H) 2.63 (td, J=8.21, 5.81 Hz, 1 H) 3.12 (d, J=12.88 Hz, 1 H) 3.15 - 3.23 (m, 1 H) 3.23 - 3.32 (m, 2 H) 3.56 - 3.67 (m, 2 H) 4.16 (d, J=5.81 Hz, 2 H) 6.91 (t, J=5.94 Hz, 1 H) 7.02 - 7.13 (m, 4 H) 7.63 (s, 2 H) 7.74 (s, 1 H).

2-(3,4-dichlorobenzyl)-N-(pyridin-4-ylmethyl)-2,7-diazaspiro[4.5]decane-7-carboxamide (15). LC-MS (ES) m/z 433, 435 $(M+H)^+$, ^{1}H NMR (400 MHz, DMSO-d_6) δ ppm 1.33 - 1.62 (m, 6 H), 2.10 (d, *J*=9.1 Hz, 1 H), 2.37 - 2.48 (m, 2 H), 2.60 - 2.68 (m, 1 H), 3.13 - 3.20 (m, 1 H), 3.20 - 3.31 (m, 3 H), 3.48 - 3.61 (m, 2 H), 4.23 (d, *J*=5.8 Hz, 2 H), 7.09 (t, *J*=5.9

Hz, 1 H), 7.17 - 7.23 (m, 2 H), 7.31 (dd, *J*=8.3, 2.0 Hz, 1 H), 7.52 - 7.58 (m, 2 H), 8.41 - 8.47 (m, 2 H).

2-(3,4-dichlorobenzyl)-N-(pyridin-3-ylmethyl)-2,7-diazaspiro[4.5]decane-7-carboxamide (16). LC-MS (ES) m/z 433.4 $(M+H)^+$, (^{1}H NMR 400 MHz, DMSO-d_6) δ ppm 1.33 - 1.62 (m, 6 H), 2.10 (d, *J*=9.1 Hz, 1 H), 2.37 - 2.48 (m, 2 H), 2.60 - 2.68 (m, 1 H), 3.13 - 3.20 (m, 1 H), 3.20 - 3.31 (m, 3 H), 3.48 - 3.61 (m, 2 H), 4.23 (d, *J*=5.8 Hz, 2 H), 7.09 (t, *J*=5.9 Hz, 1 H), 7.17 - 7.23 (m, 2 H), 7.31 (dd, *J*=8.3, 2.0 Hz, 1 H), 7.52 - 7.58 (m, 2 H), 8.41 - 8.47 (m, 2 H).

2-(3,4-dichlorobenzyl)-N-(pyridin-2-ylmethyl)-2,7-diazaspiro[4.5]decane-7-carboxamide (17). LC-MS (ES) m/z 433.4 $(M+H)^+$, ^{1}H NMR (400 MHz, DMSO-d_6) δ ppm 1.32 - 1.63 (m, 6 H), 2.10 (d, *J*=9.1 Hz, 1 H), 2.39 - 2.48 (m, 2 H), 2.64 (td, *J*=8.4, 5.4 Hz, 1 H), 3.13 - 3.21 (m, 1 H), 3.21 - 3.32 (m, 3 H), 3.49 - 3.60 (m, 2 H), 4.31 (d, *J*=5.8 Hz, 2 H), 7.06 (t, *J*=5.8 Hz, 1 H), 7.20 (d, *J*=7.8 Hz, 1 H), 7.21 (m, *J*=7.6 Hz, 1 H), 7.31 (dd, *J*=8.1, 2.0 Hz, 1 H), 7.51 - 7.56 (m, 2 H), 7.68 (td, *J*=7.6, 1.9 Hz, 1 H), 8.46 (dt, *J*=4.4, 1.6 Hz, 1 H)

2-(3,4-dichlorobenzyl)-N-((6-methylpyridin-3-yl)methyl)-2,7-diazaspiro[4.5]decane-7-carboxamide, (18). LC-MS (ES) m/z 447.5 $(M+H)^+$, ^{1}H NMR (400 MHz, DMSO-d_6) δ ppm 1.29 - 1.59 (m, 6 H), 2.04 - 2.10 (m, 1 H), 2.37 - 2.46 (m, 5 H), 2.57 - 2.68 (m, 1 H), 3.07 - 3.14 (m, 1 H), 3.15 - 3.32 (m, 3 H), 3.48 - 3.60 (m, 2 H), 4.17 (d, *J*=5.8 Hz, 2 H), 7.00 (t, *J*=5.7 Hz, 1 H), 7.13 (d, *J*=7.8 Hz, 1 H), 7.28 - 7.35 (m, 1 H), 7.50 (dd, *J*=8.0, 2.4 Hz, 1 H), 7.54 (m, *J*=4.0 Hz, 2 H), 8.31 (dd, *J*=2.0, 0.5 Hz, 1 H)

2-(3,4-dichlorobenzyl)-N-((5-methylpyridin-2-yl)methyl)-2,7-diazaspiro[4.5]decane-7-carboxamide (19). LC-MS (ES) m/z 447.5 $(M+H)^+$, ^{1}H NMR (400 MHz, DMSO-d_6) δ ppm 1.32 - 1.62 (m, 6 H), 2.09 (d, *J*=9.3 Hz, 1 H), 2.25 (s, 3 H), 2.38 - 2.48 (m, 2 H), 2.64 (td, *J*=8.3,

5.3 Hz, 1 H), 3.14 (d, *J*=12.6 Hz, 1 H), 3.18 - 3.32 (m, 3 H), 3.49 - 3.60 (m, 2 H), 4.26 (d, *J*=5.8 Hz, 2 H), 7.01 (t, *J*=5.8 Hz, 1 H), 7.09 (d, *J*=7.8 Hz, 1 H), 7.31 (dd, *J*=8.2, 2.1 Hz, 1 H), 7.45 - 7.50 (m, 1 H), 7.52 (d, *J*=8.3 Hz, 1 H), 7.54 (d, *J*=2.0 Hz, 1 H), 8.28 (t, 1 H)

N-benzyl-2-(3,4-dichlorobenzyl)-2,7-diazaspiro[4.5]decane-7-carboxamide (20). LC-MS (ES) m/z 432.4 $(M+H)^+$, (^{1}H NMR (400 MHz, DMSO-d_6) δ ppm 1.22 - 1.62 (m, 6 H), 2.10 (d, 1 H), 2.37 - 2.46 (m, 2 H), 2.58 - 2.66 (m, 1 H), 3.11 - 3.17 (m, 1 H), 3.18 - 3.31 (m, 3 H), 3.48 - 3.59 (m, 2 H), 4.22 (d, *J*=6.1 Hz, 2 H), 6.98 (t, *J*=5.9 Hz, 1 H), 7.16 - 7.35 (m, 6 H), 7.51 - 7.57 (m, 2 H)).

N-(4-chlorobenzyl)-2-(3,4-dichlorobenzyl)-2,7-diazaspiro[4.5]decane-7-carboxamide (21). LC-MS (ES) m/z 466.4 $(M+H)^+$, ^{1}H NMR (400 MHz, DMSO-d_6) δ ppm 1.22 - 1.61 (m, 6 H), 2.08 (d, *J*=9.6 Hz, 1 H), 2.37 - 2.46 (m, 2 H), 2.63 (q, *J*=7.5 Hz, 1 H), 3.08 - 3.16 (m, 1 H), 3.16 - 3.31 (m, 3 H), 3.47 - 3.60 (m, 2 H), 4.19 (d, *J*=5.8 Hz, 2 H), 7.02 (t, *J*=5.9 Hz, 1 H), 7.21 - 7.26 (m, 2 H), 7.28 - 7.34 (m, 3 H), 7.50 - 7.57 (m, 2 H).

2-(3,4-dichlorobenzyl)-N-(4-methoxybenzyl)-2,7-diazaspiro[4.5]decane-7-carboxamide (22). LC-MS (ES) m/z 462.4 $(M+H)^+$, (^{1}H NMR (400 MHz, DMSO-d_6) δ ppm 1.23 - 1.60 (m, 6 H), 2.05 - 2.11 (m, 1 H), 2.37 - 2.46 (m, 2 H), 2.58 - 2.66 (m, 1 H), 3.09 - 3.15 (m, 1 H), 3.15 - 3.24 (m, 1 H), 3.25 - 3.31 (m, 1 H), 3.48 - 3.59 (m, 2 H), 3.71 (s, 3 H), 4.14 (d, *J*=5.8 Hz, 2 H), 6.79 - 6.85 (m, 2 H), 6.90 (t, *J*=5.8 Hz, 1 H), 7.12 - 7.18 (m, 2 H), 7.31 (dd, *J*=8.3, 2.0 Hz, 1 H), 7.52 - 7.56 (m, 2 H)).

2-(3,4-dichlorobenzyl)-N-(4-fluorobenzyl)-2,7-diazaspiro[4.5]decane-7-carboxamide (23). LC-MS (ES) m/z 450.4 $(M+H)^+$, (^{1}H NMR (400 MHz, DMSO-d_6) δ ppm 1.22 - 1.61 (m, 6 H), 2.08 (d, 1 H), 2.37 - 2.46 (m, 2 H), 2.57 - 2.68 (m, 1 H), 3.08 - 3.16 (m, 1 H), 3.16 - 3.31 (m,

3 H), 3.46 - 3.61 (m, 2 H), 4.19 (d, *J*=5.8 Hz, 2 H), 7.00 (t, *J*=5.8 Hz, 1 H), 7.04 - 7.12 (m, 2 H), 7.22 - 7.29 (m, 2 H), 7.31 (dd, *J*=8.1, 2.0 Hz, 1 H), 7.50 - 7.57 (m, 2 H)).

N-(benzo[d][1,3]dioxol-5-ylmethyl)-2-(3,4-dichlorobenzyl)-2,7-diazaspiro[4.5]decane-7-carboxamide (24). In a glass microwave vial were placed benzo[d][1,3]dioxol-5-ylmethanamine (0.082 mL,100 mg, 0.66 mmol), Dichloromethane (DCM) (3 mL), and DIEA (0.236 mL, 1.352 mmol). To the resulting solution was added phenyl chloroformate (0.083 mL, 0.661 mmol) The vial was capped and the reaction mixture stirred at room temperature. LCMS after 15 min shows reaction completion and clean formation of desired carbamate intermediate. The reaction mixture was concentrated *in vacuo*. In a separate round bottomed flask were placed tert-butyl 2-(3,4-dichlorobenzyl)-2,7-diazaspiro[4.5]decane-7-carboxylate (600 mg, 1.50 mmol) and HCl, 4M in dioxane (5 mL, 20 mmol). The reaction mixture stirred at room temperature under nitrogen. LCMS after 30 min shows full deprotection. The reaction mixture was concentrated *in vacuo*. The residue was taken up in methanol (8 mL) and DIEA (2 mL, 11.5 mmol). The resulting solution was added to the glass microwave vial containing the carbamate intermediate. The vial was capped and heated by microwave to 100ºC for 30 min. LCMS shows reaction completion. The reaction mixture was concentrated *in vacuo*. The residue was taken up in 10 mL EtOAc and the resulting solution was washed with 1N NaOH (3 x 5 mL), H_2O (2 x 5 mL) and brine (1 x 5 mL). The organic layer was dried with Na_2SO_4, filtered, and concentrated. The residue was purified by reverse phase HPLC using a Gilson 215 Liquid Handler with Trilution software, with a SunFire™ Prep C18 OBD™ 5 uM, 30 mm x 50 mm column. A 7 min gradient was employed followed by a 3 min 100% organic hold time (47 mL/min, 20% gradient of ACN/H2O, 0.1% TFA) with UV detection at 214 nm. The desired fractions were combined and converted to the free base form by addition of sat'd $NaHCO_3$ and

extraction with EtOAc. The combined organics were combined, washed with brine, dried with Na_2SO_4, concentrated, and lyophilized to give N-(benzo[d][1,3]dioxol-5-ylmethyl)-2-(3,4-dichlorobenzyl)-2,7-diazaspiro[4.5]decane-7-carboxamide monohydrate (104.5 mg, 0.209 mmol, 55.7 % yield) as a white solid. LC-MS (ES) m/z 476.5 $(M+H)^+$, ^{1}H NMR (400 MHz, DMSO-d_6) δ ppm 1.29 - 1.60 (m, 6 H), 2.08 (d, *J*=9.3 Hz, 1 H), 2.37 - 2.46 (m, 2 H), 2.62 (td, *J*=8.5, 5.3 Hz, 1 H), 3.08 - 3.15 (m, 1 H), 3.15 - 3.32 (m, 3 H), 3.48 - 3.59 (m, 2 H), 4.12 (d, *J*=6.1 Hz, 2 H), 5.95 (m, *J*=1.5 Hz, 2 H), 6.69 (dd, *J*=7.8, 1.8 Hz, 1 H), 6.79 (dd, *J*=4.9, 3.2 Hz, 2 H), 6.92 (t, *J*=5.9 Hz, 1 H), 7.31 (dd, *J*=8.3, 2.0 Hz, 1 H), 7.54 (d, *J*=8.3 Hz, 1 H), 7.54 (d, 1 H).

VCD analysis and absolute configurationally assignment for 1 and its enantiomer

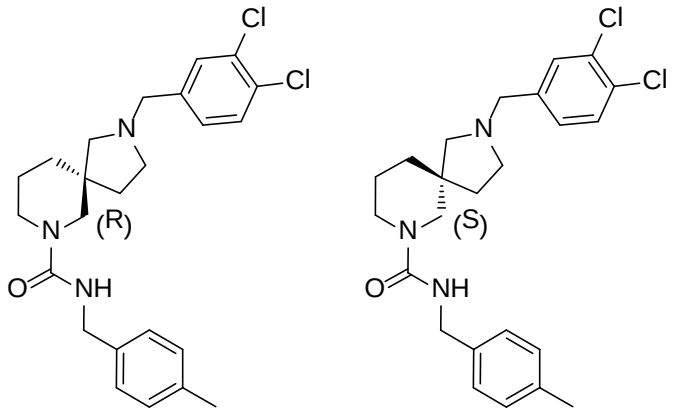

1 (GSK2850163) **the enantiomer of 1**

I. Comments:

- The configurational assignments were made using the reduced structure model shown below.
- Both phenyl rings were replaced by butadiene rings in the model.

- This replacement was made to simplify the computational analysis and is justified on the basis of conformational averaging, which would minimize contributions of either phenyl group to the experimental VCD spectra.
- Best quantitative correlation between calculated and observed VCD spectra was achieved by separating the reduced structure models into two classes: (1) folded structures, many with an intramolecular H-bond between the tertiary amine nitrogen and the secondary amide NH; (2) extended models with no intramolecular H-bonding.
- Boltzmann statistics were used to synthesize a calculated IR and VCD spectrum for each class (IR_{folded}, VCD_{folded}; $IR_{extended}$, $VCD_{extended}$)
- The VCD spectra calculated for the classes were then combined empirically to give the best correlation with experimental VCD spectra.
- The best correlation was achieved using $VCD(calc) = 0.90*VCD_{folded} + 0.10*VCD_{extended}$
- The relative intensities observed for bands due to the NH stretching vibration of free and intermolecular H-bonded NH groups were consistent with the relative amounts predicted for these classes.
- Quantitative results based on the VCD spectrum calculated for the full structure model with (S)-configuration were fully consistent with quantitative results for the reduced structure model but of lower statistical agreement with experimental VCD spectra due to less reliable predictions of VCD bands in the 1300-1150 cm^{-1} region.
- No effort was made to separate the full structure models into folded and extended classes.

II. Theoretical Analysis:

- Model:

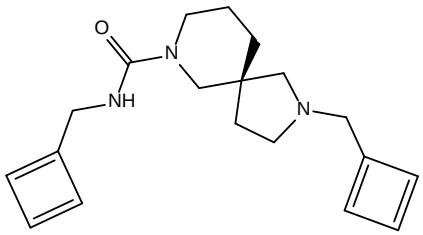

reduced structure model with (S)-configuration

- Conformational Search: MOE stochastic csearch using MMFF94x force field with Born solvation (dielectric = 75)
- Model Chemistry: # opt freq=(noraman,vcd) b3lyp/dgdzvp
- Conformational Analysis: Fractional populations estimated using Boltzmann statistics
- Lorentzian band width: 8 cm^{-1}
- Frequency scale factor: 0.980
- Estimation of Confidence Limit: CompareVOA (BioTools, Inc.) analysis (Section IX)

III. Experimental:

- Spectrometer: BioTools Chiral*IR* VCD spectrometer operated at 4 cm^{-1}
- Frequency Range: 2000-800 cm^{-1}
- PEM Calibration: PEM calibrated at 1400 cm^{-1}
- PEM Retardation Settings: PEM1 = 0.250*λ; PEM2 = 0.260*λ
- Scan Method: single block scan [2 min. DC scan + 360 min. AC scan]
- Solvent: $CDCl_3$
- Concentrations: [A2] = 11.5 mg/125ul; [A3] = 12.3mg/125ul
- Baseline Correction Method: modified half-difference (VCD_{E1} (corr'd) = VCD_{E1} minus VCD_{E2}; VCD_{E2} (corr'd) = VCD_{E2} minus VCD_{E1})

- Additional Processing: Savitsky-Golay 9-point smooth

IV. Results:

- Analysis of Experimental and Calculated Data:

  The experimental VCD and IR spectra of the enantiomer of **1** and **1** are compared with calculated data in Figures 1 and 2, respectively. The larger green box in each figure highlights the VCD spectral range used to assign the absolute configurations and estimate the level of reliability. The smaller green box indicates the spectral range omitted from consideration in this study. VCD bands in the omitted region are due to vibrational modes of the aromatic rings not present in the reduced structure model.

  In the upper panel of Figure 1, the experimental and calculated VCD spectra are largely coincident, indicating that the chiral center in this molecule has the same absolute stereochemistry as the model. Therefore, the enantiomer of **1** was assigned as the (S)-enantiomer.

  In the upper panel of Figure 2, the experimental and calculated VCD spectra are largely inverted, indicating that the chiral center in this molecule is the mirror image of the model. Therefore, **1** was assigned as the (R)-enantiomer.

  Note: The IR spectrum calculated for the model is in good overall agreement with experimental, indicating adequate coverage of the conformational space of the

stereogenic diazaspiro[4.5]decane ring, a requirement for making a reliable VCD assignment.

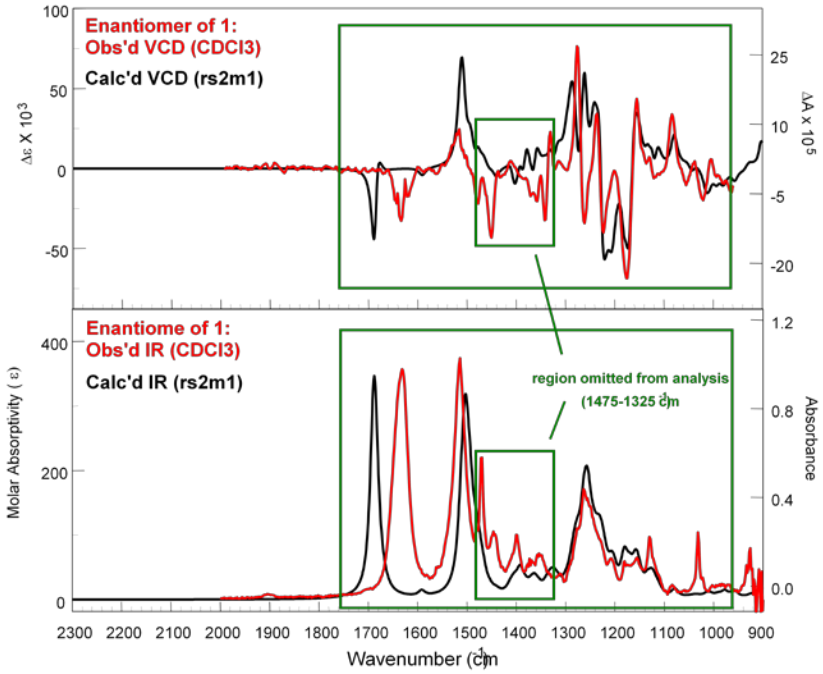

Figure 1. Upper panel: VCD spectrum of the enantiomer of **1** (red trace) vs calculated VCD spectrum (black trace). Lower panel: IR spectrum of the enantiomer of **1** (red) vs calculated IR spectrum (black).

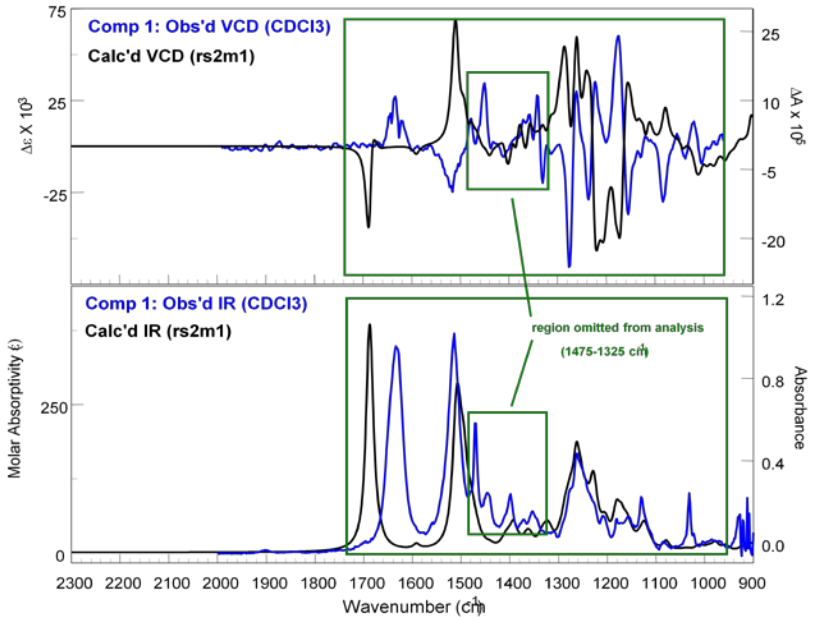

Figure 2. Upper panel: VCD spectrum of **1** (blue trace) vs calculated VCD spectrum (black trace). Lower panel: IR spectrum of **1** (blue) vs calculated IR spectrum (black).

V. Estimated Level of Reliability

- The confidence limit in this study was estimated using CompareVOA™ (BioTools, Inc.), an automated tool for quantifying the level of agreement between two sets of spectral data.
- The degree of reliability (the confidence limit) is assessed using the absolute values of two parameters: total neighborhood similarity for the VCD correlation (TNS (VCD)) and the enantiomeric similarity index (ESI).
- The degrees of reliability based on CompareVOA analysis are as follows:

Reliability	***TNS (VCD) (range)**	***ESI (range)**	**Confidence Limit (CL) (range)**
High	≥ 70	≥ 60	> 99 %
Medium	60 - 70	50 - 60	95 – 99 %
Low	50 - 60	40 – 50	90 – 95 %
Unreliable	< 50	< 40	< 90 %

*absolute value

- CompareVOA results for the current study:
    - Spectral range: 1735-960 cm^{-1}
    - Region omitted: 1475-1325 cm^{-1}
    - Range of statistical analysis (minimum 400 cm^{-1}): 625 cm^{-1}
    - Width of triangular weighting function: 30 cm^{-1}
    - TNS (VCD): 69.3 (absolute value)
    - ESI: 61.8 (absolute value)
    - Optimized scale factor: 0.980
- *Level of Reliability:* Medium-High (CL 95-99%)

SUPPLEMENTARY FIGURES

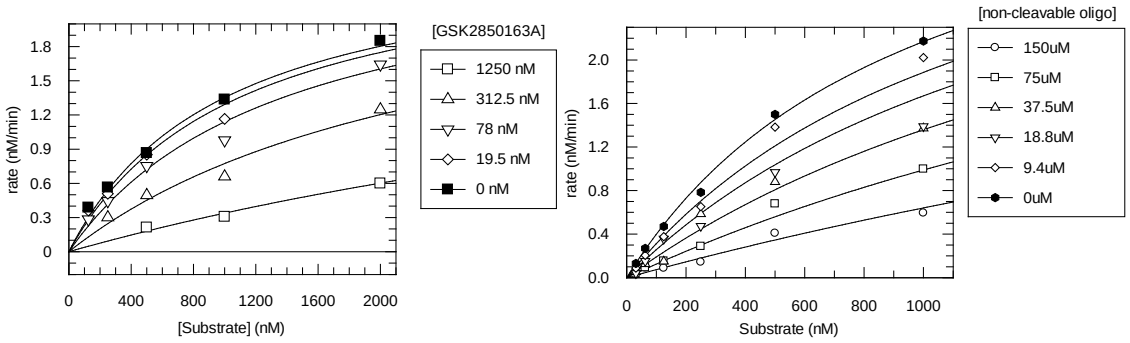

Supplementary Figure 1. Competitive inhibition studies. GSK2850163 (left) and a non-cleavable RNA substrate (right) are competitive inhibitors for pIRE1α RNase activity. Although GSK2850163 and the non-cleavable RNA substrate bind to different domains, they both behave as competitive inhibitors of pIRE1α RNase activity.

A

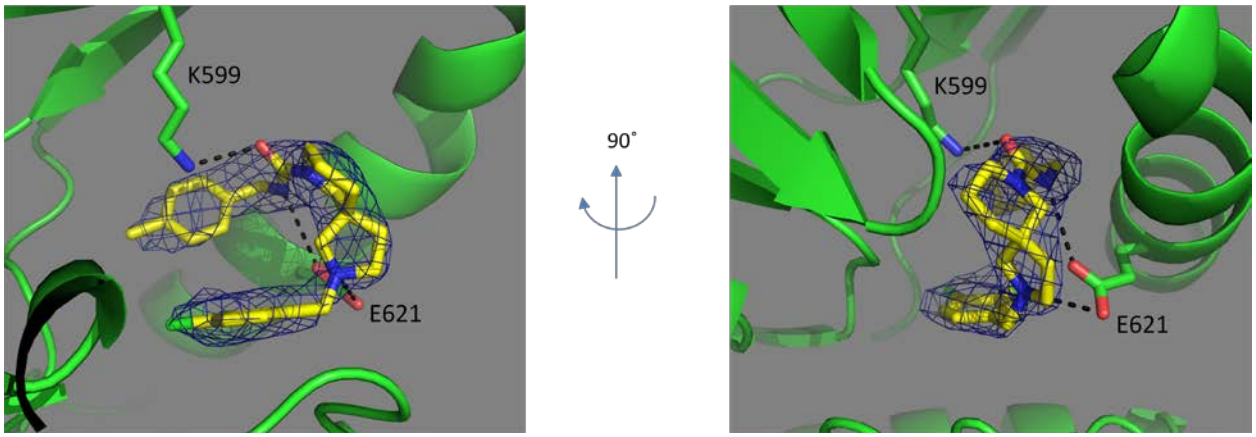

B

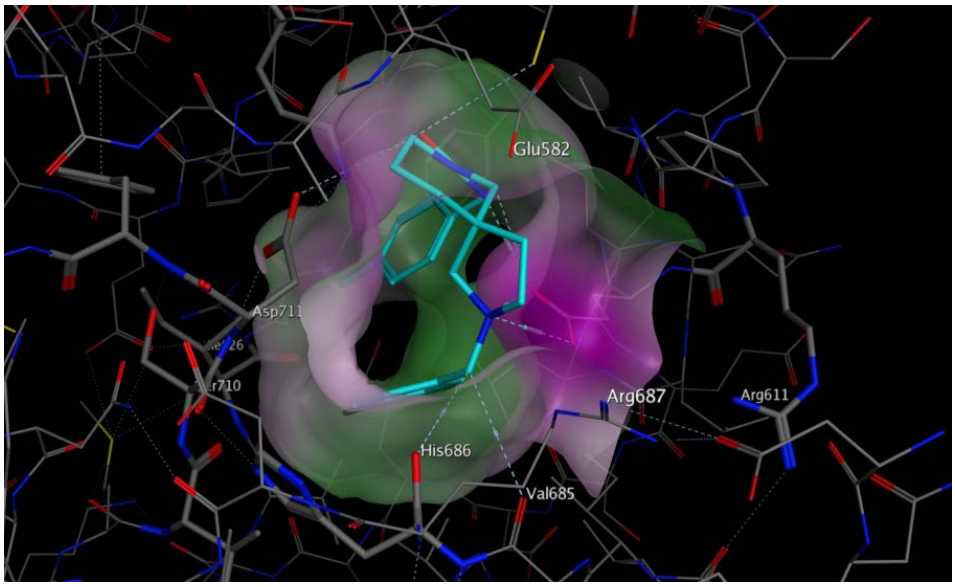

Supplementary Figure 2. pIRE1α-GSK2850163 electron density maps and binding mode. (A) Kicked omit electron density map contoured at 3σ. Ligand placement in the map was guided by the *Fo-Fc* difference map, the location of the chlorine atoms, and the H-bond interactions between the Lys599 (K599) and Glu621 (E621) of pIRE1α and GSK2850163. Only the *R*-stereoisomer fits the density. (B) Binding mode of GSK2850163 to pIRE1α. GSK2850163 in the pIRE1α binding site. GSK2850163 is colored in cyan. The nearby lipophilic and hydrophilic areas of pIRE1α are represented in green and magenta, respectively.

Supplementary Figure 3.

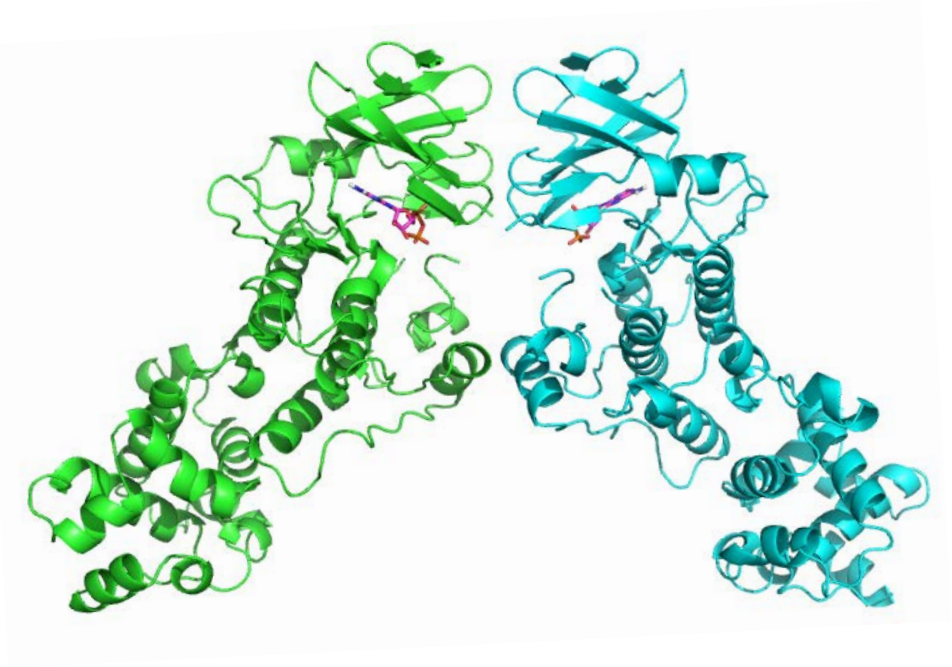

Supplementary Figure 3. Overall structure of the human pIRE1α + ADP-Mg^{2+} (PDB ID: 4YZD) face-to-face dimer. The 2-fold dimer axis coincides with the 2-fold symmetry plane in the crystal. Since there are three molecules of pIRE1α + ADP-Mg^{2+} in the asymmetric unit in this crystal form, there are three dimers as the one representative shown here. The molecule in the asymmetric unit is depicted on the right (cyan) and the partner molecule on the left (green).

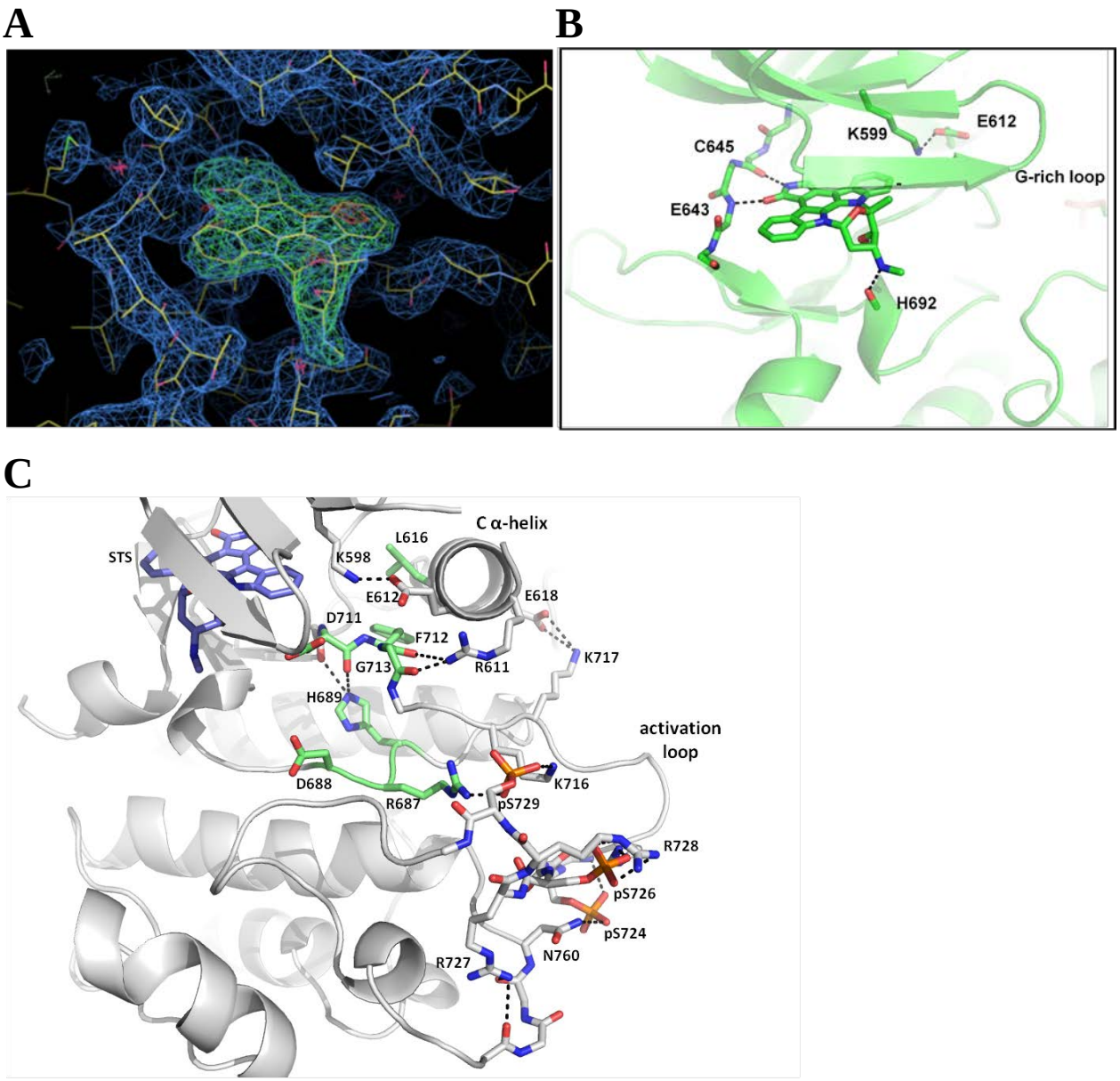

Supplementary Figure 4. Electron density map and binding mode of staurosporine (STS) to pIRE1α. (A) STS omit difference electron density map Fo-Fc contoured at 4σ (green). (B) STS interacts with hinge residues Glu643 (E643; 2.8 Å), Cys645 (C645; 2.7 Å), and His 692 (H692; 2.6 Å). (C) Active kinase conformation of pIRE1α in complex with STS. Leu616 (L616) in the αC helix interacts with the DFG loop Phe712 (F712) in the regulatory spine, and Arg687 (R687) in the kinase HRD motif interacts with Ser729 (carbon atoms colored lime). Note that the activation loop containing phosphorylated Ser residues (pS724, pS726, and pS729), previously disordered in both the pIRE1α-GSK2850163 and the pIRE1α-ADP complexes, is well defined in the pIRE1α-STS complex. A network of H-bonds extends from the serines in the activation loop to the C α-helix and into the active site DFG motif. Namely, residue Ser724 interacts with Asn750 (N750) via two H-bonds, Ser726 is involved in a H-bond interaction with Arg722 (R722; 3.1 Å) and Arg728 (R728; 3.3 Å), and Ser729 is interacting through a H-bond with Lys716 (K716; 2.7 Å) and Arg687 (R687; 2.5 Å).

A

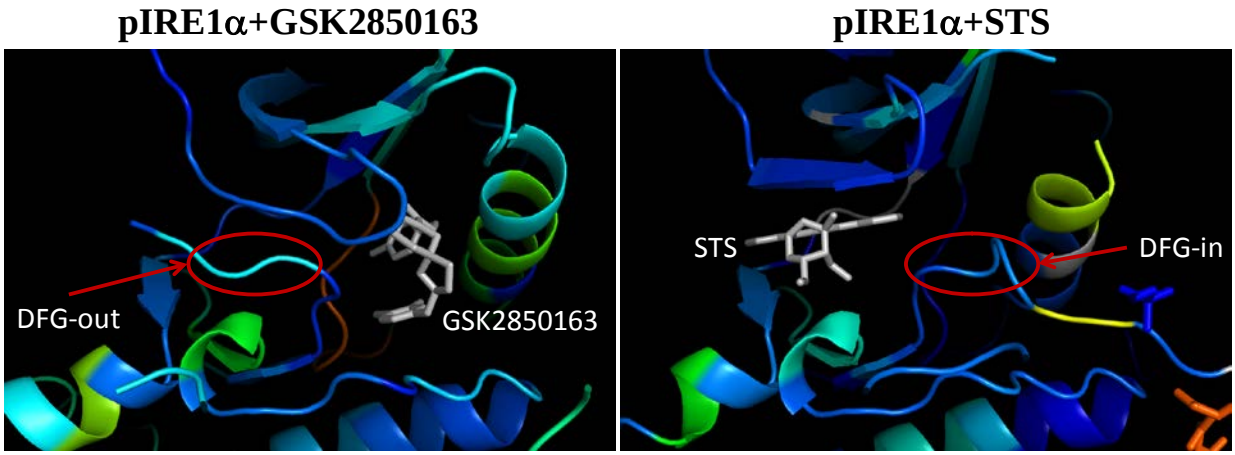

B

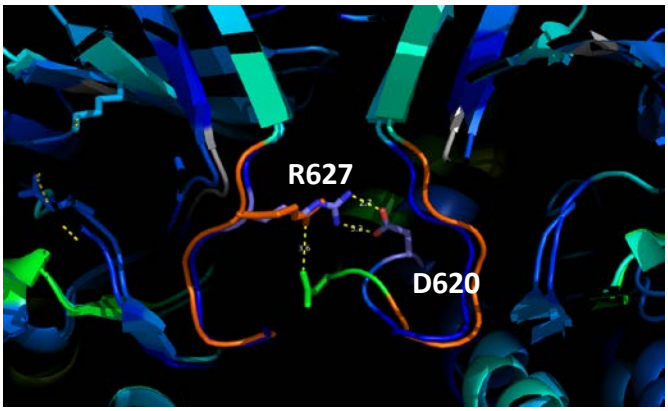

Supplementary Figure 5. Differential labeling in the Hydrogen/Deuterium Exchange (HDX). (A) Deuterium labeling is mapped onto the crystal structures of the ligand binding site and shown side-by-side for pIRE1α+GSK2850163 (left) and pIRE1α+STS (right). The activation loop at the DFG motif demonstrates increased labeling in the presence of GSK2850163, indicating more solvent exposure triggered by its displacement due to compound binding. This is consistent with the activation loop being in the DFG-out conformation as revealed by the co-crystal structure. (B) In the pIRE1α-STS complex, Arg627 forms a salt bridge with Asp620 on the partner molecule in the dimer. The disruption of this key conserved interaction by GSK2850163 is consistent with changes in the C α-helix to the inactive conformation and the reorientation of the pIRE1α dimer.

C

pIRE1α+GSK2850163 **pIRE1α+STS**

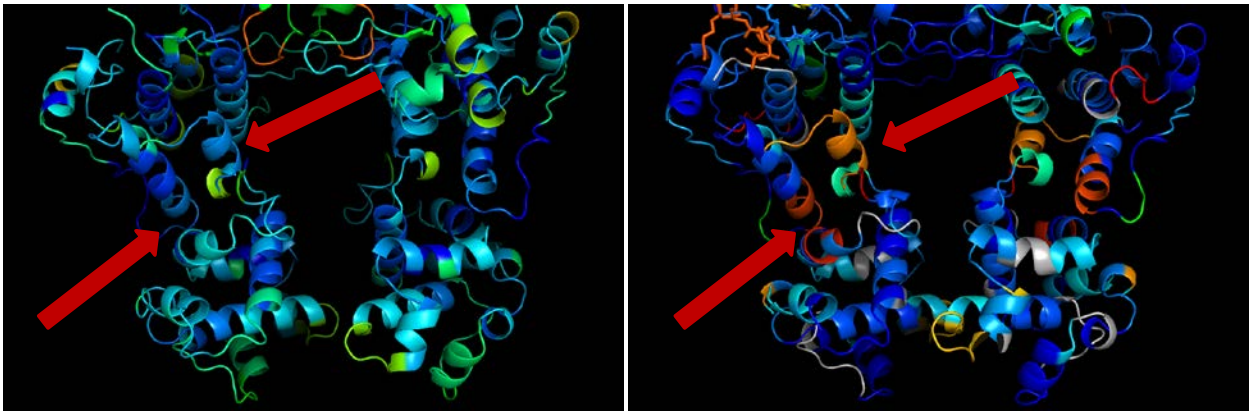

D

pIRE1α+GSK2850163 **pIRE1α+STS**

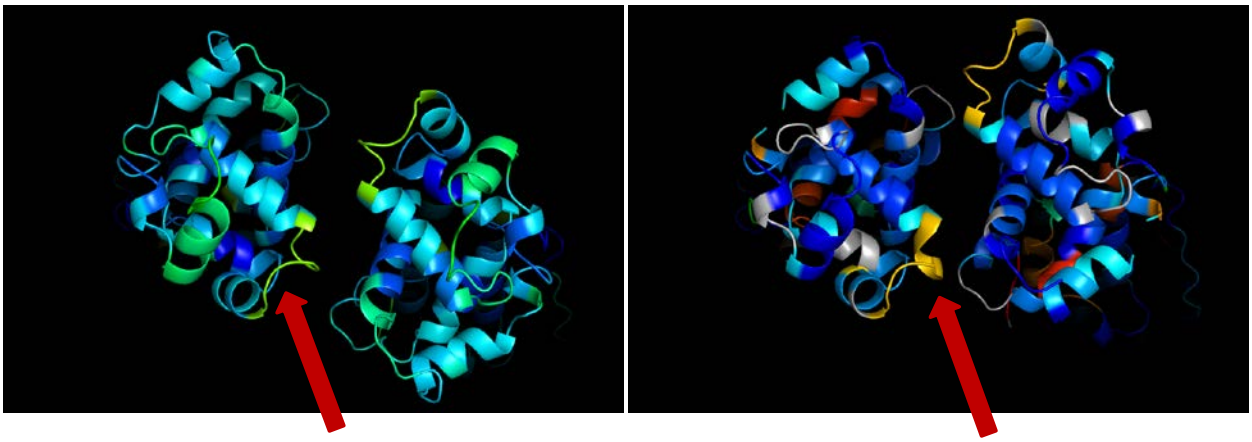

Supplementary Figure 5 (continued). Differential labeling in the Hydrogen/Deuterium Exchange (HDX). (C) Two short α-helices at the interface of the kinase and RNase domains exchange more readily in the presence of STS (right) compared to GSK2850163 (left) where there is less interactions between RNase domains due to distance. In the presence of STS, the following residues showed increased labeling: 800-806 (kinase H α-helix), residues 822-829 (kinase I α-helix), residues 945-950 (in the RNase C-terminal α-helix), and residues 960-964 (at the C-terminus). The loosening of the interactions across the intramolecular domain interface occurs in concert with the conditions under which dimerization of pIRE1α favors the intermolecular interaction between the RNase domains by STS. (D) Overall labeling of the RNase domains in the pIRE1α-GSK2850163 dimer (left) compared to the pIRE1α-STS dimer (right). STS promotes dimerization of the pIRE1α RNase domain, and as a result there is less surface available for exchange. Note the increased labeling of residues 900-916 in the presence of STS which are critical for catalysis. We found no significant differences in the average B-factors of these residues in both structures to suggest higher mobility.

Supplementary Table 1. In vitro selectivity of GSK2850163 across a panel of 284 kinases

Kinase	% Activity remaining after 10 µM GSK2850163
Abl(h)	131
Abl(m)	111
Abl (H396P) (h)	98
Abl (M351T)(h)	115
Abl (Q252H) (h)	116
Abl(T315I)(h)	107
Abl(Y253F)(h)	110
ACK1(h)	106
ALK(h)	104
ALK4(h)	81
Arg(h)	125
AMPKα1(h)	96
AMPKα2(h)	-1
Arg(m)	108
ARK5(h)	99
ASK1(h)	92
Aurora-A(h)	128
Aurora-B(h)	108
Aurora-C(h)	72
Axl(h)	99
Blk(h)	70
Blk(m)	93
Bmx(h)	87
BRK(h)	94
BrSK1(h)	99
BrSK2(h)	100
BTK(h)	109
BTK(R28H)(h)	116
CaMKI(h)	94
CaMKIIβ(h)	71
CaMKIIγ(h)	97
CaMKIδ(h)	109
CaMKIIδ(h)	91
CaMKIV(h)	117
CDK1/cyclinB(h)	110
CDK2/cyclinA(h)	99
CDK2/cyclinE(h)	93
CDK3/cyclinE(h)	106
CDK5/p25(h)	117
CDK5/p35(h)	113
CDK6/cyclinD3(h)	110
CDK7/cyclinH/MAT1(h)	118
CDK9/cyclin T1(h)	99
CHK1(h)	107

Kinase	% Activity remaining after 10 µM GSK2850163
CHK2(h)	101
CHK2(I157T)(h)	97
CHK2(R145W)(h)	93
CK1γ1(h)	110
CK1γ2(h)	111
CK1γ3(h)	110
CK1δ(h)	97
CK1(y)	90
CK2(h)	101
CK2α2(h)	106
CLK2(h)	108
CLK3(h)	96
cKit(h)	97
cKit(D816V)(h)	95
cKit(D816H)(h)	98
cKit(V560G)(h)	97
cKit(V654A)(h)	99
CSK(h)	110
c-RAF(h)	92
cSRC(h)	107
DAPK1(h)	102
DAPK2(h)	88
DCAMKL2(h)	135
DDR2(h)	106
DMPK(h)	109
DRAK1(h)	117
DYRK2(h)	109
eEF-2K(h)	118
EGFR(h)	105
EGFR(L858R)(h)	92
EGFR(L861Q)(h)	98
EGFR(T790M)(h)	100
EGFR(T790M,L858R)(h)	89
EphA1(h)	106
EphA2(h)	89
EphA3(h)	98
EphA4(h)	103
EphA5(h)	118
EphA7(h)	105
EphA8(h)	100
EphB2(h)	112
EphB1(h)	97
EphB3(h)	114
EphB4(h)	106

Kinase	% Activity remaining after 10 µM GSK2850163
ErbB4(h)	88
FAK(h)	98
Fer(h)	100
Fes(h)	107
FGFR1(h)	92
FGFR1(V561M)(h)	62
FGFR2(h)	92
FGFR2(N549H)(h)	94
FGFR3(h)	100
FGFR4(h)	85
Fgr(h)	82
Flt1(h)	105
Flt3(D835Y)(h)	99
Flt3(h)	92
Flt4(h)	97
Fms(h)	106
Fms(Y969C)(h)	103
Fyn(h)	90
GCK(h)	90
GRK5(h)	94
GRK6(h)	98
GRK7(h)	99
GSK3α(h)	115
GSK3β(h)	108
Haspin(h)	66
Hck(h)	101
Hck(h) activated	93
HIPK1(h)	84
HIPK2(h)	111
HIPK3(h)	106
IGF-1R(h)	78
IGF-1R(h), activated	96
IKKα(h)	101
IKKβ(h)	110
IR(h)	104
IR(h), activated	84
IRR(h)	81
IRAK1(h)	112
IRAK4(h)	101
Itk(h)	97
JAK2(h)	151
JAK3(h)	108
JNK1α1(h)	97
JNK2α2(h)	105

Kinase	% Activity remaining after 10 µM GSK2850163
JNK3(h)	72
KDR(h)	111
Lck(h)	62
Lck(h) activated	98
LIMK1(h)	97
LKB1(h)	103
LOK(h)	110
Lyn(h)	94
Lyn(m)	94
MAPK1(h)	84
MAPK2(h)	104
MAPK2(m)	107
MAPKAP-K2(h)	107
MAPKAP-K3(h)	-6
MEK1(h)	103
MARK1(h)	110
MELK(h)	124
Mer(h)	89
Met(h)	100
Met(D1246H)(h)	94
Met(D1246N)(h)	95
Met(M1268T)(h)	99
Met(Y1248C)(h)	86
Met(Y1248D)(h)	93
Met(Y1248H)(h)	76
MINK(h)	109
MKK4(m)	140
MKK6(h)	126
MKK7β(h)	105
MLCK(h)	84
MLK1(h)	94
Mnk2(h)	104
MRCKα(h)	114
MRCKβ(h)	93
MSK1(h)	110
MSK2(h)	112
MSSK1(h)	106
MST1(h)	99
MST2(h)	108
MST3(h)	89
mTOR(h)	81
mTOR/FKBP12(h)	101
MuSK(h)	98
NEK2(h)	97

Kinase	% Activity remaining after 10 µM GSK2850163
NEK3(h)	106
NEK6(h)	130
NEK7(h)	111
NEK11(h)	93
NLK(h)	119
p70S6K(h)	115
PAK2(h)	105
PAK4(h)	102
PAK5(h)	118
PAK6(h)	113
PAR-1Bα(h)	106
PASK(h)	84
PEK(h)	103
PDGFRα(h)	97
PDGFRα(D842V)(h)	103
PDGFRα(V561D)(h)	98
PDGFRβ(h)	108
PDK1(h)	108
PhKγ2(h)	111
Pim-1(h)	109
Pim-2(h)	124
Pim-3(h)	107
PKA(h)	132
PKBα(h)	116
PKBβ(h)	104
PKBγ(h)	96
PKCα(h)	106
PKCβI(h)	95
PKCβII(h)	111
PKCγ(h)	97
PKCδ(h)	100
PKCε(h)	109
PKCη(h)	99
PKCι(h)	99
PKCμ(h)	100
PKCθ(h)	101
PKCζ(h)	103
PKD2(h)	100
PKG1α(h)	112
PKG1β(h)	107
Plk1(h)	98
Plk3(h)	96
PRAK(h)	55
PRK2(h)	114

Kinase	% Activity remaining after 10 µM GSK2850163
PrKX(h)	111
PTK5(h)	104
Pyk2(h)	98
Ret(h)	90
Ret (V804L)(h)	94
Ret(V804M)(h)	109
RIPK2(h)	104
ROCK-I(h)	106
ROCK-II(h)	107
ROCK-II(r)	117
Ron(h)	19
Ros(h)	88
Rse(h)	102
Rsk1(h)	98
Rsk1(r)	110
Rsk2(h)	130
Rsk3(h)	90
Rsk4(h)	103
SAPK2a(h)	94
SAPK2a(T106M)(h)	89
SAPK2b(h)	112
SAPK3(h)	104
SAPK4(h)	110
SGK(h)	121
SGK2(h)	88
SGK3(h)	85
SIK(h)	138
Snk(h)	105
Src(1-530)(h)	109
Src(T341M)(h)	92
SRPK1(h)	105
SRPK2(h)	100
STK33(h)	94
Syk(h)	81
TAK1(h)	110
TAO1(h)	88
TAO2(h)	108
TAO3(h)	99
TBK1(h)	101
Tec(h) activated	74
TGFBR1(h)	100
Tie2 (h)	105
Tie2(R849W)(h)	101
Tie2(Y897S)(h)	107

Kinase	% Activity remaining after 10 μM GSK2850163
TLK2(h)	100
TrkA(h)	86
TrkB(h)	54
TSSK1(h)	88
TSSK2(h)	104
Txk(h)	82
ULK2(h)	108
ULK3(h)	108
WNK2(h)	95
WNK3(h)	92
VRK2(h)	98
Yes(h)	95
ZAP-70(h)	90
ZIPK(h)	109

Note: A panel of 284 kinases (Millipore) was assayed to determine the specificity of GSK2850163. % Activity equals the amount of kinase activity remaining after 10 μM compound treatment. After performing the single shot experiment, a full curve analysis of all potential hits (AMPKα2, FGFR1 V561M, haspin, Lck, MAPKAP-K3, PRAK, Ron, and TrkB) was performed to independently reproduce the initial findings. Only two kinases demonstrated (weak) dose-dependent inhibition by GSK2850163: Ron (IC_{50} = 4.4 μM), and FGFR1 V561M (IC_{50} = 17 μM). All other kinases were unaffected by GSK2850163 treatment.

Preliminary Full wwPDB X-ray Structure Validation Report (i)

Sep 8, 2015 – 05:11 PM EDT

DISCLAIMER

This is a preliminary version of the new style of wwPDB validation report.
This report is produced by the wwPDB validation pipeline
before deposition or annotation of the structure.
This is not an official wwPDB validation report and is not a proof of deposition.
This report should not be submitted to journals.
We welcome your comments at validation@mail.wwpdb.org
A user guide is available at http://wwpdb.org/ValidationPDFNotes.html

The following versions of software and data (see references) were used in the production of this report:

MolProbity	:	4.02b-467
Mogul	:	1.17 November 2013
Xtriage (Phenix)	:	dev-1439
EDS	:	stable24195
Percentile statistics	:	21963
Refmac	:	5.8.0049
CCP4	:	6.3.0 (Settle)
Ideal geometry (proteins)	:	Engh & Huber (2001)
Ideal geometry (DNA, RNA)	:	Parkinson et. al. (1996)
Validation Pipeline (wwPDB-VP)	:	stable24195

1 Overall quality at a glance

The reported resolution of this entry is 2.46 Å.

Percentile scores (ranging between 0-100) for global validation metrics of the entry are shown in the following graphic. The table shows the number of entries on which the scores are based.

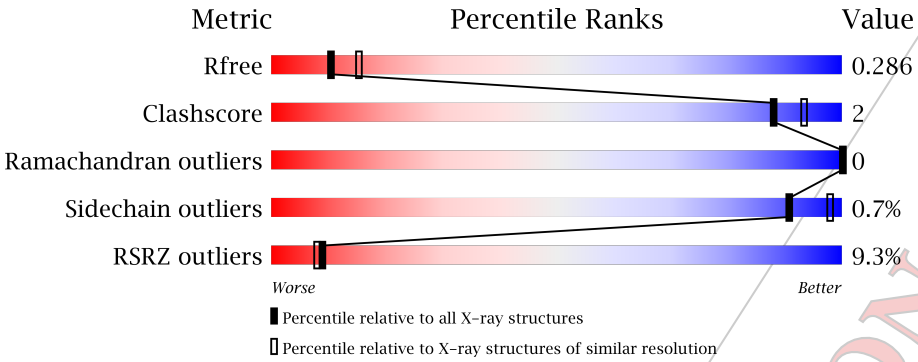

Metric	Whole archive (#Entries)	Similar resolution (#Entries, resolution range(Å))
R_{free}	66092	3566 (2.50-2.42)
Clashscore	79885	4471 (2.50-2.42)
Ramachandran outliers	78287	4383 (2.50-2.42)
Sidechain outliers	78261	4385 (2.50-2.42)
RSRZ outliers	66119	3568 (2.50-2.42)

The table below summarises the geometric issues observed across the polymeric chains and their fit to the electron density. The red, orange, yellow and green segments on the lower bar indicate the fraction of residues that contain outliers for >=3, 2, 1 and 0 types of geometric quality criteria. The upper red bar (where present) indicates the fraction of residues that have poor fit to the electron density.

Mol	Chain	Length	Quality of chain
1	A	381	
2	B	375	
3	C	378	
4	D	3	

2 Entry composition

There are 5 unique types of molecules in this entry. The entry contains 17863 atoms, of which 8734 are hydrogens and 0 are deuterium.

In the tables below, the ZeroOcc column contains the number of atoms modelled with zero occupancy, the AltConf column contains the number of residues with at least one atom in alternate conformation and the Trace column contains the number of residues modelled with at most 2 atoms.

- Molecule 1 is a protein.

Mol	Chain	Residues	Atoms						ZeroOcc	AltConf	Trace
			Total	C	H	N	O	S			
1	A	381	5922	1926	2910	516	551	19	0	1	0

- Molecule 2 is a protein.

Mol	Chain	Residues	Atoms						ZeroOcc	AltConf	Trace
			Total	C	H	N	O	S			
2	B	375	5750	1880	2817	505	529	19	0	1	0

- Molecule 3 is a protein.

Mol	Chain	Residues	Atoms						ZeroOcc	AltConf	Trace
			Total	C	H	N	O	S			
3	C	378	5934	1926	2920	525	544	19	0	3	0

- Molecule 4 is a protein called 163-163-163.

Mol	Chain	Residues	Atoms						ZeroOcc	AltConf	Trace
			Total	C	Cl	H	N	O			
4	D	3	177	72	6	87	9	3	0	0	0

- Molecule 5 is water.

Mol	Chain	Residues	Atoms		ZeroOcc	AltConf
			Total	O		
5	W	80	80	80	0	0

3 Residue-property plots

These plots are drawn for all protein, RNA and DNA chains in the entry. The first graphic for a chain summarises the proportions of errors displayed in the second graphic. The second graphic shows the sequence view annotated by issues in geometry and electron density. Residues are color-coded according to the number of geometric quality criteria for which they contain at least one outlier: green = 0, yellow = 1, orange = 2 and red = 3 or more. A red dot above a residue indicates a poor fit to the electron density (RSRZ > 2). Stretches of 2 or more consecutive residues without any outlier are shown as a green connector. Residues present in the sample, but not in the model, are shown in grey.

- Molecule 1:

Chain A:

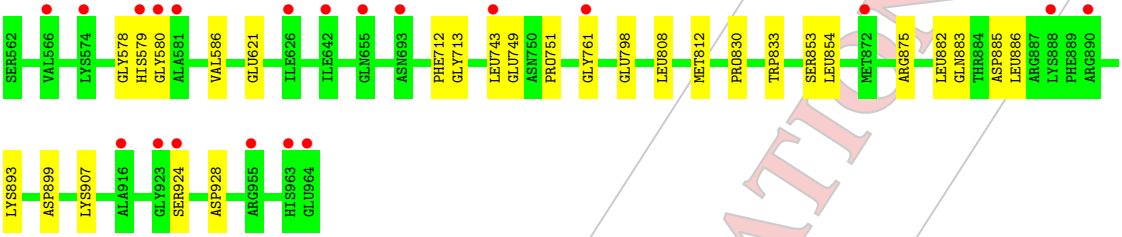

- Molecule 2:

Chain B:

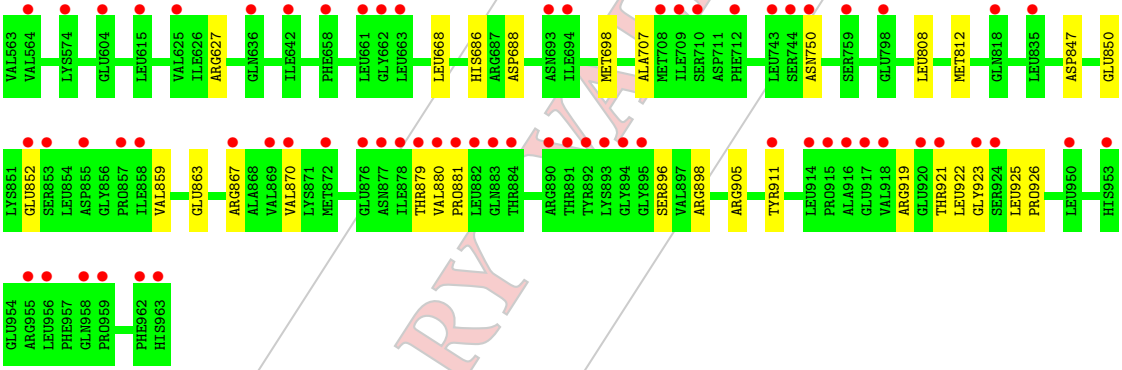

- Molecule 3:

Chain C:

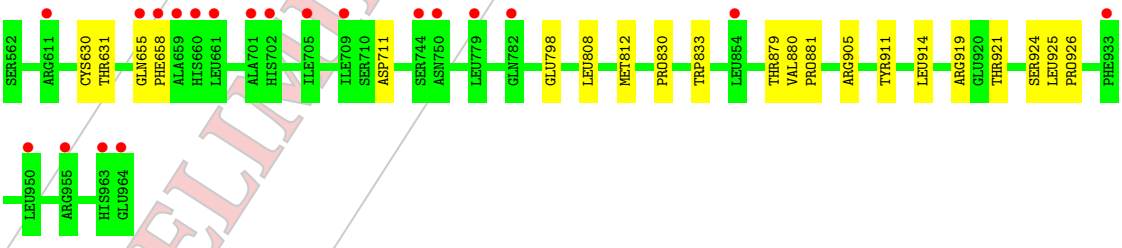

- Molecule 4: 163-163-163

Chain D:

There are no outlier residues recorded for this chain.

4 Data and refinement statistics (i)

Property	Value	Source
Space group	P 21 21 2	Depositor
Cell constants a, b, c, α, β, γ	244.00Å 77.77Å 88.31Å 90.00° 90.00° 90.00°	Depositor
Resolution (Å)	29.18 – 2.46 30.18 – 2.46	Depositor EDS
% Data completeness (in resolution range)	96.7 (29.18-2.46) 96.7 (30.18-2.46)	Depositor EDS
R_{merge}	(Not available)	Depositor
R_{sym}	(Not available)	Depositor
$< I/\sigma(I) >$	-	Xtriage
Refinement program	PHENIX (phenix.refine: 1.9_1692)	Depositor
R, R_{free}	0.235 , 0.283 0.251 , 0.286	Depositor DCC
R_{free} test set	3018 reflections (5.33%)	DCC
Wilson B-factor (Å^2)	(Not available)	Xtriage
Anisotropy	(Not available)	Xtriage
Bulk solvent k_{sol}(e/Å^3), B_{sol}(Å^2)	0.36 , 38.9	EDS
Estimated twinning fraction	No twinning to report.	Xtriage
L-test for twinning	$< \|L\| >$ = (Not available), $< L^2 >$ = (Not available)	Xtriage
Outliers	(Not available)	Xtriage
F_o,F_c correlation	0.92	EDS
Total number of atoms	17863	wwPDB-VP
Average B, all atoms (Å^2)	64.0	wwPDB-VP

Xtriage's analysis on translational NCS is as follows: *(Not available)*

5 Model quality

5.1 Standard geometry

Bond lengths and bond angles in the following residue types are not validated in this section: 163

The Z score for a bond length (or angle) is the number of standard deviations the observed value is removed from the expected value. A bond length (or angle) with $|Z| > 5$ is considered an outlier worth inspection. RMSZ is the root-mean-square of all Z scores of the bond lengths (or angles).

Mol	Chain	Bond lengths		Bond angles	
		RMSZ	#$\|Z\|$ >5	RMSZ	#$\|Z\|$ >5
1	A	0.27	0/3088	0.46	0/4186
2	B	0.26	0/3007	0.44	0/4078
3	C	0.28	0/3096	0.46	0/4191
All	All	0.27	0/9191	0.45	0/12455

Chiral center outliers are detected by calculating the chiral volume of a chiral center and verifying if the center is modelled as a planar moiety or with the opposite hand. A planarity outlier is detected by checking planarity of atoms in a peptide group, atoms in a mainchain group or atoms of a sidechain that are expected to be planar.

Mol	Chain	#Chirality outliers	#Planarity outliers
1	A	0	1
2	B	0	1
All	All	0	2

There are no bond length outliers.

There are no bond angle outliers.

There are no chirality outliers.

All (2) planarity outliers are listed below:

Mol	Chain	Res	Type	Group
1	A	580	GLY	Peptide
2	B	922	LEU	Peptide

5.2 Close contacts

In the following table, the Non-H and H(model) columns list the number of non-hydrogen atoms and hydrogen atoms in the chain respectively. The H(added) column lists the number of hydrogens added by MolProbity. The Clashes column lists the number of clashes within the asymmetric unit,

and the number in parentheses is this value normalized per 1000 atoms of the molecule in the chain. The Symm-Clashes column gives symmetry related clashes, in the same way as for the Clashes column.

Mol	Chain	Non-H	H(model)	H(added)	Clashes	Symm-Clashes
1	A	3012	2910	2899	14	0
2	B	2933	2817	2814	15	0
3	C	3014	2920	2922	15	0
4	D	90	87	0	0	0
5	W	80	0	0	3	0
All	All	9129	8734	8635	42	0

Clashscore is defined as the number of clashes calculated for the entry per 1000 atoms (including hydrogens) of the entry. The overall clashscore for this entry is 2.

All (42) close contacts within the same asymmetric unit are listed below.

Atom-1	Atom-2	Distance(Å)	Clash(Å)
2:B:850:GLU:O	2:B:898:ARG:NH2	2.12	0.83
3:C:914:LEU:O	3:C:919:ARG:NH1	2.19	0.75
1:A:885:ASP:OD2	1:A:907:LYS:NZ	2.19	0.74
2:B:925:LEU:HD23	2:B:926:PRO:N	2.07	0.69
3:C:655:GLN:C	3:C:658:PHE:HA	2.15	0.67
2:B:847:ASP:OD1	2:B:905:ARG:NE	2.34	0.61
3:C:879:THR:HG21	3:C:921:THR:HB	1.82	0.60
1:A:875:ARG:O	1:A:883:GLN:NE2	2.34	0.59
1:A:621:GLU:OE2	5:W:86:HOH:O	2.17	0.59
2:B:925:LEU:HD23	2:B:926:PRO:CA	2.37	0.55
1:A:798:GLU:HG3	3:C:798:GLU:HG3	1.90	0.53
3:C:630:CYS:SG	3:C:631:THR:N	2.84	0.51
3:C:881:PRO:HB2	3:C:921:THR:HG21	1.93	0.51
2:B:686:HIS:ND1	2:B:688:ASP:O	2.44	0.50
2:B:863:GLU:OE2	2:B:896:SER:OG	2.23	0.49
2:B:919:ARG:O	2:B:923:GLY:N	2.45	0.49
1:A:893:LYS:N	1:A:899:ASP:OD2	2.47	0.47
2:B:627:ARG:NH1	5:W:86:HOH:O	2.47	0.46
3:C:711[B]:ASP:OD1	5:W:30:HOH:O	2.21	0.46
2:B:911:TYR:OH	2:B:923:GLY:O	2.31	0.46
2:B:867:ARG:HA	2:B:870:VAL:HB	1.97	0.45
2:B:880:VAL:HB	2:B:881:PRO:HD3	1.98	0.45
2:B:852:GLU:HB2	2:B:859:VAL:CG2	2.46	0.45
3:C:925:LEU:HD23	3:C:926:PRO:HA	1.98	0.45
2:B:879:THR:HG21	2:B:921:THR:HG21	1.98	0.45
3:C:808:LEU:HG	3:C:812:MET:HE2	1.99	0.44
1:A:808:LEU:HG	1:A:812:MET:HE2	1.99	0.44

Continued on next page...

Continued from previous page...

Atom-1	Atom-2	Distance(Å)	Clash(Å)
1:A:749:GLU:HG2	1:A:751:PRO:HD3	1.98	0.44
1:A:578:GLY:HA3	1:A:713:GLY:O	2.17	0.44
3:C:911:TYR:CG	3:C:925:LEU:HD12	2.53	0.43
3:C:879:THR:HG21	3:C:921:THR:CB	2.48	0.43
2:B:808:LEU:HG	2:B:812:MET:HE2	2.00	0.43
1:A:853:SER:O	1:A:854:LEU:HB3	2.18	0.43
1:A:928:ASP:OD2	3:C:921:THR:HA	2.19	0.43
1:A:586:VAL:HG21	1:A:712:PHE:CG	2.54	0.42
1:A:882:LEU:O	1:A:886:LEU:HG	2.19	0.42
1:A:830:PRO:HA	1:A:833:TRP:CD2	2.55	0.42
2:B:668:LEU:HG	2:B:707:ALA:HB2	2.02	0.41
3:C:830:PRO:HA	3:C:833:TRP:CD2	2.56	0.41
3:C:880:VAL:HB	3:C:881:PRO:HD3	2.03	0.41
3:C:879:THR:HG23	3:C:881:PRO:HD2	2.03	0.40
1:A:761:GLY:HA2	1:A:812:MET:HE3	2.01	0.40

There are no symmetry-related clashes.

5.3 Torsion angles

5.3.1 Protein backbone (i)

In the following table, the Percentiles column shows the percent Ramachandran outliers of the chain as a percentile score with respect to all X-ray entries followed by that with respect to entries of similar resolution.

The Analysed column shows the number of residues for which the backbone conformation was analysed, and the total number of residues.

Mol	Chain	Analysed	Favoured	Allowed	Outliers	Percentiles	
1	A	376/381 (99%)	366 (97%)	10 (3%)	0	100	100
2	B	368/375 (98%)	354 (96%)	14 (4%)	0	100	100
3	C	373/378 (99%)	359 (96%)	14 (4%)	0	100	100
All	All	1117/1134 (98%)	1079 (97%)	38 (3%)	0	100	100

There are no Ramachandran outliers to report.

5.3.2 Protein sidechains (i)

In the following table, the Percentiles column shows the percent sidechain outliers of the chain as a percentile score with respect to all X-ray entries followed by that with respect to entries of similar resolution. The Analysed column shows the number of residues for which the sidechain conformation was analysed, and the total number of residues.

Mol	Chain	Analysed	Rotameric	Outliers	Percentiles
1	A	319/338 (94%)	316 (99%)	3 (1%)	87 96
2	B	307/333 (92%)	305 (99%)	2 (1%)	91 98
3	C	321/336 (96%)	319 (99%)	2 (1%)	92 98
All	All	947/1007 (94%)	940 (99%)	7 (1%)	91 98

All (7) residues with a non-rotameric sidechain are listed below:

Mol	Chain	Res	Type
1	A	579	HIS
1	A	743	LEU
1	A	924	SER
2	B	698	MET
2	B	750	ASN
3	C	905	ARG
3	C	924	SER

Some sidechains can be flipped to improve hydrogen bonding and reduce clashes. All (1) such sidechains are listed below:

Mol	Chain	Res	Type
3	C	825	HIS

5.3.3 RNA (i)

There are no RNA chains in this entry.

5.4 Non-standard residues in protein, DNA, RNA chains (i)

3 non-standard protein/DNA/RNA residues are modelled in this entry.

In the following table, the Counts columns list the number of bonds (or angles) for which Mogul statistics could be retrieved, the number of bonds (or angles) that are observed in the model and the number of bonds (or angles) that are defined in the chemical component dictionary. The Link column lists molecule types, if any, to which the group is linked. The Z score for a bond length (or angle) is the number of standard deviations the observed value is removed from the expected

value. A bond length (or angle) with $|Z| > 2$ is considered an outlier worth inspection. RMSZ is the root-mean-square of all Z scores of the bond lengths (or angles).

Mol	Type	Chain	Res	Link	Bond lengths			Bond angles		
					Counts	RMSZ	$\#\|Z\| > 2$	Counts	RMSZ	$\#\|Z\| > 2$
4	163	D	1	-	33,?,?	0.72	0	47,?,?	1.81	8 (17%)
4	163	D	2	-	33,?,?	0.73	0	47,?,?	2.08	10 (21%)
4	163	D	3	-	33,?,?	0.71	0	47,?,?	1.56	7 (14%)

In the following table, the Chirals column lists the number of chiral outliers, the number of chiral centers analysed, the number of these observed in the model and the number defined in the chemical component dictionary. Similar counts are reported in the Torsion and Rings columns. '-' means no outliers of that kind were identified.

Mol	Type	Chain	Res	Link	Chirals	Torsions	Rings
4	163	D	1	-	-	0/13/?/?	0/4/?/?
4	163	D	2	-	-	0/13/?/?	0/4/?/?
4	163	D	3	-	-	0/13/?/?	0/4/?/?

There are no bond length outliers.

All (25) bond angle outliers are listed below:

Mol	Chain	Res	Type	Atoms	Z	Observed(^{o})	Ideal(^{o})
4	D	2	163	N14-C16-N18	10.03	122.93	117.74
4	D	1	163	N14-C16-N18	8.57	122.17	117.74
4	D	3	163	N14-C16-N18	6.19	120.94	117.74
4	D	2	163	C25-C28-C53	3.98	114.12	109.06
4	D	3	163	C29-C28-C50	3.81	107.22	101.58
4	D	1	163	C29-C28-C50	3.45	106.68	101.58
4	D	3	163	C25-C28-C53	3.08	112.98	109.06
4	D	2	163	C32-N35-C50	3.05	107.19	104.02
4	D	3	163	C32-N35-C50	2.87	106.99	104.02
4	D	2	163	C29-C28-C50	2.86	105.81	101.58
4	D	2	163	O17-C16-N18	-2.79	117.50	121.77
4	D	1	163	C28-C53-N18	2.74	115.67	111.77
4	D	2	163	C36-N35-C32	-2.74	108.92	113.10
4	D	1	163	C36-N35-C32	-2.73	108.93	113.10
4	D	1	163	C29-C28-C53	-2.67	107.06	111.05
4	D	1	163	C25-C28-C53	2.63	112.41	109.06
4	D	3	163	C36-N35-C50	-2.57	110.20	112.81
4	D	2	163	C28-C53-N18	2.49	115.31	111.77
4	D	1	163	C32-N35-C50	2.44	106.56	104.02
4	D	3	163	C29-C28-C53	-2.35	107.54	111.05

Continued on next page...

Continued from previous page...

Mol	Chain	Res	Type	Atoms	Z	Observed(^{o})	Ideal(^{o})
4	D	1	163	O17-C16-N18	-2.31	118.24	121.77
4	D	3	163	C36-N35-C32	-2.27	109.63	113.10
4	D	2	163	C22-C19-N18	2.25	115.28	110.65
4	D	2	163	C19-N18-C53	2.20	117.23	113.98
4	D	2	163	C28-C50-N35	-2.16	101.20	103.76

There are no chirality outliers.

There are no torsion outliers.

There are no ring outliers.

5.5 Carbohydrates (i)

There are no carbohydrates in this entry.

5.6 Ligand geometry (i)

There are no ligands in this entry.

5.7 Other polymers (i)

There are no such residues in this entry.

5.8 Polymer linkage issues

There are no chain breaks in this entry.

6 Fit of model and data

6.1 Protein, DNA and RNA chains

In the following table, the column labelled '#RSRZ> 2' contains the number (and percentage) of RSRZ outliers, followed by percent RSRZ outliers for the chain as percentile scores relative to all X-ray entries and entries of similar resolution. The OWAB column contains the minimum, median, 95^{th} percentile and maximum values of the occupancy-weighted average B-factor per residue. The column labelled 'Q< 0.9' lists the number of (and percentage) of residues with an average occupancy less than 0.9.

Mol	Chain	Analysed	<RSRZ>	#RSRZ>2	OWAB(Å^2)	Q<0.9
1	A	381/381 (100%)	0.34	20 (5%) 26 26	28, 49, 79, 111	0
2	B	375/375 (100%)	0.99	66 (17%) 2 2	38, 70, 105, 132	0
3	C	378/378 (100%)	0.31	20 (5%) 25 25	29, 53, 79, 113	0
4	D	0/3	-	-	-	-
All	All	1134/1137 (99%)	0.54	106 (9%) 9 8	28, 56, 95, 132	0

All (106) RSRZ outliers are listed below:

Mol	Chain	Res	Type	RSRZ
2	B	923	GLY	8.8
3	C	964	GLU	7.6
2	B	872	MET	7.0
2	B	891	THR	6.3
2	B	962	PHE	5.6
2	B	916	ALA	5.1
3	C	963	HIS	5.0
2	B	890	ARG	5.0
2	B	963	HIS	5.0
2	B	880	VAL	4.9
2	B	917	GLU	4.9
2	B	882	LEU	4.6
2	B	857	PRO	4.5
2	B	914	LEU	4.5
2	B	615	LEU	4.5
2	B	853	SER	4.4
2	B	893	LYS	4.3
1	A	963	HIS	4.3
2	B	892	TYR	4.2
2	B	858	ILE	4.1
1	A	743	LEU	4.1
2	B	878	ILE	4.1

Continued on next page...

Continued from previous page...

Mol	Chain	Res	Type	RSRZ
2	B	955	ARG	4.0
2	B	884	THR	4.0
1	A	580	GLY	3.8
2	B	574	LYS	3.8
3	C	779	LEU	3.8
2	B	876	GLU	3.8
3	C	854	LEU	3.7
3	C	702	HIS	3.6
2	B	662	GLY	3.6
2	B	744	SER	3.5
2	B	835	LEU	3.5
2	B	709	ILE	3.4
3	C	658	PHE	3.4
2	B	750	ASN	3.3
1	A	872	MET	3.3
1	A	955	ARG	3.3
3	C	659	ALA	3.3
1	A	574	LYS	3.2
2	B	953	HIS	3.2
2	B	855	ASP	3.2
1	A	924	SER	3.1
3	C	750	ASN	3.1
2	B	604	GLU	3.1
2	B	911	TYR	3.1
2	B	877	ASN	3.1
1	A	964	GLU	3.0
2	B	915	PRO	3.0
2	B	818	GLN	3.0
2	B	743	LEU	3.0
2	B	663	LEU	3.0
2	B	959	PRO	2.9
2	B	879	THR	2.9
2	B	958	GLN	2.9
2	B	895	GLY	2.8
3	C	744	SER	2.8
1	A	923	GLY	2.8
1	A	890	ARG	2.8
1	A	916	ALA	2.8
2	B	881	PRO	2.8
2	B	693	ASN	2.7
2	B	918	VAL	2.7
3	C	955	ARG	2.6

Continued on next page...

Continued from previous page...

Mol	Chain	Res	Type	RSRZ
3	C	782	GLN	2.6
1	A	566	VAL	2.6
2	B	852	GLU	2.6
3	C	655	GLN	2.6
2	B	956	LEU	2.5
2	B	564	VAL	2.5
2	B	710	SER	2.5
2	B	694	ILE	2.5
2	B	950	LEU	2.5
3	C	661	LEU	2.5
2	B	883	GLN	2.4
2	B	920	GLU	2.4
1	A	655	GLN	2.4
2	B	658	PHE	2.4
2	B	867	ARG	2.4
2	B	869	VAL	2.4
3	C	709	ILE	2.4
1	A	579	HIS	2.4
3	C	933	PHE	2.4
3	C	705	ILE	2.4
1	A	761	GLY	2.3
1	A	642	ILE	2.3
2	B	636	GLN	2.3
1	A	581	ALA	2.3
2	B	921	THR	2.3
3	C	701	ALA	2.2
3	C	611	ARG	2.2
2	B	712	PHE	2.2
2	B	759	SER	2.2
2	B	661	LEU	2.2
2	B	642	ILE	2.2
1	A	888	LYS	2.2
2	B	625	VAL	2.2
2	B	924	SER	2.1
2	B	894	GLY	2.1
2	B	870	VAL	2.1
2	B	708	MET	2.1
3	C	660	HIS	2.1
3	C	950	LEU	2.1
1	A	626	ILE	2.1
1	A	693	ASN	2.0
2	B	798	GLU	2.0

6.2 Non-standard residues in protein, DNA, RNA chains (i)

In the following table, the Atoms column lists the number of modelled atoms in the group and the number defined in the chemical component dictionary. LLDF column lists the quality of electron density of the group with respect to its neighbouring residues in protein, DNA or RNA chains. The B-factors column lists the minimum, median, 95^{th} percentile and maximum values of B factors of atoms in the group. The column labelled 'Q< 0.9' lists the number of atoms with occupancy less than 0.9.

Mol	Type	Chain	Res	Atoms	RSR	LLDF	B-factors(Å^2)	Q<0.9
4	163	D	3	30/?	0.19	0.19	43,61,81,180	0
4	163	D	2	30/?	0.22	0.06	57,80,106,117	0
4	163	D	1	30/?	0.17	-0.43	32,48,70,89	0

6.3 Carbohydrates (i)

There are no carbohydrates in this entry.

6.4 Ligands (i)

There are no ligands in this entry.

6.5 Other polymers (i)

There are no such residues in this entry.

Preliminary Full wwPDB X-ray Structure Validation Report (i)

Sep 9, 2015 – 07:47 AM EDT

DISCLAIMER

This is a preliminary version of the new style of wwPDB validation report.
This report is produced by the wwPDB validation pipeline
before deposition or annotation of the structure.
This is not an official wwPDB validation report and is not a proof of deposition.
This report should not be submitted to journals.
We welcome your comments at validation@mail.wwpdb.org
A user guide is available at http://wwpdb.org/ValidationPDFNotes.html

The following versions of software and data (see references) were used in the production of this report:

MolProbity	:	4.02b-467
Mogul	:	1.17 November 2013
Xtriage (Phenix)	:	dev-1439
EDS	:	stable24195
Percentile statistics	:	21963
Refmac	:	5.8.0049
CCP4	:	6.3.0 (Settle)
Ideal geometry (proteins)	:	Engh & Huber (2001)
Ideal geometry (DNA, RNA)	:	Parkinson et. al. (1996)
Validation Pipeline (wwPDB-VP)	:	stable24195

1 Overall quality at a glance

The reported resolution of this entry is 3.10 Å.

Percentile scores (ranging between 0-100) for global validation metrics of the entry are shown in the following graphic. The table shows the number of entries on which the scores are based.

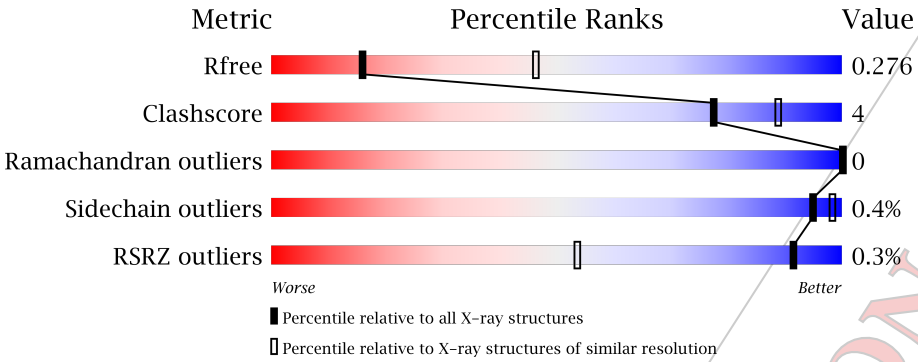

Metric	Whole archive (#Entries)	Similar resolution (#Entries, resolution range(Å))
R_{free}	66092	1007 (3.18-3.02)
Clashscore	79885	1078 (3.16-3.04)
Ramachandran outliers	78287	1044 (3.16-3.04)
Sidechain outliers	78261	1044 (3.16-3.04)
RSRZ outliers	66119	1008 (3.18-3.02)

The table below summarises the geometric issues observed across the polymeric chains and their fit to the electron density. The red, orange, yellow and green segments on the lower bar indicate the fraction of residues that contain outliers for >=3, 2, 1 and 0 types of geometric quality criteria. The upper red bar (where present) indicates the fraction of residues that have poor fit to the electron density.

Mol	Chain	Length	Quality of chain
1	A	383	
2	B	385	
3	C	379	

The following table lists non-polymeric compounds that are outliers for geometric or electron-density-fit criteria:

Mol	Type	Chain	Res	Geometry	Electron density
4	MG	F	1	-	X
4	MG	F	2	-	X

2 Entry composition

There are 6 unique types of molecules in this entry. The entry contains 16836 atoms, of which 8044 are hydrogens and 0 are deuterium.

In the tables below, the ZeroOcc column contains the number of atoms modelled with zero occupancy, the AltConf column contains the number of residues with at least one atom in alternate conformation and the Trace column contains the number of residues modelled with at most 2 atoms.

- Molecule 1 is a protein.

Mol	Chain	Residues	Atoms						ZeroOcc	AltConf	Trace
			Total	C	H	N	O	S			
1	A	383	5756	1900	2795	506	538	17	0	1	0

- Molecule 2 is a protein.

Mol	Chain	Residues	Atoms						ZeroOcc	AltConf	Trace
			Total	C	H	N	O	S			
2	B	385	5567	1859	2661	496	535	16	0	0	0

- Molecule 3 is a protein.

Mol	Chain	Residues	Atoms						ZeroOcc	AltConf	Trace
			Total	C	H	N	O	S			
3	C	379	5369	1808	2554	474	518	15	0	0	0

- Molecule 4 is MAGNESIUM ION (three-letter code: MG) (formula: unknown).

Mol	Chain	Residues	Atoms		ZeroOcc	AltConf
			Total	Mg		
4	F	1	1	1	0	0
4	F	1	Total	Mg	0	0
			1	1		

- Molecule 5 is ADENOSINE-5'-DIPHOSPHATE (three-letter code: ADP) (formula: unknown).

Mol	Chain	Residues	Atoms						ZeroOcc	AltConf
			Total	C	H	N	O	P		
5	E	1	38	10	11	5	10	2	0	0
5	E	1	Total	C	H	N	O	P	0	0
			38	10	11	5	10	2		

Continued on next page...

Continued from previous page...

Mol	Chain	Residues	Atoms						ZeroOcc	AltConf
5	E	1	Total	C	H	N	O	P	0	0
			39	10	12	5	10	2		

- Molecule 6 is water.

Mol	Chain	Residues	Atoms		ZeroOcc	AltConf
6	W	27	Total	O	0	0
			27	27		

3 Residue-property plots

These plots are drawn for all protein, RNA and DNA chains in the entry. The first graphic for a chain summarises the proportions of errors displayed in the second graphic. The second graphic shows the sequence view annotated by issues in geometry and electron density. Residues are color-coded according to the number of geometric quality criteria for which they contain at least one outlier: green = 0, yellow = 1, orange = 2 and red = 3 or more. A red dot above a residue indicates a poor fit to the electron density (RSRZ > 2). Stretches of 2 or more consecutive residues without any outlier are shown as a green connector. Residues present in the sample, but not in the model, are shown in grey.

- Molecule 1:

Chain A:

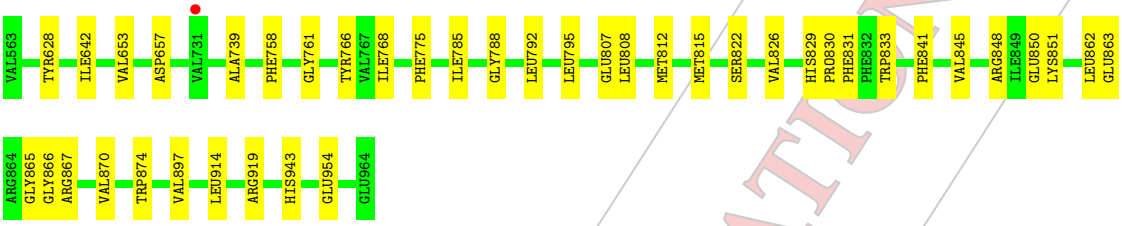

- Molecule 2:

Chain B:

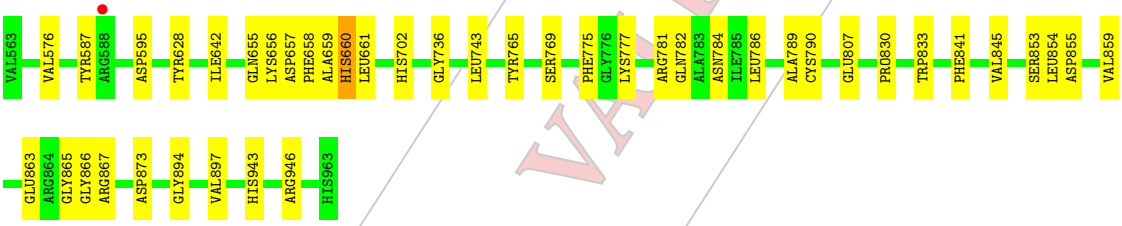

- Molecule 3:

Chain C:

4 Data and refinement statistics (i)

Property	Value	Source
Space group	C 1 2 1	Depositor
Cell constants a, b, c, α, β, γ	191.75Å 122.49Å 77.88Å 90.00° 107.07° 90.00°	Depositor
Resolution (Å)	45.64 – 3.10 45.64 – 3.10	Depositor EDS
% Data completeness (in resolution range)	98.9 (45.64-3.10) 99.0 (45.64-3.10)	Depositor EDS
R_{merge}	(Not available)	Depositor
R_{sym}	(Not available)	Depositor
$< I/\sigma(I) >$ [1]	2.44 (at 3.12Å)	Xtriage
Refinement program	PHENIX (phenix.refine: 1.9_1692)	Depositor
R, R_{free}	0.232 , 0.273 0.233 , 0.276	Depositor DCC
R_{free} test set	1560 reflections (5.05%)	DCC
Wilson B-factor (Å^2)	84.5	Xtriage
Anisotropy	0.425	Xtriage
Bulk solvent k_{sol}(e/Å^3), B_{sol}(Å^2)	0.31 , 41.1	EDS
Estimated twinning fraction	No twinning to report.	Xtriage
L-test for twinning	$< \|L\| > = 0.49, < L^2 > = 0.33$	Xtriage
Outliers	0 of 30913 reflections	Xtriage
F_o,F_c correlation	0.90	EDS
Total number of atoms	16836	wwPDB-VP
Average B, all atoms (Å^2)	97.0	wwPDB-VP

Xtriage's analysis on translational NCS is as follows: *The largest off-origin peak in the Patterson function is 3.62% of the height of the origin peak. No significant pseudotranslation is detected.*

[1] Intensities estimated from amplitudes.

5 Model quality

5.1 Standard geometry

Bond lengths and bond angles in the following residue types are not validated in this section: MG, ADP

The Z score for a bond length (or angle) is the number of standard deviations the observed value is removed from the expected value. A bond length (or angle) with $|Z| > 5$ is considered an outlier worth inspection. RMSZ is the root-mean-square of all Z scores of the bond lengths (or angles).

Mol	Chain	Bond lengths		Bond angles	
		RMSZ	$\#\|Z\| > 5$	RMSZ	$\#\|Z\| > 5$
1	A	0.28	0/3037	0.50	0/4120
2	B	0.27	0/2978	0.48	0/4049
3	C	0.27	0/2882	0.48	0/3925
All	All	0.28	0/8897	0.49	0/12094

There are no bond length outliers.

There are no bond angle outliers.

There are no chirality outliers.

There are no planarity outliers.

5.2 Close contacts

In the following table, the Non-H and H(model) columns list the number of non-hydrogen atoms and hydrogen atoms in the chain respectively. The H(added) column lists the number of hydrogens added by MolProbity. The Clashes column lists the number of clashes within the asymmetric unit, and the number in parentheses is this value normalized per 1000 atoms of the molecule in the chain. The Symm-Clashes column gives symmetry related clashes, in the same way as for the Clashes column.

Mol	Chain	Non-H	H(model)	H(added)	Clashes	Symm-Clashes
1	A	2961	2795	2788	26	0
2	B	2906	2661	2657	24	0
3	C	2815	2554	2553	13	0
4	F	2	0	0	0	0
5	E	81	34	36	0	0
6	W	27	0	0	0	0
All	All	8792	8044	8034	62	0

Clashscore is defined as the number of clashes calculated for the entry per 1000 atoms (including

hydrogens) of the entry. The overall clashscore for this entry is 4.

All (62) close contacts within the same asymmetric unit are listed below.

Atom-1	Atom-2	Distance(Å)	Clash(Å)
2:B:777:LYS:O	2:B:781:ARG:N	2.28	0.67
1:A:914:LEU:O	1:A:919:ARG:NH1	2.27	0.67
1:A:848:ARG:NH2	1:A:954:GLU:OE1	2.36	0.59
1:A:866:GLY:HA2	1:A:867:ARG:CB	2.34	0.58
2:B:866:GLY:HA2	2:B:867:ARG:CB	2.36	0.55
1:A:807:GLU:OE1	1:A:829:HIS:NE2	2.33	0.55
1:A:657:ASP:O	2:B:702:HIS:HA	2.07	0.54
3:C:854:LEU:N	3:C:855:ASP:CB	2.73	0.52
2:B:863:GLU:OE2	2:B:897:VAL:N	2.43	0.51
2:B:854:LEU:N	2:B:855:ASP:CB	2.74	0.50
3:C:808:LEU:HG	3:C:812:MET:HE2	1.93	0.50
1:A:808:LEU:HB2	1:A:829:HIS:CE1	2.47	0.49
2:B:873:ASP:HA	2:B:894:GLY:O	2.12	0.49
2:B:628:TYR:CD1	2:B:642:ILE:HG22	2.48	0.49
2:B:765:TYR:O	2:B:769:SER:OG	2.18	0.49
1:A:628:TYR:CD1	1:A:642:ILE:HG22	2.49	0.48
2:B:830:PRO:HA	2:B:833:TRP:CD2	2.49	0.48
3:C:775:PHE:HD1	3:C:784:ASN:HB3	1.78	0.47
2:B:659:ALA:HA	2:B:661:LEU:N	2.29	0.47
1:A:653:VAL:HG21	1:A:766:TYR:CE2	2.50	0.47
1:A:865:GLY:HA3	1:A:943:HIS:CE1	2.50	0.46
2:B:743:LEU:HD22	2:B:786:LEU:HD21	1.96	0.46
1:A:739:ALA:HA	1:A:758:PHE:CD2	2.50	0.46
3:C:777:LYS:CB	3:C:780:GLN:HG2	2.46	0.46
3:C:799:LYS:O	3:C:803:VAL:HG23	2.15	0.45
1:A:850:GLU:N	1:A:851:LYS:CB	2.80	0.45
1:A:788:GLY:HA2	1:A:815:MET:HE1	1.99	0.44
1:A:863:GLU:OE2	1:A:897:VAL:N	2.51	0.44
1:A:830:PRO:HA	1:A:833:TRP:CD2	2.52	0.44
2:B:655:GLN:HG3	2:B:656:LYS:N	2.33	0.44
3:C:650:GLN:OE1	3:C:692:HIS:NE2	2.50	0.44
3:C:866:GLY:HA2	3:C:867:ARG:CB	2.48	0.44
1:A:862:LEU:CD2	1:A:897:VAL:HB	2.47	0.44
2:B:658:PHE:C	2:B:660:HIS:HB2	2.38	0.44
1:A:870:VAL:HG22	1:A:874:TRP:HB3	1.99	0.43
3:C:808:LEU:HB2	3:C:829:HIS:CE1	2.52	0.43
2:B:655:GLN:HG3	2:B:656:LYS:H	1.82	0.43
2:B:865:GLY:HA3	2:B:943:HIS:CE1	2.53	0.43
3:C:784:ASN:HB3	3:C:789:ALA:HB3	1.99	0.43
1:A:775:PHE:CZ	1:A:785:ILE:HG12	2.53	0.43

Continued on next page...

Continued from previous page...

Atom-1	Atom-2	Distance(Å)	Clash(Å)
2:B:841:PHE:O	2:B:845:VAL:HG23	2.19	0.43
1:A:792:LEU:HD23	1:A:795:LEU:HD12	2.01	0.42
3:C:686:HIS:CE1	3:C:688:ASP:O	2.72	0.42
3:C:858:ILE:HG23	3:C:859:VAL:N	2.34	0.42
1:A:850:GLU:HB3	1:A:851:LYS:CB	2.49	0.42
1:A:775:PHE:N	1:A:775:PHE:CD1	2.87	0.42
3:C:850:GLU:HA	3:C:851:LYS:HA	1.84	0.42
2:B:736:GLY:N	2:B:782:GLN:OE1	2.35	0.42
1:A:761:GLY:HA2	1:A:812:MET:HE3	2.02	0.41
2:B:576:VAL:HG22	2:B:587:TYR:CE1	2.55	0.41
2:B:784:ASN:HB3	2:B:789:ALA:HB3	2.01	0.41
2:B:775:PHE:CE2	2:B:790:CYS:HB3	2.56	0.41
2:B:656:LYS:O	2:B:657:ASP:CB	2.69	0.41
2:B:807:GLU:OE2	2:B:946:ARG:NE	2.52	0.41
3:C:792:LEU:HD12	3:C:792:LEU:N	2.36	0.41
1:A:841:PHE:O	1:A:845:VAL:HG23	2.20	0.41
1:A:768:ILE:HD11	1:A:831:PHE:CE1	2.55	0.40
1:A:822:SER:O	1:A:826:VAL:HG23	2.21	0.40
2:B:853:SER:CB	2:B:855:ASP:CB	2.99	0.40
1:A:862:LEU:O	1:A:943:HIS:NE2	2.51	0.40
2:B:854:LEU:CB	2:B:859:VAL:CB	2.99	0.40
1:A:862:LEU:HD21	1:A:897:VAL:CG1	2.52	0.40

There are no symmetry-related clashes.

5.3 Torsion angles

5.3.1 Protein backbone

In the following table, the Percentiles column shows the percent Ramachandran outliers of the chain as a percentile score with respect to all X-ray entries followed by that with respect to entries of similar resolution.

The Analysed column shows the number of residues for which the backbone conformation was analysed, and the total number of residues.

Mol	Chain	Analysed	Favoured	Allowed	Outliers	Percentiles	
1	A	376/383 (98%)	363 (96%)	13 (4%)	0	100	100
2	B	377/385 (98%)	359 (95%)	18 (5%)	0	100	100
3	C	369/379 (97%)	355 (96%)	14 (4%)	0	100	100
All	All	1122/1147 (98%)	1077 (96%)	45 (4%)	0	100	100

There are no Ramachandran outliers to report.

5.3.2 Protein sidechains

In the following table, the Percentiles column shows the percent sidechain outliers of the chain as a percentile score with respect to all X-ray entries followed by that with respect to entries of similar resolution. The Analysed column shows the number of residues for which the sidechain conformation was analysed, and the total number of residues.

Mol	Chain	Analysed	Rotameric	Outliers	Percentiles	
1	A	299/340 (88%)	299 (100%)	0	100	100
2	B	284/342 (83%)	282 (99%)	2 (1%)	91	97
3	C	269/337 (80%)	268 (100%)	1 (0%)	95	98
All	All	852/1019 (84%)	849 (100%)	3 (0%)	95	98

All (3) residues with a non-rotameric sidechain are listed below:

Mol	Chain	Res	Type
2	B	595	ASP
2	B	660	HIS
3	C	743	LEU

Some sidechains can be flipped to improve hydrogen bonding and reduce clashes. All (1) such sidechains are listed below:

Mol	Chain	Res	Type
1	A	702	HIS

5.3.3 RNA

There are no RNA chains in this entry.

5.4 Non-standard residues in protein, DNA, RNA chains

There are no non-standard protein/DNA/RNA residues in this entry.

5.5 Carbohydrates

There are no carbohydrates in this entry.

5.6 Ligand geometry (i)

Of 5 ligands modelled in this entry, 2 are modelled with single atom - leaving 3 for Mogul analysis.

In the following table, the Counts columns list the number of bonds (or angles) for which Mogul statistics could be retrieved, the number of bonds (or angles) that are observed in the model and the number of bonds (or angles) that are defined in the chemical component dictionary. The Link column lists molecule types, if any, to which the group is linked. The Z score for a bond length (or angle) is the number of standard deviations the observed value is removed from the expected value. A bond length (or angle) with $|Z| > 2$ is considered an outlier worth inspection. RMSZ is the root-mean-square of all Z scores of the bond lengths (or angles).

Mol	Type	Chain	Res	Link	Bond lengths			Bond angles		
					Counts	RMSZ	$\#\|Z\|>2$	Counts	RMSZ	$\#\|Z\|>2$
5	ADP	E	1	-	29,?,?	1.31	4 (13%)	45,?,?	2.01	13 (28%)
5	ADP	E	2	-	29,?,?	1.29	4 (13%)	45,?,?	1.91	13 (28%)
5	ADP	E	3	-	29,?,?	1.31	4 (13%)	45,?,?	1.91	12 (26%)

In the following table, the Chirals column lists the number of chiral outliers, the number of chiral centers analysed, the number of these observed in the model and the number defined in the chemical component dictionary. Similar counts are reported in the Torsion and Rings columns. '-' means no outliers of that kind were identified.

Mol	Type	Chain	Res	Link	Chirals	Torsions	Rings
5	ADP	E	1	-	-	0/16/?/?	0/3/?/?
5	ADP	E	2	-	-	0/16/?/?	0/3/?/?
5	ADP	E	3	-	-	0/16/?/?	0/3/?/?

All (12) bond length outliers are listed below:

Mol	Chain	Res	Type	Atoms	Z	Observed(Å)	Ideal(Å)
5	E	3	ADP	C5-C4	4.21	1.47	1.38
5	E	1	ADP	C5-C4	4.10	1.46	1.38
5	E	2	ADP	C5-C4	4.06	1.46	1.38
5	E	2	ADP	C5-N7	-2.78	1.34	1.39
5	E	3	ADP	C5-C6	2.72	1.48	1.41
5	E	1	ADP	C5-C6	2.70	1.47	1.41
5	E	1	ADP	C5-N7	-2.65	1.34	1.39
5	E	3	ADP	C5-N7	-2.52	1.34	1.39
5	E	1	ADP	C8-N7	2.46	1.36	1.31
5	E	3	ADP	C8-N7	2.41	1.36	1.31
5	E	2	ADP	C8-N7	2.32	1.36	1.31
5	E	2	ADP	C5-C6	2.26	1.46	1.41

All (38) bond angle outliers are listed below:

Mol	Chain	Res	Type	Atoms	Z	Observed(^{o})	Ideal(^{o})
5	E	1	ADP	C5-C4-N3	-6.23	118.65	126.84
5	E	3	ADP	C5-C4-N3	-5.57	119.52	126.84
5	E	2	ADP	C5-C4-N3	-5.51	119.60	126.84
5	E	1	ADP	N3-C4-N9	5.02	135.25	127.00
5	E	2	ADP	N3-C4-N9	4.94	135.12	127.00
5	E	1	ADP	C2-N3-C4	4.79	121.37	111.39
5	E	3	ADP	C2-N3-C4	4.59	120.95	111.39
5	E	3	ADP	N3-C4-N9	4.58	134.54	127.00
5	E	2	ADP	C2-N3-C4	4.40	120.55	111.39
5	E	3	ADP	N3-C2-N1	-3.63	122.56	128.67
5	E	2	ADP	N3-C2-N1	-3.54	122.71	128.67
5	E	1	ADP	N3-C2-N1	-3.43	122.89	128.67
5	E	1	ADP	PA-O3A-PB	-3.37	121.36	132.67
5	E	1	ADP	C5-N7-C8	3.20	107.51	103.61
5	E	2	ADP	C4-N9-C8	3.08	109.26	105.72
5	E	3	ADP	C5-N7-C8	3.04	107.32	103.61
5	E	3	ADP	C6-C5-N7	3.02	136.66	131.97
5	E	1	ADP	C4-C5-N7	-2.99	106.91	110.64
5	E	3	ADP	PA-O3A-PB	-2.95	122.76	132.67
5	E	2	ADP	C5-C6-N6	-2.92	118.94	123.64
5	E	3	ADP	C4-C5-N7	-2.90	107.02	110.64
5	E	3	ADP	C4-N9-C8	2.83	108.97	105.72
5	E	1	ADP	C6-C5-N7	2.76	136.26	131.97
5	E	2	ADP	C5-N7-C8	2.70	106.90	103.61
5	E	1	ADP	C4-N9-C8	2.68	108.79	105.72
5	E	1	ADP	C3'-C2'-C1'	2.47	106.38	101.40
5	E	2	ADP	C6-C5-N7	2.26	135.48	131.97
5	E	1	ADP	N9-C8-N7	-2.25	110.69	113.89
5	E	2	ADP	PA-O3A-PB	-2.25	125.13	132.67
5	E	2	ADP	N9-C8-N7	-2.24	110.70	113.89
5	E	2	ADP	C4-C5-N7	-2.23	107.85	110.64
5	E	1	ADP	C5-C6-N6	-2.22	120.06	123.64
5	E	3	ADP	N9-C8-N7	-2.22	110.74	113.89
5	E	3	ADP	O2B-PB-O3B	2.12	115.44	107.38
5	E	2	ADP	N6-C6-N1	2.10	122.60	118.39
5	E	2	ADP	C2'-C1'-N9	-2.07	107.66	113.34
5	E	1	ADP	O3B-PB-O1B	2.05	115.17	107.38
5	E	3	ADP	C2-N1-C6	2.05	122.45	118.77

There are no chirality outliers.

There are no torsion outliers.

There are no ring outliers.

5.7 Other polymers (i)

There are no such residues in this entry.

5.8 Polymer linkage issues

There are no chain breaks in this entry.

6 Fit of model and data

6.1 Protein, DNA and RNA chains

In the following table, the column labelled '#RSRZ> 2' contains the number (and percentage) of RSRZ outliers, followed by percent RSRZ outliers for the chain as percentile scores relative to all X-ray entries and entries of similar resolution. The OWAB column contains the minimum, median, 95^{th} percentile and maximum values of the occupancy-weighted average B-factor per residue. The column labelled 'Q< 0.9' lists the number of (and percentage) of residues with an average occupancy less than 0.9.

Mol	Chain	Analysed	<RSRZ>	#RSRZ>2			OWAB(Å^2)	Q<0.9
1	A	383/383 (100%)	-0.12	1 (0%)	91	53	51, 78, 110, 168	0
2	B	385/385 (100%)	-0.09	1 (0%)	91	53	54, 84, 129, 163	0
3	C	379/379 (100%)	0.03	2 (0%)	88	39	63, 104, 144, 192	0
All	All	1147/1147 (100%)	-0.06	4 (0%)	91	53	51, 88, 135, 192	0

All (4) RSRZ outliers are listed below:

Mol	Chain	Res	Type	RSRZ
3	C	903	ALA	2.9
1	A	731	VAL	2.8
2	B	588	ARG	2.1
3	C	628	TYR	2.1

6.2 Non-standard residues in protein, DNA, RNA chains

There are no non-standard protein/DNA/RNA residues in this entry.

6.3 Carbohydrates

There are no carbohydrates in this entry.

6.4 Ligands

In the following table, the Atoms column lists the number of modelled atoms in the group and the number defined in the chemical component dictionary. LLDF column lists the quality of electron density of the group with respect to its neighbouring residues in protein, DNA or RNA chains. The B-factors column lists the minimum, median, 95^{th} percentile and maximum values of B factors of atoms in the group. The column labelled 'Q< 0.9' lists the number of atoms with occupancy less than 0.9.

Mol	Type	Chain	Res	Atoms	RSR	LLDF	B-factors(Å^2)	Q<0.9
4	MG	F	1	1/?	0.62	13.20	180,180,180,180	0
4	MG	F	2	1/?	0.41	3.45	65,65,65,65	0
5	ADP	E	1	27/?	0.26	1.24	58,81,100,102	0
5	ADP	E	2	27/?	0.24	0.32	53,75,95,102	0
5	ADP	E	3	27/?	0.25	0.00	80,100,122,137	0

6.5 Other polymers (i)

There are no such residues in this entry.

Preliminary Full wwPDB X-ray Structure Validation Report (i)

Sep 9, 2015 – 07:24 AM EDT

DISCLAIMER

This is a preliminary version of the new style of wwPDB validation report.
This report is produced by the wwPDB validation pipeline
before deposition or annotation of the structure.
This is not an official wwPDB validation report and is not a proof of deposition.
This report should not be submitted to journals.
We welcome your comments at validation@mail.wwpdb.org
A user guide is available at http://wwpdb.org/ValidationPDFNotes.html

The following versions of software and data (see references) were used in the production of this report:

MolProbity	:	4.02b-467
Mogul	:	1.17 November 2013
Xtriage (Phenix)	:	dev-1439
EDS	:	stable24195
Percentile statistics	:	21963
Refmac	:	5.8.0049
CCP4	:	6.3.0 (Settle)
Ideal geometry (proteins)	:	Engh & Huber (2001)
Ideal geometry (DNA, RNA)	:	Parkinson et. al. (1996)
Validation Pipeline (wwPDB-VP)	:	stable24195

1 Overall quality at a glance

The reported resolution of this entry is 2.49 Å.

Percentile scores (ranging between 0-100) for global validation metrics of the entry are shown in the following graphic. The table shows the number of entries on which the scores are based.

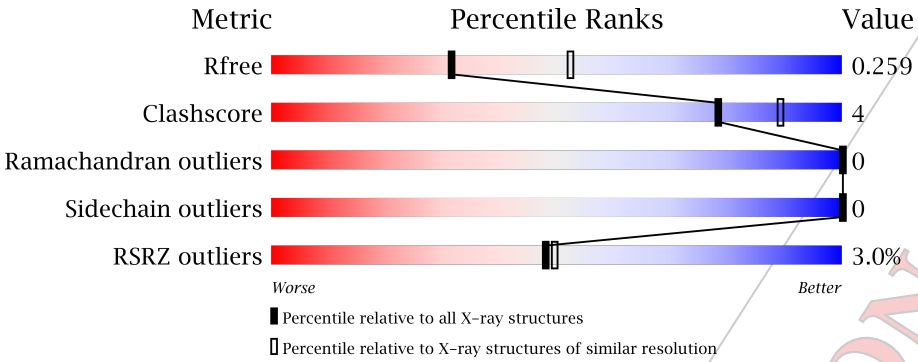

Metric	Whole archive (#Entries)	Similar resolution (#Entries, resolution range(Å))
R_{free}	66092	2784 (2.50-2.50)
Clashscore	79885	3562 (2.50-2.50)
Ramachandran outliers	78287	3480 (2.50-2.50)
Sidechain outliers	78261	3482 (2.50-2.50)
RSRZ outliers	66119	2785 (2.50-2.50)

The table below summarises the geometric issues observed across the polymeric chains and their fit to the electron density. The red, orange, yellow and green segments on the lower bar indicate the fraction of residues that contain outliers for >=3, 2, 1 and 0 types of geometric quality criteria. The upper red bar (where present) indicates the fraction of residues that have poor fit to the electron density.

Mol	Chain	Length	Quality of chain
1	A	385	
2	B	384	

2 Entry composition

There are 4 unique types of molecules in this entry. The entry contains 12013 atoms, of which 5840 are hydrogens and 0 are deuterium.

In the tables below, the ZeroOcc column contains the number of atoms modelled with zero occupancy, the AltConf column contains the number of residues with at least one atom in alternate conformation and the Trace column contains the number of residues modelled with at most 2 atoms.

- Molecule 1 is a protein.

Mol	Chain	Residues	Atoms							ZeroOcc	AltConf	Trace
			Total	C	H	N	O	P	S			
1	A	385	5974	1929	2932	535	556	3	19	0	2	0

- Molecule 2 is a protein.

Mol	Chain	Residues	Atoms							ZeroOcc	AltConf	Trace
			Total	C	H	N	O	P	S			
2	B	384	5857	1901	2854	529	551	3	19	0	0	0

- Molecule 3 is STAUROSPORINE (three-letter code: STU) (formula: unknown).

Mol	Chain	Residues	Atoms					ZeroOcc	AltConf
			Total	C	H	N	O		
3	L	1	62	28	27	4	3	0	0
3	L	1	Total	C	H	N	O	0	0
			62	28	27	4	3		

- Molecule 4 is water.

Mol	Chain	Residues	Atoms		ZeroOcc	AltConf
			Total	O		
4	W	58	58	58	0	0

3 Residue-property plots

These plots are drawn for all protein, RNA and DNA chains in the entry. The first graphic for a chain summarises the proportions of errors displayed in the second graphic. The second graphic shows the sequence view annotated by issues in geometry and electron density. Residues are color-coded according to the number of geometric quality criteria for which they contain at least one outlier: green = 0, yellow = 1, orange = 2 and red = 3 or more. A red dot above a residue indicates a poor fit to the electron density (RSRZ > 2). Stretches of 2 or more consecutive residues without any outlier are shown as a green connector. Residues present in the sample, but not in the model, are shown in grey.

- Molecule 1:

Chain A:

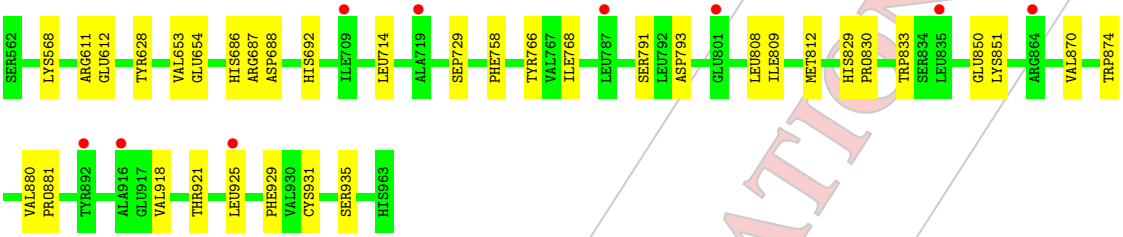

- Molecule 2:

Chain B:

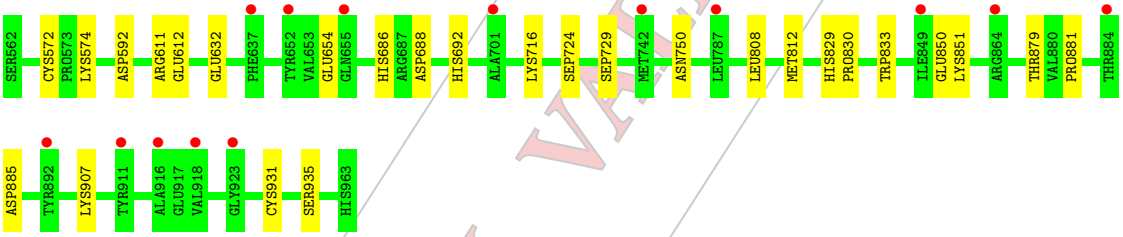

4 Data and refinement statistics (i)

Property	Value	Source
Space group	P 21 21 21	Depositor
Cell constants a, b, c, α, β, γ	49.34Å 155.26Å 155.64Å 90.00° 90.00° 90.00°	Depositor
Resolution (Å)	40.23 – 2.49 40.22 – 2.49	Depositor EDS
% Data completeness (in resolution range)	98.2 (40.23-2.49) 97.7 (40.22-2.49)	Depositor EDS
R_{merge}	(Not available)	Depositor
R_{sym}	(Not available)	Depositor
$< I/\sigma(I) >$	-	Xtriage
Refinement program	PHENIX (phenix.refine: 1.9_1692)	Depositor
R, R_{free}	0.247 , 0.289 0.255 , 0.259	Depositor DCC
R_{free} test set	2116 reflections (5.31%)	DCC
Wilson B-factor (Å^2)	(Not available)	Xtriage
Anisotropy	(Not available)	Xtriage
Bulk solvent k_{sol}(e/Å^3), B_{sol}(Å^2)	0.38 , 27.8	EDS
Estimated twinning fraction	No twinning to report.	Xtriage
L-test for twinning	$< \|L\| >$ = (Not available), $< L^2 >$ = (Not available)	Xtriage
Outliers	(Not available)	Xtriage
F_o,F_c correlation	0.92	EDS
Total number of atoms	12013	wwPDB-VP
Average B, all atoms (Å^2)	52.0	wwPDB-VP

Xtriage's analysis on translational NCS is as follows: *(Not available)*

5 Model quality

5.1 Standard geometry

Bond lengths and bond angles in the following residue types are not validated in this section: STU, SEP

The Z score for a bond length (or angle) is the number of standard deviations the observed value is removed from the expected value. A bond length (or angle) with $|Z| > 5$ is considered an outlier worth inspection. RMSZ is the root-mean-square of all Z scores of the bond lengths (or angles).

Mol	Chain	Bond lengths		Bond angles	
		RMSZ	$\#\|Z\| > 5$	RMSZ	$\#\|Z\| > 5$
1	A	0.25	0/3084	0.45	0/4167
2	B	0.24	0/3040	0.42	0/4111
All	All	0.25	0/6124	0.44	0/8278

There are no bond length outliers.

There are no bond angle outliers.

There are no chirality outliers.

There are no planarity outliers.

5.2 Close contacts

In the following table, the Non-H and H(model) columns list the number of non-hydrogen atoms and hydrogen atoms in the chain respectively. The H(added) column lists the number of hydrogens added by MolProbity. The Clashes column lists the number of clashes within the asymmetric unit, and the number in parentheses is this value normalized per 1000 atoms of the molecule in the chain. The Symm-Clashes column gives symmetry related clashes, in the same way as for the Clashes column.

Mol	Chain	Non-H	H(model)	H(added)	Clashes	Symm-Clashes
1	A	3042	2932	2929	23	0
2	B	3003	2854	2852	19	0
3	L	70	54	52	5	0
4	W	58	0	0	1	0
All	All	6173	5840	5833	43	0

Clashscore is defined as the number of clashes calculated for the entry per 1000 atoms (including hydrogens) of the entry. The overall clashscore for this entry is 4.

All (43) close contacts within the same asymmetric unit are listed below.

Atom-1	Atom-2	Distance(Å)	Clash(Å)
1:A:686:HIS:ND1	1:A:688:ASP:O	2.27	0.68
1:A:654:GLU:N	1:A:654:GLU:OE1	2.29	0.64
1:A:687:ARG:NH2	1:A:729:SEP:O3P	2.31	0.63
3:L:1:STU:H261	3:L:1:STU:H16	1.82	0.60
3:L:2:STU:H16	3:L:2:STU:H261	1.83	0.60
2:B:654:GLU:OE1	2:B:654:GLU:N	2.37	0.57
1:A:758:PHE:HA	1:A:812:MET:O	2.06	0.56
2:B:686:HIS:ND1	2:B:688:ASP:O	2.43	0.51
3:L:2:STU:H273	3:L:2:STU:C17	2.41	0.50
1:A:687:ARG:NH1	1:A:714:LEU:O	2.44	0.49
2:B:572:CYS:SG	2:B:574:LYS:HG2	2.54	0.47
1:A:568:LYS:NZ	2:B:632:GLU:OE2	2.42	0.46
1:A:653:VAL:HG21	1:A:766:TYR:CE2	2.51	0.46
1:A:686:HIS:CE1	1:A:688:ASP:O	2.68	0.46
1:A:918:VAL:HA	1:A:921:THR:HG22	1.98	0.46
1:A:931:CYS:O	1:A:935:SER:OG	2.23	0.46
2:B:885:ASP:OD2	2:B:907:LYS:NZ	2.35	0.45
2:B:724:SEP:O3P	2:B:750:ASN:ND2	2.39	0.45
1:A:692:HIS:HB3	3:L:1:STU:H281	1.99	0.45
2:B:692:HIS:HB3	3:L:2:STU:H281	1.98	0.45
1:A:611:ARG:CG	1:A:612:GLU:N	2.80	0.45
2:B:830:PRO:HA	2:B:833:TRP:CG	2.52	0.45
2:B:808:LEU:HG	2:B:812:MET:HE2	1.99	0.45
2:B:808:LEU:HB2	2:B:829:HIS:CE1	2.52	0.45
2:B:931:CYS:O	2:B:935:SER:OG	2.23	0.44
1:A:808:LEU:HB2	1:A:829:HIS:CE1	2.53	0.44
1:A:870:VAL:HG13	1:A:874:TRP:HB3	1.99	0.44
2:B:724:SEP:O2P	4:W:45:HOH:O	2.21	0.44
1:A:830:PRO:HA	1:A:833:TRP:CG	2.51	0.44
1:A:850:GLU:HA	1:A:851:LYS:HA	1.77	0.44
2:B:850:GLU:HA	2:B:851:LYS:HA	1.84	0.42
2:B:611:ARG:HG3	2:B:612:GLU:N	2.34	0.42
2:B:716:LYS:NZ	2:B:729:SEP:O2P	2.51	0.42
1:A:768:ILE:HD12	1:A:809:ILE:HD11	2.02	0.42
1:A:628:TYR:OH	2:B:592:ASP:OD2	2.24	0.41
1:A:925:LEU:HD23	1:A:929:PHE:CB	2.51	0.41
1:A:830:PRO:HA	1:A:833:TRP:CD2	2.56	0.41
1:A:880:VAL:CG1	1:A:881:PRO:HD3	2.50	0.41
2:B:830:PRO:HA	2:B:833:TRP:CD2	2.56	0.41
2:B:686:HIS:CE1	2:B:688:ASP:O	2.74	0.41
1:A:880:VAL:N	1:A:881:PRO:CD	2.84	0.40
2:B:879:THR:HB	2:B:881:PRO:HD2	2.02	0.40
1:A:791:SER:OG	1:A:793:ASP:OD1	2.38	0.40

There are no symmetry-related clashes.

5.3 Torsion angles

5.3.1 Protein backbone

In the following table, the Percentiles column shows the percent Ramachandran outliers of the chain as a percentile score with respect to all X-ray entries followed by that with respect to entries of similar resolution.

The Analysed column shows the number of residues for which the backbone conformation was analysed, and the total number of residues.

Mol	Chain	Analysed	Favoured	Allowed	Outliers	Percentiles	
1	A	374/385 (97%)	362 (97%)	12 (3%)	0	100	100
2	B	371/384 (97%)	362 (98%)	9 (2%)	0	100	100
All	All	745/769 (97%)	724 (97%)	21 (3%)	0	100	100

There are no Ramachandran outliers to report.

5.3.2 Protein sidechains

In the following table, the Percentiles column shows the percent sidechain outliers of the chain as a percentile score with respect to all X-ray entries followed by that with respect to entries of similar resolution. The Analysed column shows the number of residues for which the sidechain conformation was analysed, and the total number of residues.

Mol	Chain	Analysed	Rotameric	Outliers	Percentiles	
1	A	317/340 (93%)	317 (100%)	0	100	100
2	B	308/339 (91%)	308 (100%)	0	100	100
All	All	625/679 (92%)	625 (100%)	0	100	100

There are no protein residues with a non-rotameric sidechain to report.

Some sidechains can be flipped to improve hydrogen bonding and reduce clashes. There are no such sidechains identified.

5.3.3 RNA

There are no RNA chains in this entry.

5.4 Non-standard residues in protein, DNA, RNA chains

6 non-standard protein/DNA/RNA residues are modelled in this entry.

In the following table, the Counts columns list the number of bonds (or angles) for which Mogul statistics could be retrieved, the number of bonds (or angles) that are observed in the model and the number of bonds (or angles) that are defined in the chemical component dictionary. The Link column lists molecule types, if any, to which the group is linked. The Z score for a bond length (or angle) is the number of standard deviations the observed value is removed from the expected value. A bond length (or angle) with $|Z| > 2$ is considered an outlier worth inspection. RMSZ is the root-mean-square of all Z scores of the bond lengths (or angles).

Mol	Type	Chain	Res	Link	Bond lengths			Bond angles		
					Counts	RMSZ	$\#\|Z\| > 2$	Counts	RMSZ	$\#\|Z\| > 2$
1	SEP	A	724	-	9,?,?	1.79	4 (44%)	12,?,?	1.29	1 (8%)
1	SEP	A	726	-	9,?,?	1.80	4 (44%)	12,?,?	1.28	1 (8%)
1	SEP	A	729	-	9,?,?	1.67	4 (44%)	12,?,?	1.27	0
2	SEP	B	724	-	9,?,?	1.74	4 (44%)	12,?,?	1.06	0
2	SEP	B	726	-	9,?,?	1.77	4 (44%)	12,?,?	1.39	1 (8%)
2	SEP	B	729	-	9,?,?	1.83	4 (44%)	12,?,?	1.44	1 (8%)

In the following table, the Chirals column lists the number of chiral outliers, the number of chiral centers analysed, the number of these observed in the model and the number defined in the chemical component dictionary. Similar counts are reported in the Torsion and Rings columns. '-' means no outliers of that kind were identified.

Mol	Type	Chain	Res	Link	Chirals	Torsions	Rings
1	SEP	A	724	-	-	0/6/?/?	0/0/?/?
1	SEP	A	726	-	-	0/6/?/?	0/0/?/?
1	SEP	A	729	-	-	0/6/?/?	0/0/?/?
2	SEP	B	724	-	-	0/6/?/?	0/0/?/?
2	SEP	B	726	-	-	0/6/?/?	0/0/?/?
2	SEP	B	729	-	-	0/6/?/?	0/0/?/?

All (24) bond length outliers are listed below:

Mol	Chain	Res	Type	Atoms	Z	Observed(Å)	Ideal(Å)
2	B	729	SEP	CA-C	3.47	1.53	1.49
2	B	726	SEP	CA-C	2.98	1.52	1.49
1	A	726	SEP	CA-C	2.95	1.52	1.49
2	B	724	SEP	CA-C	2.93	1.52	1.49
1	A	724	SEP	CA-C	2.86	1.52	1.49
1	A	729	SEP	CA-C	2.81	1.52	1.49
1	A	724	SEP	P-O2P	2.36	1.61	1.54

Continued on next page...

Continued from previous page...

Mol	Chain	Res	Type	Atoms	Z	Observed(Å)	Ideal(Å)
1	A	726	SEP	P-O1P	2.36	1.61	1.54
1	A	726	SEP	P-O3P	2.36	1.61	1.54
2	B	724	SEP	P-O2P	2.35	1.61	1.54
1	A	726	SEP	P-O2P	2.33	1.61	1.54
1	A	724	SEP	P-O1P	2.32	1.61	1.54
2	B	726	SEP	P-O3P	2.31	1.61	1.54
1	A	724	SEP	P-O3P	2.29	1.61	1.54
2	B	724	SEP	P-O1P	2.27	1.61	1.54
2	B	726	SEP	P-O2P	2.27	1.61	1.54
2	B	729	SEP	P-O2P	2.26	1.61	1.54
2	B	729	SEP	P-O1P	2.25	1.61	1.54
1	A	729	SEP	P-O1P	2.24	1.61	1.54
2	B	726	SEP	P-O1P	2.23	1.61	1.54
2	B	729	SEP	P-O3P	2.19	1.61	1.54
1	A	729	SEP	P-O3P	2.15	1.61	1.54
1	A	729	SEP	P-O2P	2.14	1.61	1.54
2	B	724	SEP	P-O3P	2.05	1.60	1.54

All (4) bond angle outliers are listed below:

Mol	Chain	Res	Type	Atoms	Z	Observed(^{o})	Ideal(^{o})
2	B	726	SEP	OG-CB-CA	2.75	111.19	108.31
1	A	724	SEP	OG-CB-CA	2.56	110.99	108.31
2	B	729	SEP	OG-CB-CA	2.37	110.79	108.31
1	A	726	SEP	OG-CB-CA	2.18	110.60	108.31

There are no chirality outliers.

There are no torsion outliers.

There are no ring outliers.

5.5 Carbohydrates (i)

There are no carbohydrates in this entry.

5.6 Ligand geometry (i)

2 ligands are modelled in this entry.

In the following table, the Counts columns list the number of bonds (or angles) for which Mogul statistics could be retrieved, the number of bonds (or angles) that are observed in the model and

the number of bonds (or angles) that are defined in the chemical component dictionary. The Link column lists molecule types, if any, to which the group is linked. The Z score for a bond length (or angle) is the number of standard deviations the observed value is removed from the expected value. A bond length (or angle) with $|Z| > 2$ is considered an outlier worth inspection. RMSZ is the root-mean-square of all Z scores of the bond lengths (or angles).

Mol	Type	Chain	Res	Link	Bond lengths			Bond angles		
					Counts	RMSZ	$\#\|Z\| > 2$	Counts	RMSZ	$\#\|Z\| > 2$
3	STU	L	1	-	42,?,?	3.02	15 (35%)	68,?,?	1.85	12 (17%)
3	STU	L	2	-	42,?,?	3.01	15 (35%)	68,?,?	1.87	11 (16%)

In the following table, the Chirals column lists the number of chiral outliers, the number of chiral centers analysed, the number of these observed in the model and the number defined in the chemical component dictionary. Similar counts are reported in the Torsion and Rings columns. '-' means no outliers of that kind were identified.

Mol	Type	Chain	Res	Link	Chirals	Torsions	Rings
3	STU	L	1	-	-	0/4/?/?	0/0/?/?
3	STU	L	2	-	-	0/4/?/?	0/0/?/?

All (30) bond length outliers are listed below:

Mol	Chain	Res	Type	Atoms	Z	Observed(Å)	Ideal(Å)
3	L	1	STU	C8-N1	9.00	1.43	1.35
3	L	2	STU	C8-N1	8.92	1.43	1.35
3	L	1	STU	O5-C8	8.73	1.40	1.23
3	L	2	STU	O5-C8	8.67	1.40	1.23
3	L	2	STU	C25-N3	-7.05	1.36	1.46
3	L	1	STU	C25-N3	-6.85	1.36	1.46
3	L	1	STU	C19-N3	5.97	1.50	1.38
3	L	2	STU	C19-N3	5.93	1.50	1.38
3	L	1	STU	C9-C10	5.09	1.55	1.50
3	L	2	STU	C9-C10	5.08	1.55	1.50
3	L	2	STU	C22-C23	-4.12	1.48	1.52
3	L	1	STU	C22-C23	-4.12	1.48	1.52
3	L	2	STU	C20-N3	3.89	1.46	1.39
3	L	1	STU	C20-N3	3.87	1.46	1.39
3	L	1	STU	C26-C21	-3.04	1.48	1.51
3	L	2	STU	C26-C21	-2.94	1.48	1.51
3	L	1	STU	O4-C21	-2.85	1.39	1.43
3	L	2	STU	O4-C21	-2.82	1.39	1.43
3	L	2	STU	O4-C25	2.63	1.48	1.43
3	L	1	STU	C9-N1	2.58	1.48	1.45
3	L	1	STU	O4-C25	2.56	1.48	1.43

Continued on next page...

Continued from previous page...

Mol	Chain	Res	Type	Atoms	Z	Observed(Å)	Ideal(Å)
3	L	2	STU	C7-C8	-2.48	1.39	1.49
3	L	2	STU	C9-N1	2.46	1.48	1.45
3	L	1	STU	C7-C8	-2.45	1.39	1.49
3	L	1	STU	C17-N2	2.40	1.44	1.41
3	L	2	STU	C17-N2	2.40	1.44	1.41
3	L	1	STU	C21-N2	-2.31	1.46	1.48
3	L	2	STU	C21-N2	-2.20	1.46	1.48
3	L	1	STU	C24-C25	2.14	1.55	1.51
3	L	2	STU	C24-C25	2.02	1.54	1.51

All (23) bond angle outliers are listed below:

Mol	Chain	Res	Type	Atoms	Z	Observed(^{o})	Ideal(^{o})
3	L	2	STU	C9-N1-C8	-8.49	107.37	114.02
3	L	1	STU	C9-N1-C8	-8.18	107.61	114.02
3	L	1	STU	O5-C8-N1	-6.15	120.39	125.49
3	L	2	STU	O5-C8-N1	-5.92	120.57	125.49
3	L	1	STU	C7-C8-N1	4.24	111.78	106.46
3	L	2	STU	C7-C8-N1	4.23	111.76	106.46
3	L	2	STU	C5-C20-N3	4.16	110.88	108.90
3	L	1	STU	C5-C20-N3	4.05	110.83	108.90
3	L	2	STU	C28-N4-C23	-3.34	110.07	114.67
3	L	1	STU	C28-N4-C23	-3.24	110.22	114.67
3	L	1	STU	C19-N3-C20	-3.22	104.02	108.22
3	L	2	STU	C19-N3-C20	-3.20	104.04	108.22
3	L	1	STU	C21-N2-C17	3.14	132.18	127.64
3	L	2	STU	C21-N2-C17	3.13	132.16	127.64
3	L	2	STU	C24-C25-N3	-2.53	109.93	112.75
3	L	2	STU	C1-C20-N3	-2.35	125.73	129.71
3	L	1	STU	C1-C20-N3	-2.23	125.92	129.71
3	L	2	STU	C21-O4-C25	2.18	125.00	118.31
3	L	1	STU	C21-O4-C25	2.16	124.93	118.31
3	L	1	STU	C24-C25-N3	-2.15	110.36	112.75
3	L	1	STU	O4-C25-C24	-2.12	109.25	112.50
3	L	2	STU	O4-C25-C24	-2.02	109.40	112.50
3	L	1	STU	C9-C10-C7	2.01	111.14	109.79

There are no chirality outliers.

There are no torsion outliers.

There are no ring outliers.

5.7 Other polymers (i)

There are no such residues in this entry.

5.8 Polymer linkage issues

There are no chain breaks in this entry.

6 Fit of model and data

6.1 Protein, DNA and RNA chains

In the following table, the column labelled '#RSRZ> 2' contains the number (and percentage) of RSRZ outliers, followed by percent RSRZ outliers for the chain as percentile scores relative to all X-ray entries and entries of similar resolution. The OWAB column contains the minimum, median, 95^{th} percentile and maximum values of the occupancy-weighted average B-factor per residue. The column labelled 'Q< 0.9' lists the number of (and percentage) of residues with an average occupancy less than 0.9.

Mol	Chain	Analysed	<RSRZ>	#RSRZ>2	OWAB(Å^2)	Q<0.9
1	A	385/385 (100%)	0.54	9 (2%) 57 60	23, 47, 74, 90	0
2	B	384/384 (100%)	0.62	14 (3%) 41 42	23, 46, 72, 98	0
All	All	769/769 (100%)	0.58	23 (2%) 48 50	23, 46, 74, 98	0

All (23) RSRZ outliers are listed below:

Mol	Chain	Res	Type	RSRZ
2	B	701	ALA	3.9
1	A	864	ARG	3.6
1	A	916	ALA	3.5
2	B	637	PHE	3.4
1	A	719	ALA	3.4
1	A	892	TYR	3.2
2	B	911	TYR	3.1
2	B	923	GLY	3.1
2	B	918	VAL	3.1
2	B	849	ILE	2.9
2	B	787	LEU	2.8
2	B	655	GLN	2.8
1	A	801[A]	GLU	2.6
2	B	916	ALA	2.6
2	B	864	ARG	2.6
1	A	787	LEU	2.4
2	B	652	TYR	2.3
2	B	742	MET	2.3
2	B	884	THR	2.2
1	A	835	LEU	2.2
2	B	892	TYR	2.1
1	A	925	LEU	2.1
1	A	709	ILE	2.0

6.2 Non-standard residues in protein, DNA, RNA chains

In the following table, the Atoms column lists the number of modelled atoms in the group and the number defined in the chemical component dictionary. LLDF column lists the quality of electron density of the group with respect to its neighbouring residues in protein, DNA or RNA chains. The B-factors column lists the minimum, median, 95^{th} percentile and maximum values of B factors of atoms in the group. The column labelled 'Q< 0.9' lists the number of atoms with occupancy less than 0.9.

Mol	Type	Chain	Res	Atoms	RSR	LLDF	B-factors(Å^2)	Q<0.9
1	SEP	A	729	10/?	0.21	0.89	39,50,57,61	0
1	SEP	A	724	10/?	0.17	-0.06	57,63,72,75	0
2	SEP	B	724	10/?	0.18	-0.56	59,69,82,84	0
2	SEP	B	726	10/?	0.17	-0.90	49,59,71,74	0
2	SEP	B	729	10/?	0.17	-1.07	37,44,49,50	0
1	SEP	A	726	10/?	0.13	-1.76	53,66,91,93	0

6.3 Carbohydrates

There are no carbohydrates in this entry.

6.4 Ligands

In the following table, the Atoms column lists the number of modelled atoms in the group and the number defined in the chemical component dictionary. LLDF column lists the quality of electron density of the group with respect to its neighbouring residues in protein, DNA or RNA chains. The B-factors column lists the minimum, median, 95^{th} percentile and maximum values of B factors of atoms in the group. The column labelled 'Q< 0.9' lists the number of atoms with occupancy less than 0.9.

Mol	Type	Chain	Res	Atoms	RSR	LLDF	B-factors(Å^2)	Q<0.9
3	STU	L	1	35/?	0.19	0.05	23,33,43,55	0
3	STU	L	2	35/?	0.19	-0.01	23,31,42,53	0

6.5 Other polymers

There are no such residues in this entry.